



# DISSERTATION

## MIXED GROUP V COMPOUND SEMICONDUCTORS FOR INTERSUBBAND DEVICES

ausgeführt zum Zwecke der Erlangung des akademischen Grades eines  
Doktors der technischen Wissenschaften

unter der Leitung von

**Univ. Prof. Dr. Gottfried Strasser**

Institut für Festkörperelektronik

eingereicht an der

TECHNISCHEN UNIVERSITÄT WIEN

FAKULTÄT FÜR ELEKTROTECHNIK UND INFORMATIONSTECHNIK

von

**Dipl.-Ing. Tobias Zederbauer**

Mat.Nr. 0425186

Othelloasse 1/5/10

A-1230 Wien

Wien, im Mai 2017

Betreut durch: Univ.Prof. Dr. Gottfried Strasser

Begutachtet durch: Prof. Zbigniew Wasilewski, PhD  
Univ.Prof. Dr. Armando Rastelli

Tag der mündlichen Prüfung: 22.05.2017



## Kurzfassung

Für viele Anwendungen im mittleren und fernen Infrarotbereich sind Quantenkaskadenlaser von großem Interesse. Nach dem ersten experimentellen Nachweis der Funktionsfähigkeit dieses Konzeptes setzte eine rasche Weiterentwicklung ein, wodurch bald nahezu im gesamten mittleren Infrarotbereich Laser im Dauerstrichbetrieb und bei Raumtemperatur betrieben werden konnten. Im fernen Infrarotbereich sind Quantenkaskadenlaser jedoch bis heute auf Kryotechnik angewiesen. So liegt die höchste bis heute gezeigte Betriebstemperatur eines Quantenkaskadenlasers im Terahertz Bereich bei unter 200 K. In der Literatur finden sich jedoch Hinweise darauf, dass die Verwendung von Quantentopfmaterialien mit niedriger effektiver Elektronenmasse, wie  $\text{Ga}_x\text{In}_{1-x}\text{As}$  oder  $\text{InAs}$ , zu besseren Ergebnissen führen kann. Da für einen Quantenkaskadenlaser zumindest ein zweites Material als Barriere benötigt wird, steigt das Interesse an exotischeren As-Sb Verbindungshalbleitern, welche mit diesen beiden Quantentopfmaterialien kompatibel sind.

Zwar hat sich für Quantenkaskadenlaser mit  $\text{InAs}$  Quantentöpfen, welche im mittleren Infrarotbereich emittieren,  $\text{AlAs}_{1-x}\text{Sb}_x$  als geeignetes Barrierenmaterial erwiesen, jedoch verlangt die exorbitante Barrierenhöhe dieses Materialsystems im THz Bereich die Verwendung extrem dünner Schichten deren Züchtung nur sehr schwer handhabbar ist, weswegen ein solcher Laser bis heute nicht gezeigt werden konnte. Zur Nutzbarmachung der Vorteile von  $\text{InAs}$  auch für den THz Bereich ist also ein dazu gitterangepasstes Material mit geringerer Barrierenhöhe notwendig. Hier bietet sich der quaternäre Verbindungshalbleiter  $\text{Al}_x\text{In}_{1-x}\text{As}_y\text{Sb}_{1-y}$  an, da durch die richtige Wahl seiner Zusammensetzung Barrierenhöhe und Gitterkonstante unabhängig von einander justiert werden können.

Die vereinzelt in der Literatur zu findenden Artikel, welche sich mit der Züchtung dieses Materials beschäftigen, berichten häufig von schlechter Materialqualität wenn versucht wird einen Aluminiumanteil von etwa 10 % bis 15 % zu überschreiten. Um jedoch das volle Potential dieses Materials ausnutzen, seine Eigenschaften also über einen möglichst großen Bereich einstellen zu können, ist es notwendig sein Verhalten während der Züchtung genau zu verstehen. Innerhalb der vorliegenden Arbeit wurde der Einfluss der Parameter Substrattemperatur, sowie Arsen- und Antimondruck, auf Zusammensetzung und Schichtqualität von  $\text{Al}_x\text{In}_{1-x}\text{As}_y\text{Sb}_{1-y}$  mit einem Aluminiumanteil von  $x=0.462$  mittels Röntgenstrukturanalyse und Rasterkraftmikroskopie untersucht. Die Untersuchungen zeigen eine starke Temperaturabhängigkeit der Einbaurate von Sb in  $\text{Al}_{0.462}\text{In}_{0.538}\text{As}_y\text{Sb}_{1-y}$  wodurch eine niedrige Substrattemperatur für das Erreichen der Gitteranpassung unumgänglich ist. Bei einer Substrattemperatur von  $410^\circ\text{C}$  konnten auf  $\text{InAs}$  gitterangepasste  $\text{Al}_{0.462}\text{In}_{0.538}\text{As}_y\text{Sb}_{1-y}$  Schichten mit hoher Kristallqualität gezüchtet werden.



Die oben erwähnten Ergebnisse zeigen, dass die Züchtung von hochqualitativen Dünnschichten von Verbindungshalbleitern in welchen Arsen und Antimon gemischt auftreten durch das komplexe Zusammenspiel der beiden Gruppe-V-Elemente großen Optimierungsaufwandes Bedarf. Das Verständnis dieses Zusammenspiels ist für diese Optimierung von großem Interesse. Als Modellsystem, anhand dessen diese Familie von Verbindungshalbleitern untersucht werden soll bietet sich die ternäre Verbindung  $\text{GaAs}_{1-x}\text{Sb}_x$  an, da die Gegenwart nur eines einzelnen Gruppe-III-Elements Mehrdeutigkeiten in der Interpretation der Ergebnisse verringert. Um die Interaktion von Arsen und Antimon besser zu verstehen wurden Zusammensetzung und Kristallqualität von  $\text{GaAs}_{1-x}\text{Sb}_x$  in Abhängigkeit von Substrattemperatur, Wachstumsrate, sowie Arsen- und Antimondruck untersucht und die gefundenen Ergebnisse mit Berichten in der Literatur verglichen.

Die Ergebnisse zeigen, dass die Wachstumsrate signifikanten Einfluss sowohl auf die Zusammensetzung also auch auf die Kristallqualität hat und zwei, von unterschiedlichen Mechanismen dominierte Bereiche, unterschieden werden müssen. Bei niedrigen Wachstumsraten ist die Antimonkonzentration direkt mit der Wachstumsrate verknüpft, ihre Verringerung führt also zu einem geringeren Antimonanteil. Bei hohen Wachstumsraten ist hingegen das Gegenteil der Fall. Das beschriebene Verhalten lässt sich dadurch erklären, dass bei hohen Wachstumsraten eine Verknappung von Antimon auftritt, wohingegen bei niedrigen Wachstumsraten ein Prozess dominiert bei welchem Antimon durch Arsen ersetzt wird, was die Antimonkonzentration in der Schicht verringert. Darüber hinaus zeigt sich, dass verspannte Schichten bei niedrigen Wachstumsraten früher relaxieren und so geringere Kristallqualität aufweisen. Bei niedrigen Wachstumstemperaturen und hohen Wachstumsraten kann hingegen ausgezeichnete Kristallqualität erreicht werden.

Da die oben erwähnten Ergebnisse darauf hindeuten, dass niedrige Wachstumstemperaturen, bei welchen tendenziell schlechtere optische sowie elektrische Eigenschaften von Dünnschichten zu erwarten sind, notwendig sind um hohe Kristallqualität zu erreichen wurden  $\text{InAs}$  basierte Halbleiterstrukturen mit  $\text{AlAs}_{1-x}\text{Sb}_x$ -Barrieren bei einer Substrattemperatur von  $400^\circ\text{C}$  gezüchtet und auf ihre Funktionstüchtigkeit überprüft. An einem, unter diesen Bedingungen hergestellten Quantenkaskadendetektor konnte eine spezifische Detektivität von  $2.7 \times 10^7 \text{ cm } \sqrt{\text{Hz}} \text{ W}^{-1}$  bei 300 K und einer Mittenwellenlänge von  $4.84 \mu\text{m}$  gezeigt werden. Darüberhinaus war es erstmals möglich einen  $\text{InAs}$  basierten Quantenkaskadenlaser, welcher im THz-Bereich emittiert, zu zeigen. Unter Anwendung eines senkrecht zur Wachstumsrichtung ausgerichteten Magnetfeldes und Kühlung mittels Flüssighelium zeigte der, auf einem 3-Topf-Konzept basierende Laser, Emission bei 3.8 THz. Diese Ergebnisse zeigen, dass antimonidisch-arsenidische Verbindungshalbleiter großes Potential haben um Durchbrüche im Bereich der Intersubbandoptoelektronik zu ermöglichen.

# Abstract

Coherent light sources in the mid and far infrared are of great interest for chemical sensing in the mid infrared fingerprint region, free-space optical communication in the atmospheric transparency windows as well as imaging applications.

After their first experimental demonstration in 1994, quantum cascade lasers have undergone rapid development and are now reliable and highly customizable coherent light sources in the mid-infrared regime. Despite their great success in this region, cryogenic cooling techniques are still required to enable QCL operation at THz frequencies.

The highest pulsed operation temperature of a THz quantum cascade laser so far has been shown using devices based on the GaAs/AlGaAs material system. There are, however, reports that suggest that the use of well materials with a lower effective electron mass can improve their performance.  $\text{Ga}_x\text{In}_{1-x}\text{As}$  lattice matched to InP and InAs are well material candidates which feature an effective mass lower than that of GaAs. With the increasing interest in these low effective mass materials for intersubband devices, mixed As-Sb compounds, like  $\text{GaAs}_{1-x}\text{Sb}_x$  or  $\text{Al}_x\text{In}_{1-x}\text{As}_y\text{Sb}_{1-y}$ , gain more and more attention.

For InAs based mid-infrared devices,  $\text{AlAs}_{1-x}\text{Sb}_x$  was proven to be a well suited barrier material. In the THz regime, however, the extremely high conduction band offset of this material system requires the growth of sub-monolayer thin barriers which are difficult to control in terms of growth. Despite reports about electroluminescence, from these structures, no laser operation has been reported so far. Finding a barrier material which is much better suited for the design and growth of THz quantum cascade lasers may help to exploit the beneficial properties of InAs as a well material for devices operating in this region.  $\text{Al}_x\text{In}_{1-x}\text{As}_y\text{Sb}_{1-y}$ , which can be grown lattice matched to InAs, should exhibit a tunable band-offset and thus allow for the use of thicker, and hence easily controllable barriers, making it a promising candidate as a barrier material. Reports on the growth of this material by MBE are sparse in literature. This work provides a detailed study on the growth of  $\text{Al}_x\text{In}_{1-x}\text{As}_y\text{Sb}_{1-y}$  lattice-matched to InAs by Molecular Beam Epitaxy. In order to find the conditions which lead to high crystal quality deep within the miscibility gap,  $\text{Al}_x\text{In}_{1-x}\text{As}_y\text{Sb}_{1-y}$  with  $x=0.462$  was grown at different growth temperatures as well as  $\text{As}_2$  and  $\text{Sb}_2$  beam equivalent pressures. The crystal quality of the grown layers was examined by high-resolution X-ray diffraction and atomic force microscopy. It was found that the incorporation of Sb into  $\text{Al}_{0.462}\text{In}_{0.538}\text{As}_y\text{Sb}_{1-y}$  is strongly temperature dependent and reduced growth temperatures are necessary in order to achieve significant Sb mole fractions in the grown layers. At  $480^\circ\text{C}$  lattice matching to InAs could not be achieved. At  $410^\circ\text{C}$  lattice matching was possible and high quality films of  $\text{Al}_{0.462}\text{In}_{0.538}\text{As}_y\text{Sb}_{1-y}$  were obtained.

The results on the growth of  $\text{Al}_x\text{In}_{1-x}\text{As}_y\text{Sb}_{1-y}$  illustrate that the growth of mixed As-Sb compounds materials, still provides significant challenges due to the complex interaction between the group V species. Since in  $\text{GaAs}_{1-x}\text{Sb}_x$  only one group III species is present it is an ideal model

system to study this interaction. In order to find a better understanding of the involved processes, the literature on the growth of this material is evaluated and compared to the results obtained within this work. It was found that the growth rate has a strong influence on the composition of the layer, and that two regimes can be identified in which different effects dominate the incorporation of Sb. While a shortage of Sb leads to a lowering of the Sb content at high growth rates, at low growth rates the As-for-Sb exchange reaction prohibits incorporation of Sb. Moreover, this effect deteriorates the quality of strained layers since it leads to early relaxation. These experiments show that low growth temperatures and moderately high growth rates lead to excellent crystal quality.

The experimental data presented in this work show that low  $T_g$  is beneficial for the crystal quality of mixed As-Sb compounds. Since the optical properties and interface quality of MBE grown materials are strongly dependent on the growth conditions, InAs-based devices using AlAsSb barriers were designed and grown at a  $T_g$  of 400 °C to ensure that grown at low  $T_g$  does not prevent the realization of inter-subband devices. Using a semi-classical Monte-Carlo approach a quantum cascade detector structure was designed, and processed into a mesa structure. The QCD showed a peak specific detectivity  $2.7 \times 10^7 \text{ cm } \sqrt{\text{Hz}} \text{ W}^{-1}$  at 300 K and a center detection wavelength of 4.84  $\mu\text{m}$ . Moreover, it was possible for the first time to show laser performance in the THz regime for InAs-based structures. By applying a magnetic field at liquid helium temperature, an InAs/AlAs<sub>1-x</sub>Sb<sub>x</sub> based THz QCL structure employing a 3-well resonant phonon depletion design showed laser emission at 3.8 THz. These results indicate that mixed As-Sb materials are promising candidates for the use in intersubband devices.



---

## Contents

---

<b>1</b>	<b>Introduction</b>	<b>1</b>
1.1	Outline . . . . .	3
<b>2</b>	<b>Crystals</b>	<b>5</b>
2.1	The Crystal lattice . . . . .	5
2.2	The 14 Bravais lattices . . . . .	6
2.3	Directions and Planes in Crystals . . . . .	7
2.4	III/V Semiconductors . . . . .	10
<b>3</b>	<b>Quantum Cascade Lasers</b>	<b>13</b>
3.1	Inter Subband Transitions in Semiconductor heterostructures . . . . .	13
3.2	Quantum Cascade Lasers . . . . .	15
3.3	State of the art QCLs . . . . .	19
<b>4</b>	<b>Molecular Beam Epitaxy of QCL Materials</b>	<b>21</b>
4.1	Epitaxy . . . . .	21
4.1.1	Lattice mismatch . . . . .	22
4.2	Crystal growth by Molecular Beam Epitaxy . . . . .	26
4.2.1	Ultra high vacuum conditions . . . . .	28
4.2.2	Evaporation of Source Materials . . . . .	29
4.3	Reactions during Molecular Beam Epitaxy (MBE) Growth . . . . .	32
4.3.1	Surface Reconstructions . . . . .	33
<b>5</b>	<b>Characterization of Epitaxial Layer Structures</b>	<b>37</b>
5.1	High Resolution X-Ray Diffraction . . . . .	37
5.1.1	Diffraction of X-Rays from Crystal Planes . . . . .	37

5.1.2	High Resolution X-Ray Diffraction (HRXRD) of hetero epitaxial layers . . . . .	41
5.2	Reflection High Energy Electron Diffraction . . . . .	44
5.3	Atomic Force Microscopy . . . . .	48
5.4	Energy Dispersive X-ray Spectroscopy . . . . .	50
<b>6</b>	<b>MBE growth of InAs-based QCLs</b>	<b>53</b>
6.1	Influence of the Effective Electron Mass . . . . .	53
6.2	Barrier Materials for InAs Based Quantum Cascade Lasers (QCLs) . . . .	55
6.3	$\text{Al}_{0.20}\text{In}_{0.80}\text{As}_y\text{Sb}_{1-y}$ Barrier determination . . . . .	57
6.4	$\text{Al}_{0.462}\text{In}_{0.538}\text{As}_y\text{Sb}_{1-y}$ . . . . .	59
6.5	MBE Growth of $\text{Al}_{0.462}\text{In}_{0.538}\text{As}_y\text{Sb}_{1-y}$ . . . . .	61
6.5.1	Influence of the Substrate Temperature . . . . .	64
6.5.2	Temperature limit for lattice matching . . . . .	65
6.5.3	Influence of $P_{\text{As}_2}$ . . . . .	66
6.5.4	SEM and EDX measurements on $\text{Al}_{0.462}\text{In}_{0.538}\text{As}_y\text{Sb}_{1-y}$ films . . . .	67
6.6	Discussion . . . . .	71
<b>7</b>	<b>GaAsSb as a Model System for Group V mixing</b>	<b>75</b>
7.1	The $\text{Ga}_{0.47}\text{In}_{0.53}\text{As}/\text{GaAs}_{0.51}\text{Sb}_{0.49}$ material system . . . . .	75
7.2	Crystal Quality of $\text{GaAs}_{1-x}\text{Sb}_x$ with Respect to the Substrate Temperature	77
7.3	Incorporation of Sb into $\text{GaAs}_{1-x}\text{Sb}_x$ . . . . .	80
7.3.1	Growth rate dependence of the Sb incorporation . . . . .	81
7.3.2	Temperature dependence of the Sb incorporation . . . . .	84
7.3.3	Crystal quality with respect to the growth rate . . . . .	84
7.4	Discussion . . . . .	86
<b>8</b>	<b>Low Temperature Grown InAs Based Intersubband Devices</b>	<b>89</b>
8.1	$\text{InAs}/\text{AlAs}_{1-x}\text{Sb}_x$ Quantum Cascade Detector . . . . .	89
8.2	$\text{InAs}/\text{AlAs}_{1-x}\text{Sb}_x$ Terahertz (THz)-QCL . . . . .	92
8.3	Discussion . . . . .	93
<b>9</b>	<b>Discussion and Outlook</b>	<b>95</b>
	<b>Bibliography</b>	<b>99</b>

# CHAPTER 1

## Introduction

The electromagnetic spectrum can coarsely be divided into the radio, microwave, infrared, visible, ultraviolet, x-ray and the gamma-ray regions. Of these regions, the infrared region, which spans from wavelengths from 300  $\mu\text{m}$  to 800 nm is of special interest for chemical sensing applications since vibrational and rotational modes of molecules reside in this region[1].

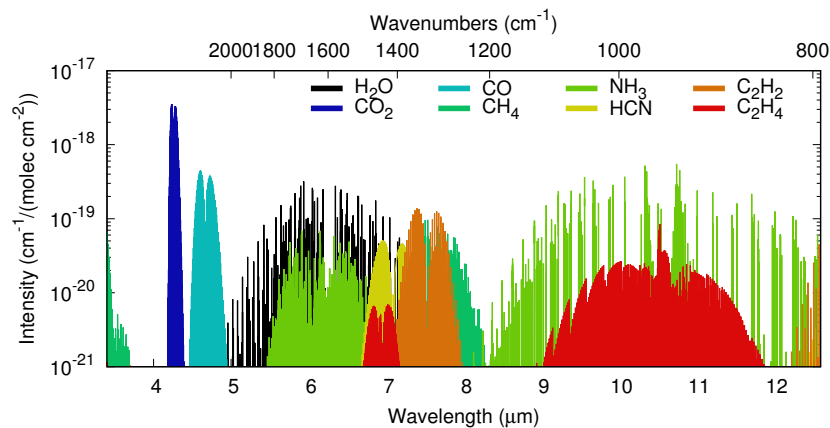


**Figure 1.1:** Absorption line intensities of different molecules. Data Taken from the HITRAN online database[2].

Figure 1.1 shows the absorption lines of selected molecules between 4  $\mu\text{m}$  and 12  $\mu\text{m}$ . The infrared region is commonly further divided into the far-Infrared (FIR) region which covers the wavelength range from 300  $\mu\text{m}$  to 15  $\mu\text{m}$ , the Mid-Infrared (MIR) region which is located between 15  $\mu\text{m}$  and 3  $\mu\text{m}$  and the near-Infrared (NIR) region, which covers the

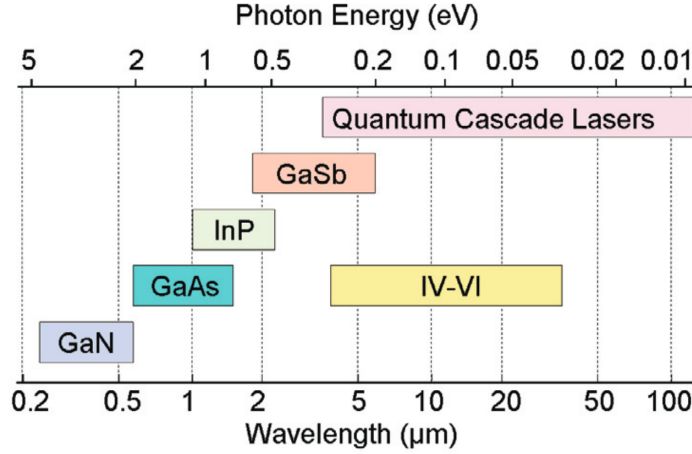


**Figure 1.2:** Spectral span of different semiconductor technologies. Taken from [3].

range from 3 μm to the edge of the visible spectrum at 800 nm. Due to the presence of absorption lines, light emitters and detectors which operate in these regions are of special interest for gas sensing, imaging, and medical applications[4].

Especially for portable and standoff-detection systems semiconductor devices are advantageous due to their size and power consumption. Figure 1.2 shows the spectral ranges different semiconductor technologies can span. Most notably, the development of GaAs[5, 6, 7] and III-nitride based[8] devices lead to the full coverage of the visible and the NIR regions. Since these lasers rely on interband transitions, the path towards the long wavelength side of the infrared spectrum lead to the use of materials with ever decreasing band gaps. However, due to the interband nature of the optical transition used in this type of laser, the band gap energy of the material is the fundamental lower limit for the energy of the generated photons. Lead-salts such as  $\text{Pb}_x\text{Sn}_{1-x}\text{Te}$  are the group of semiconductors with the smallest direct band gaps, however, especially in the THz region they show rather limited output power[9] and the smallest, emission frequencies which could be achieved are around 18 THz to 15 THz[10, 11].

The limitations imposed by the band gap, lead to the invention[12, 13], and later realization[14] of the QCL. In such a device, an optical transition takes place between two confined states in the same band, and hence, the emission wavelength is not defined by the band gap of the material, but solely by the design of a series of quantum wells. Its versatility makes the QCL an interesting device for sensing and spectroscopy applications in the MIR regime[15, 16, 17] where it enabled the monolithic integration of laser and detector on the same chip[18] while in the FIR regime, applications ranging from astronomy to telecommunications [19, 20] as well as THz imaging[21] have been developed.



Despite all its success, the operation of THz-QCLs still requires cryogenic cooling techniques. This drawback substantially limits the impact of this technology on real world applications. The development of new material systems is one possible route to achieve higher operation temperatures. InAs based devices may provide a substantial advantage over traditional GaAs based devices, due to the low effective electron mass in the well. Their growth, however, still provides significant challenges, especially since appropriate barrier materials require the mixing of group V elements. Understanding the growth of these materials is substantial to achieve high quality devices. Hence, the mechanism which influence the quality of the grown materials and the interactions between the precursors have to be investigated and understood in order to enhance the performance of these devices.

## 1.1 Outline

First, the basics of crystals and crystal structures are summarized in chapter 2. Thereafter, the working principle of the QCL and the influence of material properties are summarized in chapter 3. The principles of MBE are given in chapter 4 and an overview of important characterization techniques for epitaxially grown structures is given in chapter 5. Chapter 6 explains the motivation for the use of InAs as a well material, and the quaternary  $\text{Al}_x\text{In}_{1-x}\text{As}_y\text{Sb}_{1-y}$  alloy as a barrier material for THz-QCLs. Thereafter, the efforts to optimize the crystal quality of this material are described. In chapter 7 the mixing of group V elements in III/V compound semiconductors is analyzed using  $\text{GaAs}_{1-x}\text{Sb}_x$  as a model system. Finally the optimization strategies, developed in the previous chapters, are evaluated by applying the results to intersubband devices in chapter 8.



The physical properties of a solid do not only depend on the atoms it is composed of but they are also strongly influenced by the arrangement of these atoms. Hence, solids can be classified with respect to this arrangement i.e. how well ordered its atoms are. If this order is only on a length scale comparable to the distance between the atoms the solid is said to be amorphous. This kind of arrangement is characteristic for glasses. If the order of the atoms, however, is persistent on a length scale much larger than the interatomic distance we are talking about crystals[22]. Since the crystal structure of materials like Si and GaAs is responsible for their semiconducting behavior and influences many aspects of their production and processing, a few basic points about crystals shall be presented in this chapter.

### 2.1 The Crystal lattice

The positions at which atoms reside within a crystal are called the crystal lattice. Due to the periodic arrangement of the atoms the whole crystal is defined by only a few vectors. In a cubic lattice (figure 2.1(a)), for example, the three vectors

$$\vec{a} = a \begin{pmatrix} 1 \\ 0 \\ 0 \end{pmatrix} = a\vec{e}_x; \quad \vec{b} = a \begin{pmatrix} 0 \\ 1 \\ 0 \end{pmatrix} = a\vec{e}_y; \quad \vec{c} = a \begin{pmatrix} 0 \\ 0 \\ 1 \end{pmatrix} = a\vec{e}_z, \quad (2.1)$$

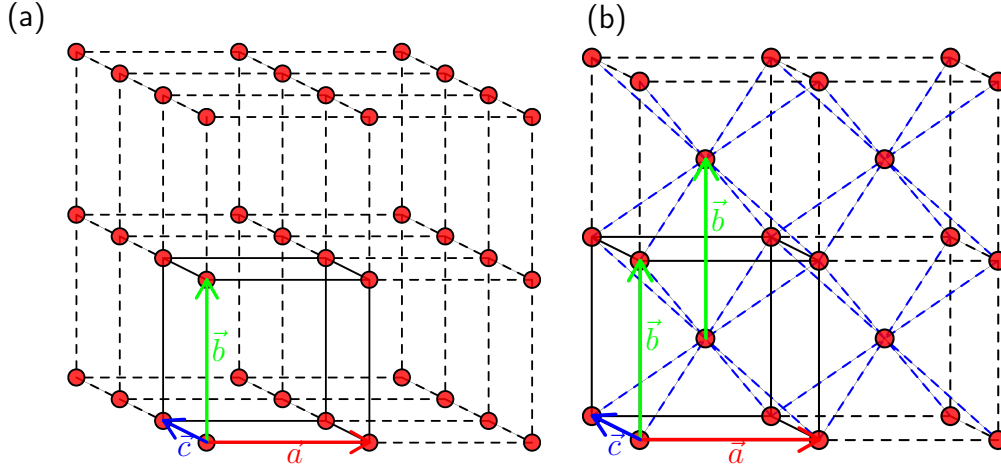


**Figure 2.1:** A simple cubic and a body centered cubic lattice. Applying one of the lattice vectors to any lattice site will give the position of another lattice site.

where  $a$  is the inter-atomic distance, define all positions, or lattice sites, at which atoms can be found. Applying one of these vectors at any point of the lattice will give the position of another lattice site.

These vectors, which are not necessarily orthogonal or of the same length, can also be described by their lengths  $(a, b, c)$  and the angles between them  $(\alpha, \beta, \gamma)$ . Since these six parameters describe the complete lattice, they are called lattice parameters or lattice constants. The parallelepiped that is defined by the 3 vectors  $\vec{a}, \vec{b}, \vec{c}$  is called the unit cell of the lattice. This means that the whole crystal can be constructed by repeating the unit cell in all three dimensions.

## 2.2 The 14 Bravais lattices

In the most simple case the lattice is described by three orthogonal vectors of the same length and has one lattice site at each of the eight corners of the unit cell. This lattice is called the simple cubic lattice. Since the atoms at each corner of the unit cell are shared with 7 adjacent cells there is exactly  $N = \frac{8}{8} = 1$  atom per unit cell in this crystal and one lattice site for this type of lattice.

There are other cubic lattices, however, which have more than one lattice site per unit cell. If there is an additional lattice site in the center of there unit cell we call this lattice body centered cubic. This lattice structure has exactly  $N = \frac{8}{8} + 1 = 2$  lattice sites per unit cell. In the third type of cubic lattice additional lattice sides are placed in the centers of the 6 faces of the unit cell. Since each of these sided is shared with one adjacent cell we have in total  $N = \frac{8}{8} + \frac{6}{2} = 4$  lattice sites.

As shown in figure 2.1(b), applying one of the lattice vectors to any of the additional sites will also give the position of another lattice site. Hence, the lattice vectors and the unit cell is all the information which is needed to construct the whole lattice.

With respect to the six lattice parameters  $a, b, c$  and  $\alpha, \beta, \gamma$  seven types of crystal systems can be distinguished. If all three lattice vectors are orthogonal, we can distinguish three crystal systems depending on the number of lattice vectors of the same length. As we have already seen, a lattice with three lattice vectors of the same length is called cubic ( $a = b = c$ ). If only two of the vectors are of the same length the lattice is called tetragonal ( $a = b \neq c$ ). Finally if all three vectors have a different length the lattice is called orthorhombic ( $a \neq b \neq c$ ).

Three more crystal systems exist in which at least one of the angles  $\alpha, \beta, \gamma$  is not equal to  $\frac{\pi}{2}$ . If the three lattice vectors have the same length ( $a = b = c$ ) and the same angles between them ( $\alpha = \beta = \gamma \neq \frac{\pi}{2}$ ) the lattice is called rhombohedral. If only one angle differs from  $\frac{\pi}{2}$  ( $\alpha \neq \frac{\pi}{2}, \beta = \gamma = \frac{\pi}{2}$ ) the lattice is called monoclinic. If all angles and all distances are different ( $a \neq b \neq c; \alpha \neq \beta \neq \gamma$ ) the lattice is called triclinic. Finally the hexagonal lattice has two different angles  $\alpha = \frac{\pi}{2}$  and  $\gamma = \frac{\pi}{3}$  and two lattice vectors of different length ( $a \neq c$ ).

Of some of these seven crystal systems body-centered, face-centered or base-centered modifications exist which lets us distinguish in total 14 different lattices. Already in 1850 it has been shown by the french crystallographer Auguste Bravais that in three dimensions only these 14 point lattices, nowadays called Bravais lattices, exist[23, 24]. All 14 Bravais lattices are shown in figure 2.2.

## 2.3 Directions and Planes in Crystals

The physical properties of a crystal can be strongly anisotropic. Figure 2.4 shows (100), (110) and (111) planes in a simple cubic lattice. It can be seen that the configuration of the atoms on these planes is fairly different, and it is obvious that each of them may exhibit different properties. Hence, it is important to distinguish directions and planes in a crystal. Any plane which goes through the origin of the crystal lattice will intercept with other points of the lattice at regular intervals. Since the crystal can be considered to extend to infinity, for each plane there is a set of parallel planes which are indistinguishable from the original plane. To identify such a set of planes in a lattice, the intercepts between the plane and the axes of the unit cell are obtained as shown in figure 2.3[25]. In this example we find the fractions of the lattice constant of the intercepts to be  $d_x = \frac{1}{2}, d_y = 1$  and  $d_z = \frac{1}{4}$ .

## 2.3. Directions and Planes in Crystals

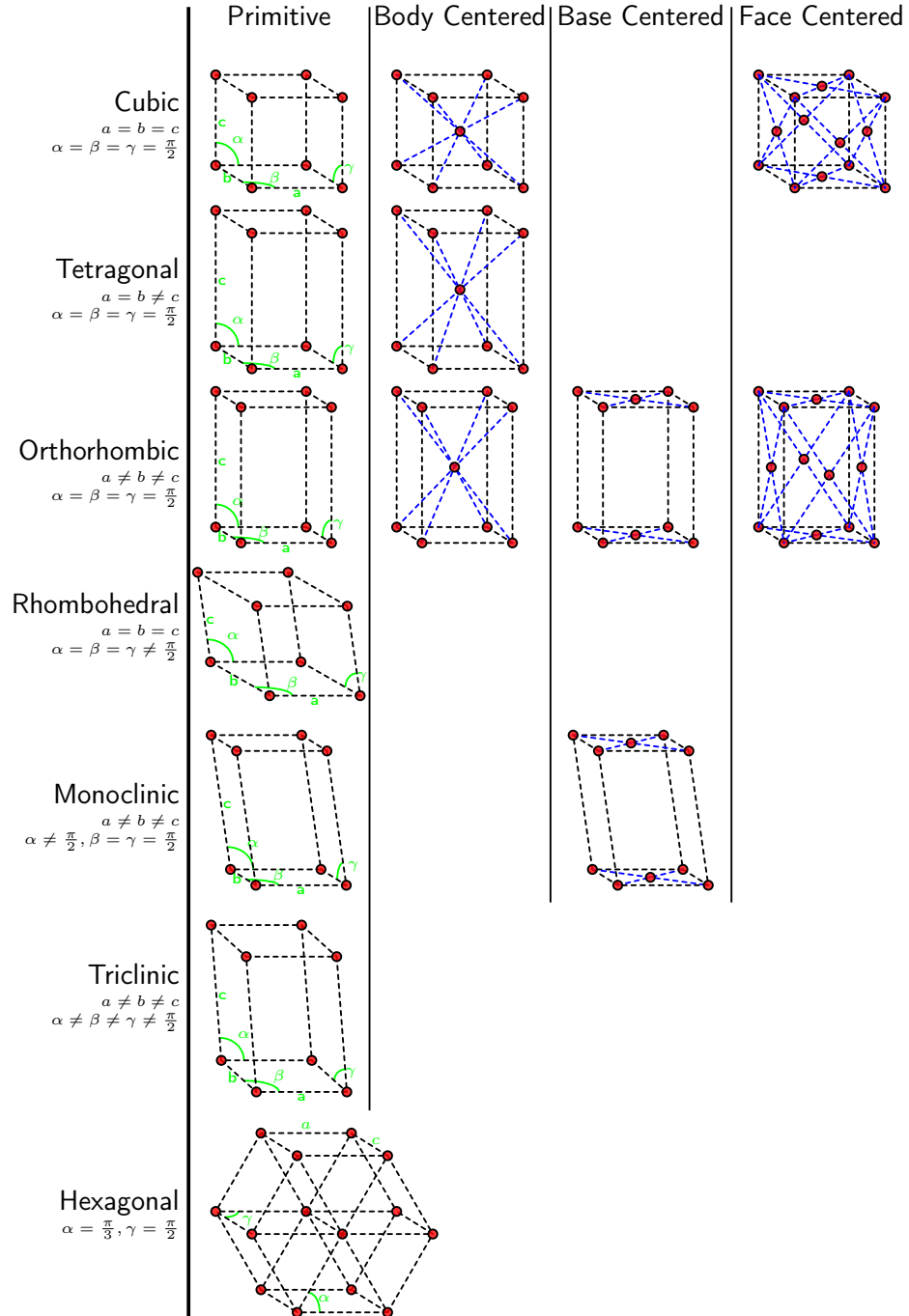


**Figure 2.2:** The 14 Bravais lattices

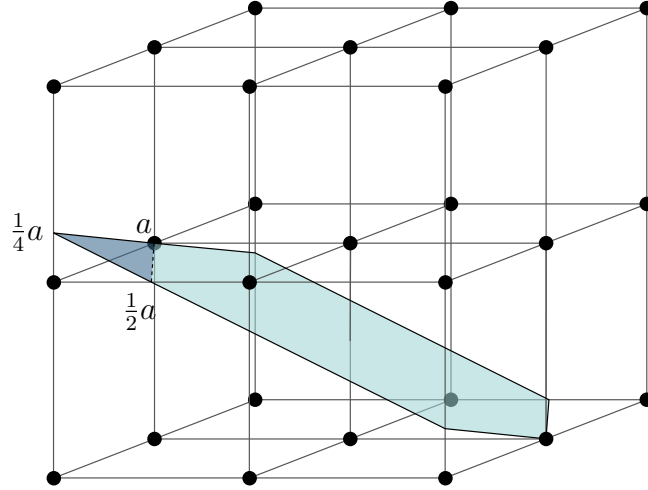


**Figure 2.3:** Derivation of the Miller indices of a plane. From the intersections between the plane and the axes of the unit cell the Miller indices of the plane are derived.

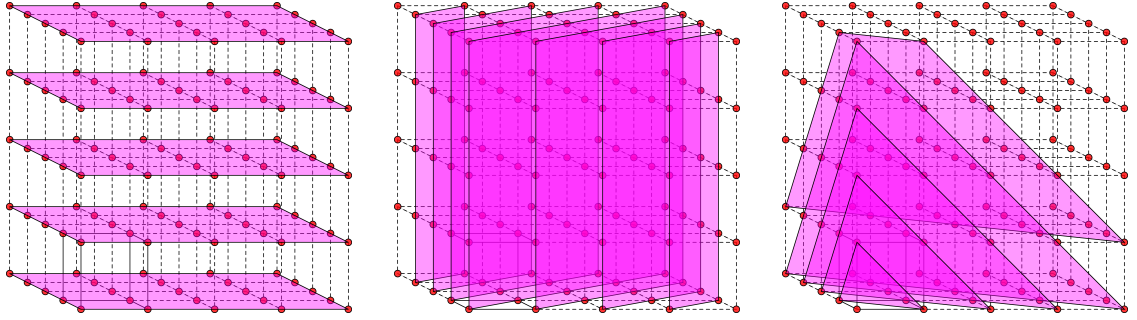


**Figure 2.4:** (100), (110) and (111) planes in a simple cubic lattice.

We can now find an integer  $s$ , such that the products  $d_i s$  are the smallest integer values. In our example, for  $s = 4$  we find

$$\begin{aligned} h &= d_x s = \frac{1}{2} s = 2 \\ k &= d_y s = 1 s = 4 \\ l &= d_z s = \frac{1}{4} s = 1. \end{aligned} \tag{2.2}$$

These values are called the Miller indices of the plane and are denoted in parenthesis  $(hkl)$  or in our example  $(241)$ . If the plane is parallel to one of the crystal axes the intercept will be at infinity and the respective miller index is 0. A negative index is denoted by a bar above the number, e.g.  $(\bar{2}41)$ .

Some of the planes in a crystal can be equivalent due to the symmetry of the lattice. In a simple cubic lattice for example the  $(100)$ ,  $(010)$ ,  $(001)$ ,  $(\bar{1}00)$ ,  $(0\bar{1}0)$  and  $(00\bar{1})$  are indistinguishable and are denoted as  $\{100\}$  planes.

## 2.4. III/V Semiconductors

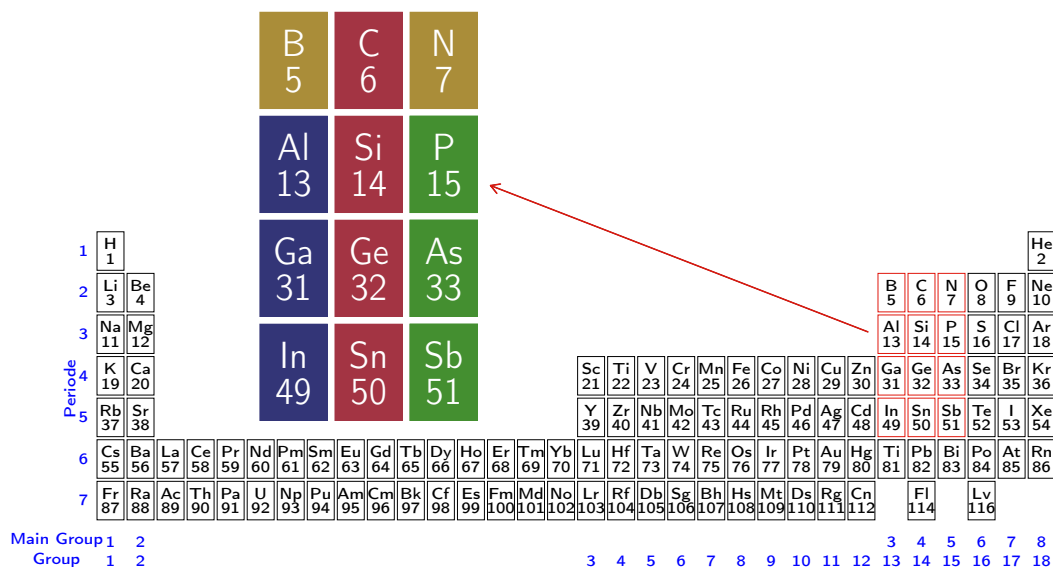


**Figure 2.5:** Elements which form III/V compound Semiconductors. These compounds are formed of one or more elements of the group III (Al,Ga,In), highlighted in blue, and one or more elements of the group V (P,As,Sb), shown in green. Compounds containing N are usually referred to as nitrides due to their distinct properties. Also III/V semiconductors containing B exist, however, they are less commonly used for optical devices. The elemental semiconductors Si,Ge and Sn are found in group V and highlighted in red.

In the same way in which we can define planes in the crystal, we can also define directions. These directions are denoted in square brackets (e.g.  $[hkl]$ ) defined such that the direction  $[hkl]$  is orthogonal to the  $(hkl)$  plane. If equivalent directions exist, they are denoted by angle brackets (e.g.  $\langle 100 \rangle$ ).

## 2.4 III/V Semiconductors

Semiconductors can be grouped into elemental semiconductors such as Si, Ge and Sn, which are found in the fourth main group of the periodic table, and compound semiconductors which consist of combinations of elements from the main groups III and V, II and VI or IV and VI.

In this work we will concentrate on the compound semiconductors consisting of elements from group III and V since they are the basic building blocks for intersubband devices such as QCLs. Figure 2.5 shows these elements. III/V semiconductors consist of one or more elements of the main group III and one or more elements of the main group V. Usually when we refer to III/V semiconductors we are talking about combinations of Al,Ga and In and P,As and Sb such as GaAs or InSb. Compounds with N are usually excluded from this group since their distinct properties justify the treatment as separate group. III/V



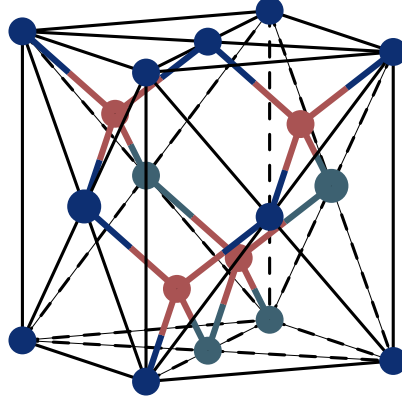


**Figure 2.6:** The zincblende crystal structure. This crystal structure consists of two face centered cubic sublattices which are displaced in direction of the body diagonal by one quarter of its length and each of the sublattices is occupied by atoms of a different main group i.e. there is a group III (blue) and a group V (red) sublattice.

semiconductors crystallize in the zincblende crystal structure which is shown in figure 2.6. This crystal structure consists of two face centered cubic sublattices, of which each is occupied by atom species of a distinct main group. The two sublattices are shifted in direction of the body diagonal of the unit cell by one quarter of its length and the unit cell contains four atoms of each main group. Although bulk crystals of these compounds usually have zincblende structure, there also exists the wurtzite configuration which can be found in nanostructures of these materials[26].

While each sublattice is reserved for elements from one of the two groups, atom species from the same group can be mixed in the particular sublattice. Depending on the number of different atom species these alloys are referred to as binary, ternary, or quaternary compounds and so forth. Figure 2.7 shows the lattice constants and band gap of selected III/V semiconductors. The binary alloys, which are indicated by circles, can be used as substrates for epitaxy since they are available as high quality wafers. The lines connecting the binary alloys show the lattice constants and band gap of ternary alloys, e.g.  $\text{GaAs}_{1-x}\text{Sb}_x$  is connecting GaAs and GaSb,  $\text{Al}_x\text{In}_{1-x}\text{As}$  is indicated by the line connecting AlAs and InAs and so forth. The faces which are enclosed by these lines indicate quaternary and quaternary alloys which are composed of the binary alloys at the corners of the face, e.g. AlAs, GaAs and InAs form the quaternary  $\text{Al}_x\text{Ga}_y\text{In}_{1-x-y}\text{As}$  alloy.

The properties of the particular alloy are given by an, in the most simple case linear, combination of the properties of the involved binary alloys known as Vegard's law[27]. A summary of the most important parameters of common III/V semiconductors can be found in refs [28], [29], [30] and [31].

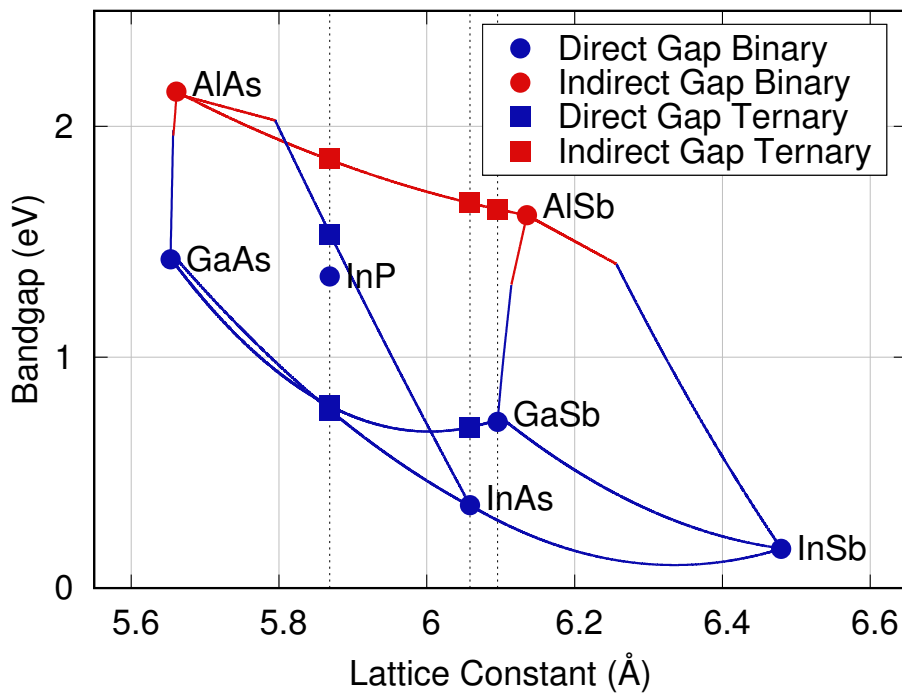


**Figure 2.7:** Band gap and lattice constant of selected III/V semiconductors. Binary alloys are indicated by circles. The lines connecting binaries which have one common component indicated ternary alloys. Faces which are enclosed by ternary alloys are quaternary or quinary alloys.

In traditional band gap lasers an optical transition from the conduction to the valence band is used to create light emission. In such structures the band gap energy is the fundamental lower limit for the energy of the emitted light. In a semiconductor heterostructure, however, it is possible to design electronic subbands such that an optical transition within the same band, called an intersubband transition, can be achieved. Not only is the energy of such a transition not limited by the energy of the band gap of the material, it can also be tailored to generate photons of a specific energy.

A device which makes use of this property is the Quantum Cascade Laser (QCL) which was theoretically envisioned by Kazarinov and Suris in 1971[12] and first demonstrated by Faist et. al. in 1994[14].

### 3.1 Inter Subband Transitions in Semiconductor heterostructures

Band gap lasers produce light via an optical transition from the conduction band to the valence band as shown in figure 3.1 (a). The transition energy is given by the sum of the band gap energy of the well material and the confinement energies of the electron and hole states,

$$E_{12} = E_{e1} + E_g + E_{h1} \quad (3.1)$$

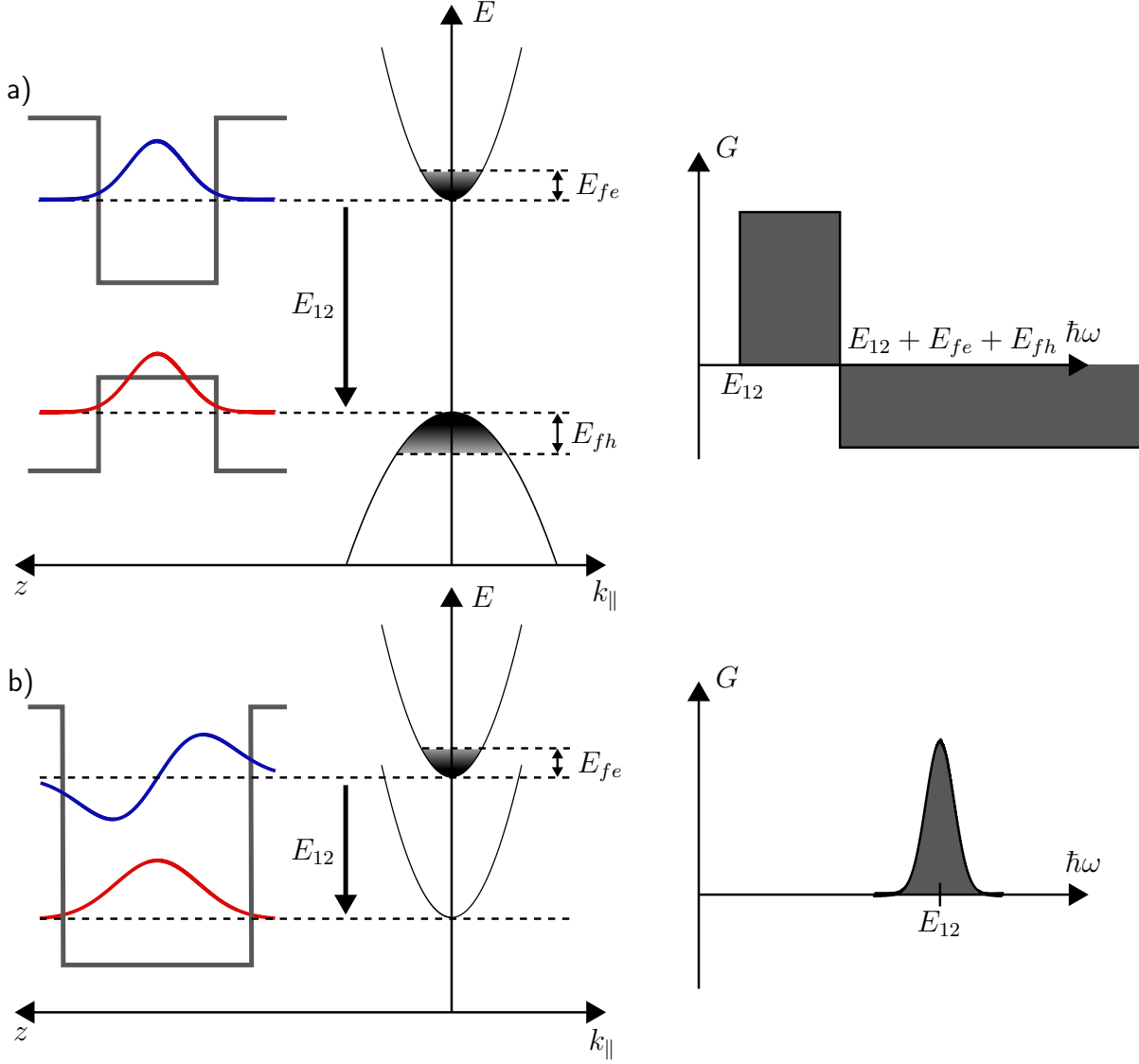


**Figure 3.1:** Comparison of interband and intersubband transitions. The interband transition (a) occurs between a state in the conduction- (electrons) and valence band (holes). The energy difference is given by the sum of the band gap energy and the two confinement energies. Due to the distributions of electrons and holes in the two bands the gain spectrum is broadened. For high energies the interband system shows absorption. The intersubband transition (b) occurs between two states within either the conduction or the valence band. The energy difference  $E_{12}$  is solely defined by the confinement energies of the two states. Since both states show the same in-plane dispersion, ideally the gain spectrum would be infinitely sharp and centered around  $E_{12}$ , however, factors like nonparabolicity lead to a broadening of the gain spectrum. After [32].

and the band gap of the well material is the upper limit for the energy of the generated photons. For photons with an energy below  $E_{12}$  the material is transparent. For energies between  $E_{12}$  and  $E_{12} + E_{fe} + E_{fh}$  inversion in the material can be achieved and gain is observed. At higher energies electrons can be excited from the valence into the conduction band and the material is absorbing. In contrast, in an intersubband structure, shown in figure 3.1 (b), the optical transition takes place between two subbands within either the conduction or the valence band and the energy of the transition is solely defined by the confinement energies of the two states and for an infinitely wide quantum well this energy goes to zero. Since the two states are in the same band, both have the same in-plane dispersion and the gain spectrum shows a sharp line at  $E_{12}$ . Due to broadening of the two levels and the nonparabolicity of the dispersion this line can be broadened.

Since the two subbands show the same dispersion, electrons are easily scattered between the upper and lower state. Due to this, the upper state lifetime in intersubband systems is only on the order of pico seconds. In contrast, the upper state lifetime in an interband system can go as high as a few nano seconds.

## 3.2 Quantum Cascade Lasers

A device which exploits intersubband transitions for the generation of light is the QCL. It consists of a periodic structure in which active cells are connected by injector regions. As shown in figure 3.2, the active cell is designed such that a three-level system is created, in which the highest level  $|3\rangle$  is the upper laser level,  $|2\rangle$  is the lower laser level, and  $|1\rangle$  is the ground state. An electron which enters the active cell of period  $N$  undergoes an optical transition from state  $|3\rangle$  to  $|2\rangle$ . Finally the electron reaches the injector of period  $N$  via  $|1\rangle$  and travels to period  $N + 1$  where it is again injected into the upper laser state.

The gain in a QCL structure can be approximated from the intersubband transition probabilities induced by an electromagnetic wave[33]. The interaction between an optical mode in the laser resonator and the electronic states is accounted for by adding a perturbative interaction term to the Hamiltonian of the electronic states  $H_0$

$$H = H_0 + H_{int}. \quad (3.2)$$

The interaction term is then derived from the kinetic energy term for a charged particle in an electromagnetic field, which is given by

$$H = \frac{(\vec{p} - e\vec{A})^2}{2m}. \quad (3.3)$$

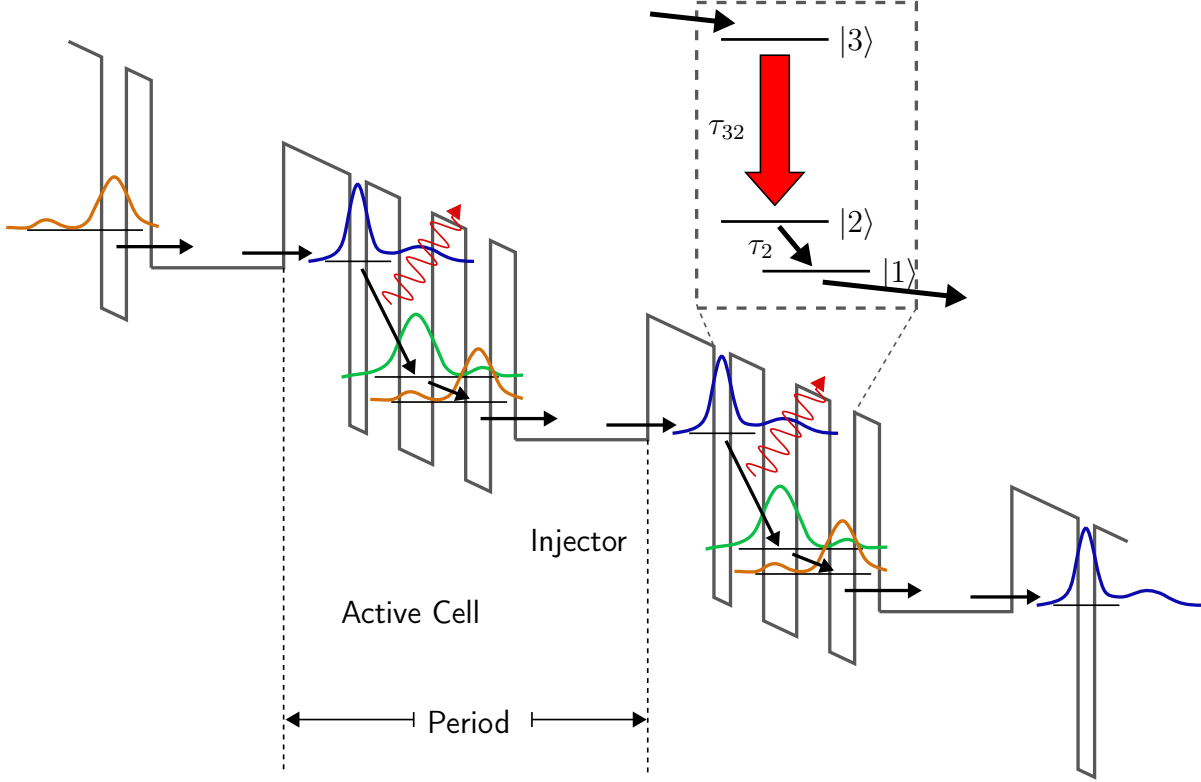


**Figure 3.2:** Conduction band diagram of a QCL. The QCL consists of a repetition of periods which are composed of an active cell and an injector region. The active cell is designed such that a three-level system is formed as shown in the inset. The optical transition happens between states  $|3\rangle$  and  $|2\rangle$  with the intersubband scattering rate  $r_{32} = \tau_{32}^{-1}$ . Electrons in the lower laser level are depleted into ground state with the scattering time  $\tau_2$ . From the ground state the electron reach the injector and finally the upper laser state of the next period. After?

After expanding this term gives

$$H = \frac{\vec{p}^2}{2m} - \frac{e}{2m}(\vec{p} \cdot \vec{A} + \vec{A} \cdot \vec{p}) + \frac{e^2}{2m} \vec{A}^2 \quad (3.4)$$

and using  $\vec{p} = -j\hbar\nabla$  and applying the Coulomb gauge ( $\nabla \cdot \vec{A} = 0$ ) we get

$$H = \frac{\vec{p}^2}{2m} - \frac{ie\hbar}{m} \vec{A} \cdot \nabla + \frac{e^2}{2m} \vec{A}^2. \quad (3.5)$$

For low intensities ( $\vec{A}^2 \ll$ ) we find the interaction term to be

$$H_{int} = -\frac{e}{m} \vec{A} \cdot \vec{p}. \quad (3.6)$$

We consider  $\vec{A}$  to be a plane wave polarized in the  $z$  direction with the angular frequency

$\omega$  and the propagation vector  $\vec{k}$

$$\vec{A} = -\frac{E_0}{2\omega} \vec{e}_z (e^{j(ky+\omega t)} - e^{-j(ky+\omega t)}). \quad (3.7)$$

The transition rate of electrons from the initial state  $i$  to the final state  $f$  can be calculated using Fermi's golden rule

$$W_{if} = \frac{2\pi}{\hbar} \sum |\langle i|H_{int}|f \rangle|^2 \delta(E_f - E_i - \hbar\omega). \quad (3.8)$$

Since the wavelength of the optical mode can be considered large compared to the atomic distance, the spacial dependence of the vector potential  $\vec{A}$  is neglected and taken outside of the matrix element. This is referred to as dipole approximation.

$$\langle i|H_{int}|f \rangle = -\frac{e}{m} \vec{A} \langle i|\vec{p}|f \rangle \quad (3.9)$$

The matrix element of the momentum can be related to the matrix element of the position via

$$\langle i|\vec{p}|f \rangle = jm\omega \langle i|z|f \rangle \quad (3.10)$$

and hence the transition rate reads

$$W_{if} = \frac{\pi}{2\hbar} E_0^2 e^2 \sum |\langle i|z|f \rangle|^2 \delta(E_f - E_i - \hbar\omega). \quad (3.11)$$

In reality, the subbands  $i$  and  $f$  will not be infinitely sharp but will show a certain line width  $\gamma$ . Hence, we replace the delta function by a lorentzian function

$$W_{if} = \frac{\pi}{2\hbar} E_0^2 e^2 \sum |\langle i|z|f \rangle|^2 \frac{\frac{\gamma}{\pi}}{(E_f - E_i - \hbar\omega)^2 + \gamma^2}. \quad (3.12)$$

which has a maximum at  $\hbar\omega = E_f - E_i$  of

$$W_{if}^{\max} = \frac{\pi}{2\hbar\gamma} E_0^2 e^2 |\langle z_{if} \rangle|^2, \quad (3.13)$$

where  $\langle z_{if} \rangle$  is a short hand for the matrix element of the transition from  $i$  to  $f$ .

The gain in an optical material can be defined as the change in the photon flux over the total photon flux in the medium,

$$G = \frac{1}{\Phi} \frac{d\Phi}{dy}, \quad (3.14)$$

### 3.2. Quantum Cascade Lasers

---

where  $g$  is the gain coefficient,  $J$  is the current density and  $\Phi$  is the photon flux from the incident wave  $\vec{A}$ , given by

$$\Phi = \frac{\epsilon_0 n c E_0^2}{2\hbar\omega} w L, \quad (3.15)$$

with  $w$  being the width and  $L$  height of the medium.

The change in the photon flux is given by

$$\frac{d\Phi}{dy} = W_{32}^{\max} w (n_3 - n_2), \quad (3.16)$$

where  $n_3$  is the number of electrons in the upper- and  $n_2$  that in the lower state. By combining equations 3.13, 3.15 and 3.16 we find

$$G = \frac{\omega e^2 |\langle z_{if} \rangle|^2}{\epsilon_0 n c L_p} (n_3 - n_2). \quad (3.17)$$

In an electrically pumped system as a QCL the number of electron in the upper state is given by

$$n_3 = \eta_i \frac{J}{e} \tau_3, \quad (3.18)$$

where  $\eta_i$  is the injection efficiency,  $J$  is the current density and  $\tau_3$  is the lifetime in the upper state. If we furthermore assume that the lower laser state can only be populated by electrons from the upper state, the number of electrons in the lower laser state is given by

$$n_2 = n_3 \frac{\tau_2}{\tau_{32}}, \quad (3.19)$$

with  $\tau_2$  being the lifetime in the lower laser state and  $\tau_{32}$  being the scattering time from the upper to the lower state.

By inserting equations 3.18 and 3.19 into equation 3.17 and normalizing by the current density we get

$$g_c = \frac{\omega e |\langle z_{if} \rangle|^2}{\epsilon_0 n c L_p} \eta_i \tau_3 \left( 1 - \frac{\tau_2}{\tau_{32}} \right), \quad (3.20)$$

which is referred to as the gain coefficient of the material.

In order to achieve light emission from a QCL the gain in the material has to compensate for the losses in the cavity. The point at which this happens is called threshold current density and is given by

$$J_{th} = \frac{\alpha_w + \alpha_m}{g_c \Gamma}, \quad (3.21)$$

where  $\alpha_w$  and  $\alpha_m$  are the waveguide and the mirror losses respectively, and  $\Gamma$  is the confinement factor of the optical mode.



### 3.3 State of the art QCLs

After their first demonstration in 1994 QCLs have went through a rapid development. In the mid MIR region, Continuous Wave (cw) operation of these devices at low temperatures could be demonstrated in 1996[34], the same year room temperature operation in pulsed mode[35] was demonstrated, but it took until 2002 for room-temperature cw operation to be demonstrated[36]. Up until now QCLs with emission wavelength from 2.75  $\mu\text{m}$  to 24  $\mu\text{m}$ [37, 38] have been demonstrated, and room-temperature cw operation is possible for almost the entire spectral range. Reviews on this topic can be found in [39] and [40].

While QCLs have been heavily optimized in the MIR region, equally high performance is yet to be shown in the region on the low energy side of the Reststrahlen band. In 1998 the first QCL in the GaAs/ $\text{Al}_x\text{Ga}_{1-x}\text{As}$  material system was shown[41]. In 2002 this technology enabled the first laser performance in this region, also called the THz region[42]. Since then, extensive research helped to extend the emission wavelength of these devices to a window from 1.2 THz to 4.9 THz and enabled a maximum operation temperature of  $\sim 200\text{ K}$ [43]. Nevertheless, THz-QCLs are still a very active field of research in order to enable higher operation temperatures and to allow for higher output powers. Optimized active regions[44], second harmonic generation[45, 46, 47], special waveguides[48, 49, 50, 51] and new materials systems[52, 53, 54] are explored to further enhance the performance.

A summary of the peak operation temperature and the respective emission wavelength is given in figure 3.3.

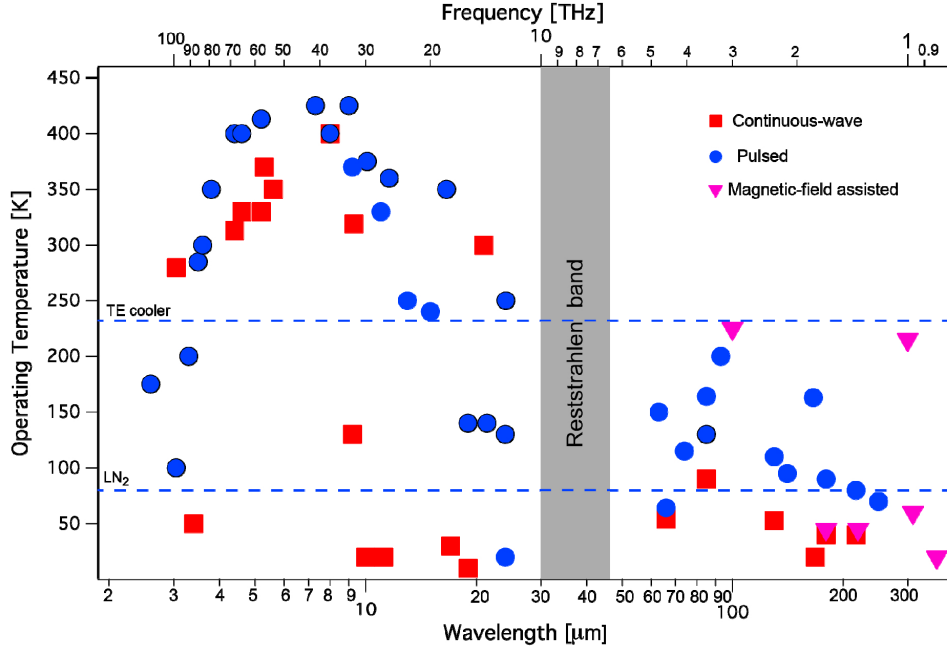


**Figure 3.3:** Maximum operation temperature and operation wavelength of QCLs. The two dashed horizontal lines indicate the limit for  $\text{LN}_2$  and thermoelectric cooling. On the high energy side of the Reststrahlen band we find both pulsed and cw operation up to temperatures around 400 K for a very broad range of wavelength. On the low energy side, the maximum operation temperature demonstrated so far without applying a magnetic field is just under 200 K. Taken from [40].

---

### Molecular Beam Epitaxy of QCL Materials

---

As we have seen in chapter 3, QCLs consist of alternating layers of semiconductors with thicknesses in the range of nanometers. The high degree of precision and uniformity, which is necessary for such complex devices can be achieved by MBE. Although there are competing techniques, *e.g.* Metal-Organic Chemical Vapor Deposition (MOCVD), QCLs operating in the THz have so far only be grown successfully by MBE. In this chapter the working principle of this technique will be explained. This chapter does not intend to provide a complete overview of this very extensive topic, but rather provide the background which is necessary to follow the explanations given in the following chapters.

#### 4.1 Epitaxy

When atoms are deposited onto a crystal template they may order such that the newly grown part is indistinguishable from the template. This process is called (homo-) epitaxy from old Greek *epi* for on top of and *taxis* for ordering. Also atoms which are different from those forming the template crystal, also referred to as substrate, may order on its surface. This process is called hetero-epitaxy. If the material of the layer is very similar to the substrate, i.e. they have the same crystal structure and a similar lattice constant, the growth of high quality epitaxial layers is possible.

The growth of high quality heteroepitaxial layers is the basis for the production of quantum well structures as they are described in chapter 3. III/V semiconductors, which crystallize in the zincblende crystal structure, are the dominant group of materials for the

Material	$C_{11}$	$C_{12}$	$C_{44}$
AlAs	12.02	5.7	5.89
GaAs	11.9	5.34	5.96
InAs	8.3	4.5	4.0
AlSb	8.77	4.08	4.34
InSb	6.67	3.65	3.02
GaSb	8.83	4.02	4.32
InP	10.11	5.61	4.56

**Table 4.1:** Stiffness coefficients for selected III/V semiconductors. All values in  $1 \times 10^{10}$  Pa. Taken from [31, 30].

production of QCLs. Hetero-epitaxy of these materials is a very elaborate topic, however, composition control and lattice matching can still be a challenging especially for materials containing both As and Sb.

#### 4.1.1 Lattice mismatch

When a layer of a material is grown on an substrate which has a different lattice constant, the atoms in the layer will be forced to align with the atoms in the substrate such that layer and substrate have the same in-plane lattice constant. This deformation leads to strain in the grown layer. The strain on a cubic crystal structure as a result to the applied stress is given by

$$\begin{pmatrix} \sigma_{xx} \\ \sigma_{yy} \\ \sigma_{zz} \\ \sigma_{yz} \\ \sigma_{xz} \\ \sigma_{xy} \end{pmatrix} = \begin{pmatrix} C_{11} & C_{12} & C_{12} & - & - & - \\ C_{12} & C_{11} & C_{12} & - & - & - \\ C_{12} & C_{12} & C_{11} & - & - & - \\ - & - & - & C_{44} & - & - \\ - & - & - & - & C_{44} & - \\ - & - & - & - & - & C_{44} \end{pmatrix} \begin{pmatrix} \epsilon_{xx} \\ \epsilon_{yy} \\ \epsilon_{zz} \\ \epsilon_{yz} \\ \epsilon_{xz} \\ \epsilon_{xy} \end{pmatrix} \quad (4.1)$$

where  $\sigma_{ij}$  are components of the stress tensor,  $\epsilon_{ij}$  are components of the strain tensor and  $C_{ij}$  are the stiffness coefficients of the material[55]. Stiffness coefficients for selected materials are given in table 4.1.

The strain component for the crystal direction  $i$  is given by

$$\epsilon_{ii} = \frac{a_i^L - a_0^L}{a_0^L} \quad (4.2)$$

where  $a_0^L$  is the native lattice constant of the layer and  $a_i^L$  is the strained lattice constant in direction  $i$ .

For growth along the [001] direction and biaxial stress applied in the x and y directions due to a substrate with the lattice constant  $a_0^S$  we can conclude

$$a_x^L = a_y^L = a_0^S \Rightarrow \epsilon_{xx} = \epsilon_{yy} = \epsilon_{\parallel} = \frac{a_0^S - a_0^L}{a_0^L}. \quad (4.3)$$

In this case the stress component in growth direction  $\sigma_{zz}$  is zero and the respective strain component  $\epsilon_{zz}$  is given by

$$\sigma_{zz} = 2C_{12}\epsilon_{\parallel} + C_{11}\epsilon_{zz} = 0 \quad (4.4)$$

from which the out-of-plane lattice constant of the layer

$$a_z^L = a_{\perp}^L = a_0^L - \frac{2C_{12}}{C_{11}}(a_0^S - a_0^L) \quad (4.5)$$

can be calculated.

We see that this type of biaxial stress applied to the layer due to the lattice constant mismatch with the substrate leads to a tetragonal distortion of the crystal since

$$a_x^L = a_y^L \neq a_z^L. \quad (4.6)$$

A layer which is distorted in such a way is referred to as pseudomorphic.

The situation is depicted in figure 4.1. If a layer with a native lattice constant  $a_0^L$  is deposited onto a substrate with a smaller lattice constant  $a_0^S$ , the layer will experience compressive stress and hence, the in-plane lattice constant of the layer will be compressed, while its out-of-plane lattice constant will be extended. On the other hand, deposition of a layer with a native lattice constant smaller than that of the substrate will lead tensile stress and hence, an extension of the in-plane lattice constant, while the out-of-plane lattice constant will be compressed.

If the crystal is distorted in such a way, strain energy is introduced into the layer. The areal density of the introduced strain energy is given by

$$\frac{E}{A} = 2h_l G \epsilon_{\parallel}^2 \frac{1 + \nu}{1 - \nu} \quad (4.7)$$

where  $h_l$  is the thickness of the layer,  $G$  is the shear modulus and  $\nu$  is Poisson's ratio of the material which is given by

$$\nu = \frac{C_{12}}{C_{11} - C_{12}} \quad (4.8)$$

for stress along the axis of the unit cell in cubic materials. We see that the areal strain en-

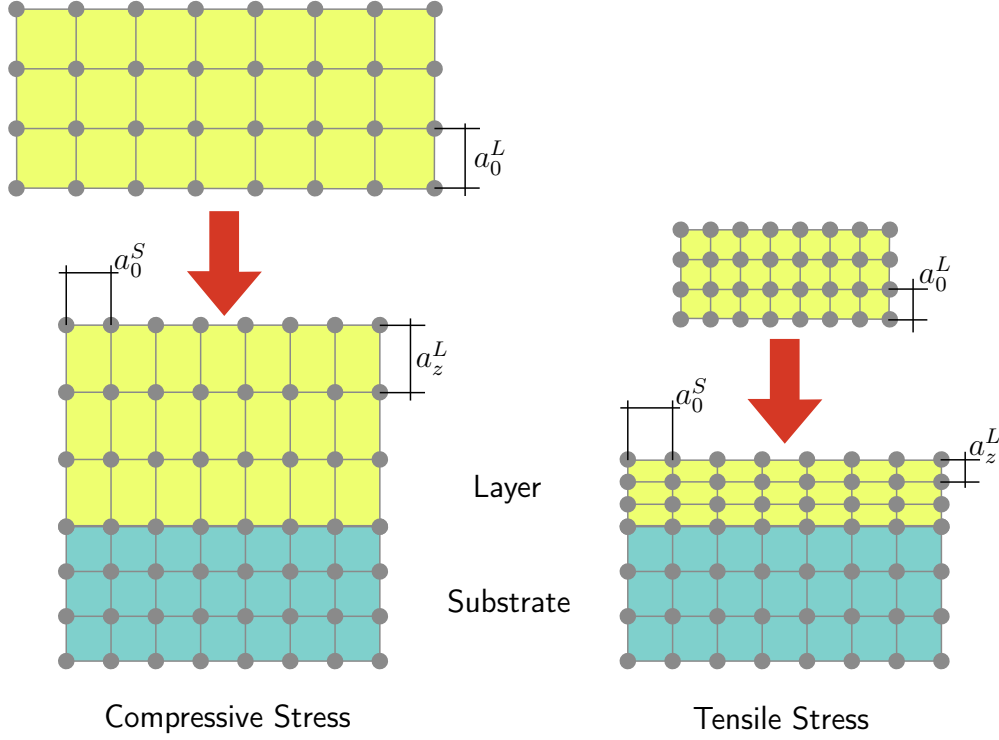


**Figure 4.1:** Tensile and compressive stress applied to an epitaxial layer. If a layer with a native lattice constant  $a_0^L$  larger than the lattice constant of the substrate  $a_0^S$  is deposited, its in-plane lattice constant will be compressed while its out-of-plane lattice constant will be extended. If, on the other hand, the lattice constant of the layer smaller than that of the substrate, its in-plane lattice constant will be extended while its out-of-plane lattice constant will be compressed. In both cases the native cubic crystal structure of the layer material is distorted into a tetragonal lattice.

ergy density increases linearly with the thickness of the layer for a given lattice mismatch. The thickness at which the areal strain energy density becomes larger than the energy necessary to form a dislocation is referred to as the critical thickness  $h_c$ . The formation of the dislocation plastically relaxes the stress in the layer and reduces the areal strain energy density.

A method to predict relaxation of a pseudomorphic layer was developed by Matthews and Blakeslee[56] and later on refined by Braun and coworkers[57] who showed that the critical thickness can be calculated numerically by the following transcendent formula.

$$h_c = b \frac{1 - \nu \cos^2(\alpha)}{8\pi|\epsilon_{||}|(1 + \nu) \sin(\alpha) \cos(\beta)} \ln\left(\frac{\rho h_c}{b}\right) \quad (4.9)$$

In here  $b$  is the absolute length of the Burgers vector  $\vec{b}$  of the dislocation,  $\alpha$  is the angle between the Burgers vector and the dislocation line vector,  $\beta$  is the angle between the glide plane and the interface and  $\rho$  is the strain energy of the dislocation vector.

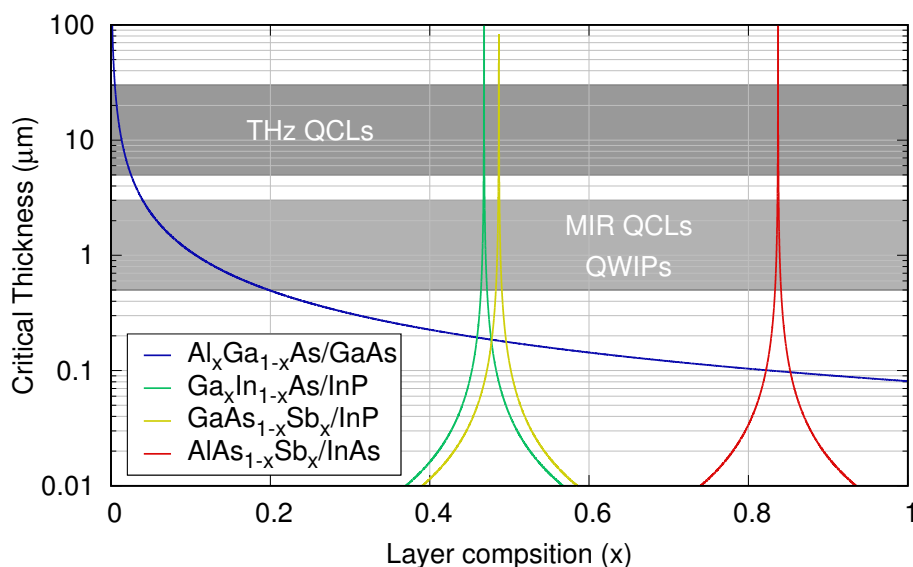


**Figure 4.2:** Critical thickness versus composition of different materials. The composition of the ternary alloys changes their lattice constant and hence, the lattice mismatch with the substrate. The two gray shaded areas indicate the typical thicknesses of hetero structures used for intersubband devices. Since the lattice mismatch between GaAs and AlAs is only 0.145 %, the critical thickness for  $\text{Al}_x\text{Ga}_{1-x}\text{As}$  on GaAs is relatively large also for large Al mole fractions. For the other ternaries, the composition has to be accurate to a few tenth of a percent to allow for the growth of intersubband devices.

If dislocations are introduced into an otherwise perfect crystal, two domains on either side of the dislocation will be formed which are in themselves perfectly crystalline but tilted or twisted with respect to each other. The size of this domains is related to the density of dislocations in the crystal and crystals exhibiting a high density of such domains are referred to as mosaic. It is clear that a high density of dislocations will reduce the smoothness of a layer since it will consist of many small regions with slightly different crystal orientations.

Figure 4.2 shows the influence of the composition of different ternary materials on the critical thickness. One can see that the critical thickness is strongly reduced if the composition of the material deviates from the ideal composition for lattice matching. Due to the small lattice mismatch between GaAs and AlAs relatively thick layers of  $\text{Al}_x\text{Ga}_{1-x}\text{As}$  can be grown even for large Al mole fractions. For other ternary materials such as  $\text{Ga}_x\text{In}_{1-x}\text{As}$ ,  $\text{GaAs}_{1-x}\text{Sb}_x$  and  $\text{AlAs}_{1-x}\text{Sb}_x$  the composition composition has to be accurate to a few tenth of a percent in order to prevent relaxation of thick structures.

## 4.2 Crystal growth by Molecular Beam Epitaxy

MBE is a technique to epitaxially grow thin films of semiconductors, metals or oxides on a substrate which acts as a template for the formation of a crystal. By choosing conditions which favor a well ordered positioning of these atoms or molecules, layers of high crystalline quality can be grown[58]. In the most simple case, the atoms or molecules, which are deposited on the substrate, are as those of which the substrate is built itself. The resulting layer is then indistinguishable from the substrate, and the process is referred to as “homoepitaxy”. However, also atoms of a different species can be deposited onto the substrate and, if the conditions are chosen correctly, will form a crystal. This case is referred to as “heteroepitaxy”. Since the substrate acts as a template for the formation of the crystal, the quality of the substrate has a strong influence on the quality of the grown layer. To ensure the best results, usually substrates in which all atoms are in the same crystal phase, so called single crystals, are used. The atoms or molecules deposited onto the substrate are evaporated from cells containing very high purity material. This is necessary to reduce the amount of contamination by electrically active defects.

Figure 4.3 shows the main parts of an MBE reactor. The whole process is carried out under Ultra High Vacuum (UHV) conditions inside a vacuum chamber (a), *i.e.* a background pressure of less than  $10^{-9}$  torr. In order to maintain UHV conditions, liquid-helium cryo pumps, ion getter pumps and titanium sublimation pumps are attached to the chamber (b). Inside the reactor, a hollow cryo shroud (also called cryo panel)(c), which is filled with liquid nitrogen acts as a cryo getter pump, and thermally insulates heat sources inside the chamber from each other to limit thermal cross talk. The substrate (d) is placed inside a holder (e) (also called platen or block), which is placed in front of a heater (f). During the growth process, the substrate is kept at an elevated temperature, and is rotated around the z axis (g) to enhance the uniformity across the substrate. The temperature of the substrate is monitored by a thermocouple which sits in the center of the heater. To get a more accurate measure of the temperature, usually a pyrometer is used to monitor the temperature through a window (h) from the outside. During growth, source material is evaporated from a cell, and condenses on the substrate. Shutters (i) in front of each cell are used to control which materials reach the substrate at any given point during the growth. For the growth of III/V semiconductors, there are basically two different types of cells. Standard effusion cells (j) are used to evaporate group III materials. These cells consist of a crucible, usually made out of Pyrolytic Boron Nitride (PBN), holding the source material, which is surrounded by a heater. The temperature of the source material controls the rate at which material is evaporated from the cell.



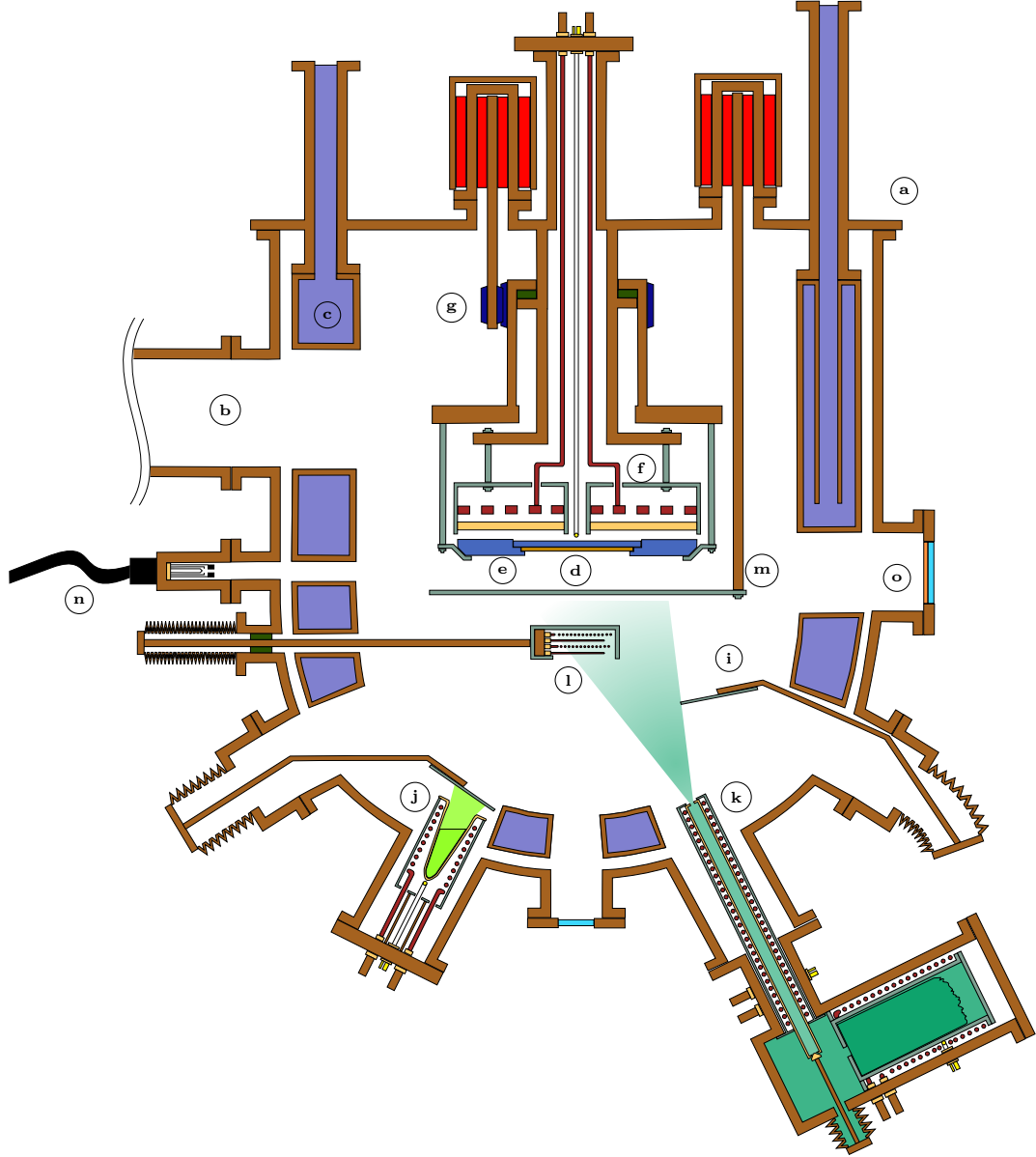


**Figure 4.3:** Schematic drawing of an MBE system and its components. (a) vacuum chamber, (b) pumping well, (c) cryo panel, (d) substrate, (e) substrate holder (platen), (f) substrate heater, (g) substrate rotation, (h) pyrometer window, (i) cell Shutter, (j) standard effusion cell, (k) valved cracking cell, (l) flux gauge, (m) main shutter, (n) RHEED gun, (o) RHEED screen

## 4.2. Crystal growth by Molecular Beam Epitaxy

---

Since group V materials sublime from the source as tetramers which are not as reactive as dimers or monomers, for these materials valved cracking cells are used[58, 59, 60](k). In this type of cell the evaporated materials passes through a valve which can be used to regulate the flux of this material, and then travels through a cracking zone, which consists of a PBN tube which is heated to up to 1200 °C in which the tetramers are cracked down to dimers or monomers, depending on the temperature.

To monitor the amount of materials coming from a cell, a flux gauge (l) can be brought into the beam path. It consists of a headed filament on which arriving atoms or molecules are ionized[61]. High tension between a grid and a collector is used to collect the ions and create a current which is proportional to the flux coming from the cell. During the flux measurement the substrate is protected from the flux by a main shutter (m).

To monitor the state of the surface of the growing crystal a Reflection High Energy Electron Diffraction (RHEED) setup is used. It consists of an electron gun (n) from which electron are shot at a shallow angle onto the substrate, the electrons are then diffracted by the substrate and an interference pattern is created on a phosphorus screen (o) which sits on the opposite side of the chamber.

Details on the MBE process will be given in the following sections.

### 4.2.1 Ultra high vacuum conditions

Assuming every atom impinging on the surface of the substrate creates an electrically active defect, and defects of opposite charge do not cancel out, the doping due to impurities from the background vapor is given by[62]

$$n = \sum_i s_i w_i r^{-1} \quad (4.10)$$

where  $r$  is the growth rate of layer being grown and  $s_i$  and  $w_i$  are the sticking coefficient and the impingement rate of atom or molecule species  $i$ , respectively.

How low the background pressure has to be to achieve the low background doping necessary for intersubband devices is shown by the following example.

For THz QCLs the intentional doping is on the order of  $1 \times 10^{15} \text{ cm}^{-3}$ . The background doping therefore should be at much lower than that. With the lattice constant of GaAs ( $a = 0.565325 \text{ nm}$ ) and eight atoms per unit cell we find that there are  $4.42 \times 10^{22} \text{ cm}^{-3}$  atoms in GaAs. To get background doping of  $1 \times 10^{15} \text{ cm}^{-3}$  the ratio between unintentional and intentional depositions has to be smaller than  $\frac{1}{4.42} \times 10^{-7}$ .

III/V semiconductors are typically grown at growth rates close to 1 Monolayer (ML) per second. For GaAs this means  $1.25159 \times 10^{19}$  atoms are deposited per unit area and second. With the relation above we get for the rate of atoms deposited from the background:

$$w_i < \frac{1.25128 \times 10^{19}}{4.42 \times 10^7} = 2.83166 \times 10^{11} m^{-3} s^{-1} \quad (4.11)$$

The rate of atom or molecules of species  $i$  from the background vapor impinging on the substrate per second and square meter is given by equation 4.12.

$$w_i = p_i \sqrt{\frac{N_A}{2\pi M_i k_B T}} \quad (4.12)$$

From this we get the background pressure as follows if we assume the temperature of the background vapor is 300 K.

$$p_i = 2.078843 \times 10^{-22} w_i \sqrt{M_i} \quad (4.13)$$

To get value for the background pressure we assume the background only consists of Nitrogen molecules. With the molar weight ( $28.02 \times 10^{-3} kg/mol$ ), and the limit for the deposition rate derived in equation 4.11 we get

$$\begin{aligned} p_i &< 2.078843 \times 10^{-22} 2.83166 \times 10^{11} \sqrt{M_i} \\ p_i &< 4.9278 \times 10^{-12} \text{ pa or } 3.696 \times 10^{-14} \text{ torr} \end{aligned} \quad (4.14)$$

With careful handling, such a low background pressure can be achieved in an MBE system. However, even lower background doping than  $1 \times 10^{15} cm^{-3}$  is usually observed in MBE grown structures. This is attributed to the fact that the sticking coefficient  $s_i$  is much less than 1 at the conditions at which growth takes place.

### 4.2.2 Evaporation of Source Materials

In order to grow a crystal in an MBE system, atom or molecules are evaporated from high purity source material. The evaporation of liquid or solid source material is described by the Hertz-Knudsen equation (4.15)[62].

$$\Gamma_e = \frac{dN_e}{dt} = A_e (p_{eq} - p_v) \sqrt{\frac{N_A}{2\pi M k_B T}} \quad (4.15)$$

Herein,  $\frac{dN_e}{dt}$  is the number of molecules leaving the source per unit time,  $A_e$  is the surface area of the evaporating material,  $p_v$  is the vacuum pressure of the volume into which the

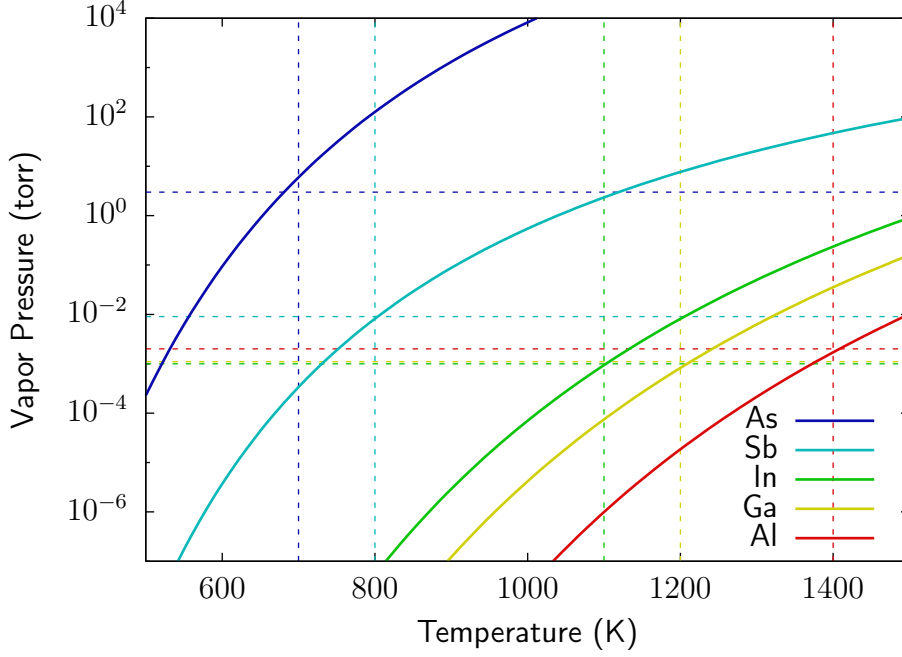


**Figure 4.4:** Vapor pressures of Al,Ga,In,As and Sb. The vertical dashed lines indicate typical evaporation temperatures during growth. The dashed horizontal lines show the respective vapor pressure at this temperature. Since the cells used in MBE are no Knudsen cells and due to the distance between cell and beam flux monitor, the measured flux in the MBE-system will be different. The slopes of the ideal vapor pressure curves, however, are usually similar to those we find in an MBE system[63].

material is evaporated, and  $p_{eq}$  is the equilibrium pressure of the vapor above the material at its current temperature. Under UHV conditions we can assume that  $p_v = 0$ . For a given material, the rate at which molecules are leaving the source therefore depends on the vapor pressure of the material  $p_{eq}$  and  $\sqrt{\frac{1}{T}}$ . Hence also the rate of molecules arriving at the substrate, *i.e.* the growth rate, is related to the temperature of the source material. The vapor pressures of materials used in III/V MBE can be seen in figure 4.4.

The relation given in equation 4.15 is strictly only true if the orifice through which the molecules escape into the vacuum is small compared to the evaporation surface and the equilibrium pressure is not disturbed. This is not true for the type of cells used in MBE since here the size of the evaporation surface is on the same order as the orifice. The linear dependence of the growth rate on the vapor pressure of the source material still can be considered a very good approximation.

The actual number of molecules arriving at the substrate of course also depends on the distance and angles between the cell and the substrate. Assuming an ideal Knudsen cell,

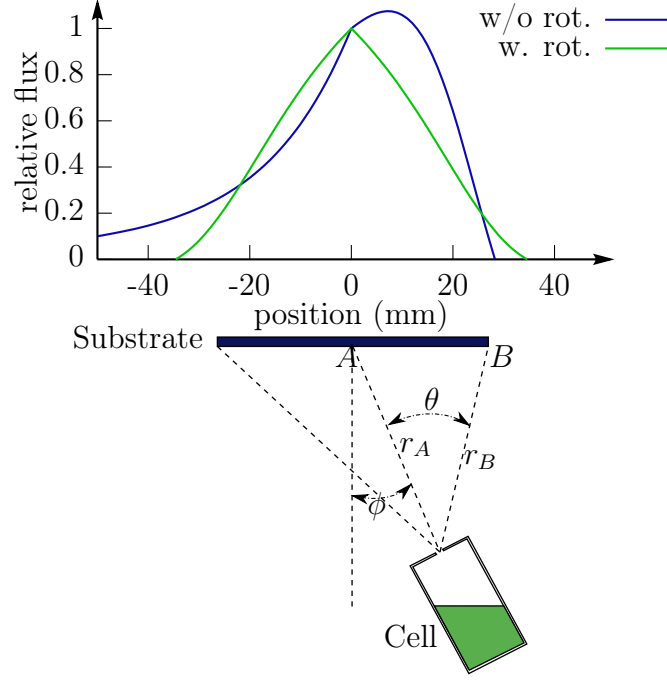


**Figure 4.5:** Evaporation characteristic of a Knudsen cell. The flux arriving at any point of the substrate depends on the distance of the cell  $r_A$ , its tilt from the surface normal  $\phi$  and the angle between the normal of the cell and the line of sight to the point  $\theta$ . If the substrate is at rest the distribution of the flux will be asymmetric with its maximum shifted towards the position of the cell. This asymmetry can be countered by rotating the substrate around the  $z$  axis. Conical evaporation cells, as they are used in MBE-systems show a much more uniform distribution of the flux and provide better homogeneity than Knudsen cells.

shown in figure 4.5, the flux  $I_A$  arriving at point A is given by

$$I_A = \frac{\Gamma_e}{\pi r_A^2} \cos \phi, \quad (4.16)$$

where  $\Gamma_e$  is the rate of molecules evaporating from the cell,  $r_A$  is the distance between the cell and point A on the substrate and  $\phi$  is the incidence angle of the beam with respect to the substrate normal. The flux at point B is given by

$$I_B = \frac{\Gamma_e}{\pi r_B^2} \cos \theta \cos (\theta + \phi). \quad (4.17)$$

Figure 4.5 shows the relative deposition rate, or flux, at different positions of the substrate. It can be seen that a ideal Knudsen cell leads to a very inhomogeneous flux distributions across the substrate. By rotating the substrate around the  $Z$  axis, a symmetric

### 4.3. Reactions during MBE Growth

---

distribution can be achieved. In practice, however, cell types are used which create more homogeneous distribution, at the expense of a less efficient use of the source material.

The two types of cells, mainly used for the growth of III/V semiconductors are shown in figure 4.3. Figure 4.3 (j) shows a conical cell which is used for group III materials. It consists of conical crucible, commonly made from PBN, which holds the material. It is surrounded by a heater which supplies the heat necessary to achieve the temperatures for evaporation. The temperature is measured by a thermocouple. Figure 4.3 (k) shows a cracking cell. This type of cell is used for group V materials. In this type of cell the source materials resides inside a compartment which is separated from the vacuum chamber by a valve which is used to control the amount of material which leaves the cell. At the evaporation temperature, group V materials sublime as tetramers. Before the vapor enters the deposition chamber it travels through a heated PBN tube. On contact with this tube the group V tetramers can be cracked down to dimers or monomers, depending on the temperature of the cracking zone. The type of group V molecules used for the growth of a layer can strongly influence the growth mode and hence the quality of the grown layer.

## 4.3 Reactions during MBE Growth

When a beam of atoms or molecules is incident upon a crystal surface they can adsorb and interact with the crystal[62]. As shown in figure 4.6 the adsorbed atom or molecule will migrate on the surface until it either encounters a lattice site at which it will be incorporated into the crystal, aggregate with other adatoms on the surface and nucleate a new island or desorb thermally, thus leaving the surface. The time adsorbed atoms or molecules can remain on the surface before they are integrated into the crystal can be on the order of milliseconds and during that time they can perform  $\sim 10^6$  hops to different sites[64].

The rates of all three processes strongly depend on the species of the atoms or molecules in the beam, crystal substrate as well as the crystal plane(s) of the surface, and its condition, e.g. its temperature, and have a large influence on the structure and morphology of the growing crystal.

With respect to the morphology of the growing crystal, three modes of crystal growth, shown in figure 4.7, can be identified. In the Volmer-Weber growth mode, the interaction between adatoms is much stronger than the interaction between the adatoms and the crystal surface. Consequently the growth will exhibit a high rate of island nucleation which leads a three dimensional structure of the film.

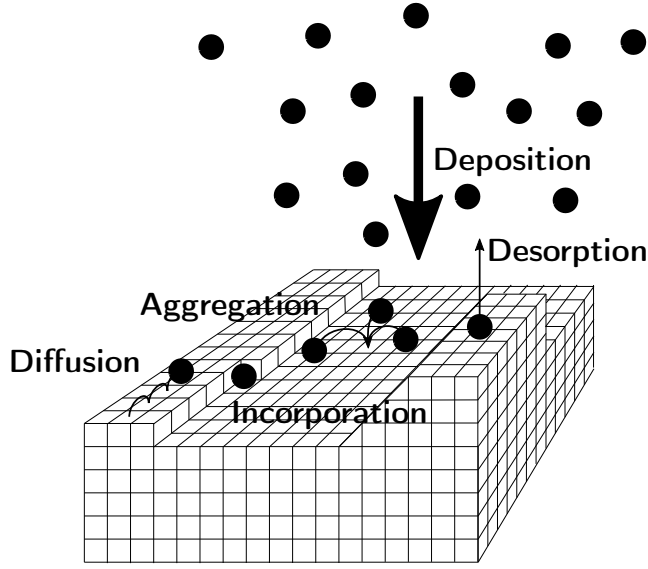


**Figure 4.6:** Actions of atoms or molecules impinging onto a crystal surface. Atoms or molecules on a crystal surface will be diffuse on the surface until they aggregate, incorporate or desorbe. After [62].

In the Frank-van-der-Merwe growth mode, adatom-adatom interactions are comparably weak with respect to interactions with the crystal surface, and the adatoms preferentially occupy vacant crystal sites of already existing layers. This mode, which leads to atomically smooth growth surfaces, is the preferential growth mode for III-V semiconductor heterostructures.

There exists a growth mode which exhibits a mix of the morphological characteristics of the two aforementioned modes which is referred to as Stranski-Krastanov growth mode. In this mode island nucleation starts after the growth of a few monolayers in the layer by layer growth mode.

### 4.3.1 Surface Reconstructions

Atoms on a crystal surface will usually show a different arrangement than those atoms within the crystal since they have less partners for bonding. The atoms form periodic structures on the surface, which are denoted by the crystal surface on which they form as

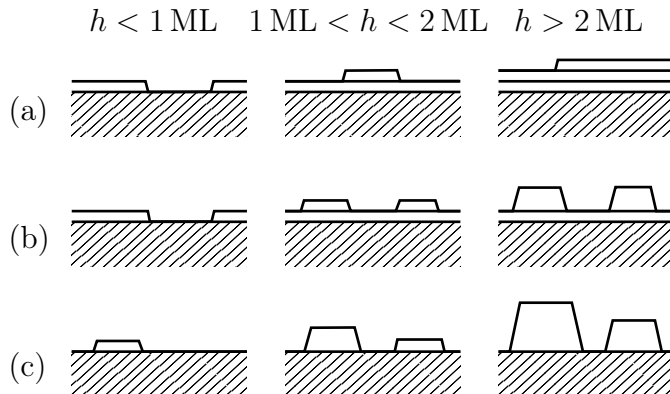


**Figure 4.7:** Epitaxial growth modes. Depending on the conditions the morphology of the growing layer can be dominated by layer by layer growth (Frank-van der Merwe), island growth (Volmer-Weber) or a mixed growth mode (Stranski-Krastanov). After [62].

#### 4.3. Reactions during MBE Growth

well as their periodicity and rotation. Figure 4.8 shows the GaAs(100)-(4×4) reconstruction, measured by Biegelsen et. al.[65] by Scanning Tunneling Microscopy (STM), which formed when the sample was cooled to 300 °C under As flux.

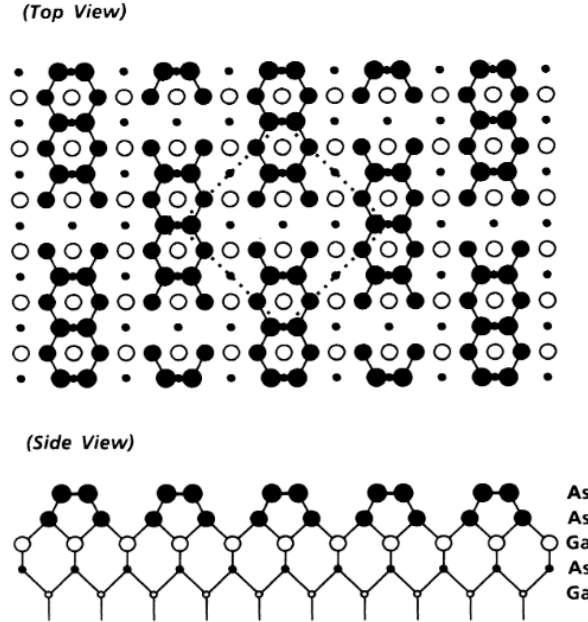


**Figure 4.8:** GaAs(100)-(4×4) reconstruction. Taken from [65]

The As atoms on the surface arrange in rows along the [011] directions and the structure shows a period which is four times larger than that of the underlying crystal surface in both the [010] and [001] directions. The unit cell of the reconstruction is indicated by the dotted square in the center of figure 4.8. Surface reconstructions can be measured in-situ by RHEED which is briefly explained in section 5.2.

Many other reconstructions of the GaAs(100) surface can be found, however, in terms of MBE growth the most important ones are the Ga-stabilized GaAs(100)-(4×2) and the As-stabilized GaAs(100)-(2×4) reconstructions which are found at elevated substrate temperatures depending on the supplied As pressure.

When a (100) oriented GaAs substrate is heated without supplying flux of As, As atoms will leave the surface and the (4×4) reconstruction will change to a (2×4) reconstruction. Upon further heating the rate of As leaving the surface will increase up until the point where the reconstruction changes and the Ga-stabilized (4×2) reconstruction will appear. If the rate of loss of As atoms is compensated for by supplying As flux, the reconstruction will change back to the As stabilized (2×4) reconstruction. If under these conditions flux of Ga is supplied, the reconstruction will change back to the Ga-stabilized (4×2) since Ga will stick to the surface and the supplied As flux is just enough to compensate for the loss of As but not enough to form GaAs. Hence, for the growth of GaAs, Ga and As



atoms have to be supplied at least at a one-to-one ratio. Since the sticking coefficient of As is close to zero in absence of free Ga adatoms on the surface, perfect stoichiometry in GaAs is easily achieved if As flux is provided in excess. We see that the reconstruction, found on the surface of a growing layer give a good indication of the current condition of the surface and allows for the in-situ monitoring of the growth process.

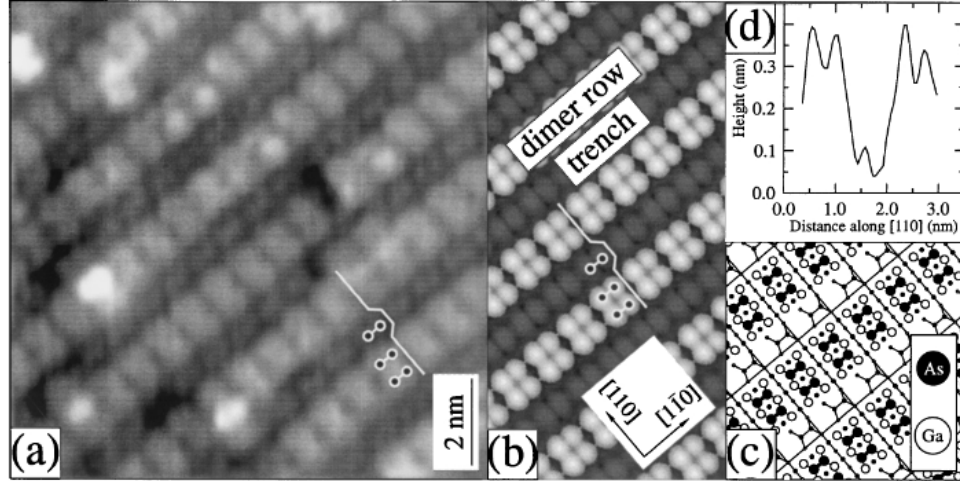


**Figure 4.9:** The GaAs(100)-(2×4) reconstruction. Taken from [66]



---

## Characterization of Epitaxial Layer Structures

---

### 5.1 High Resolution X-Ray Diffraction

X-ray diffraction is a standard tool to characterize the structure of crystals. To do so, an, ideally monochromatic, beam of X-Rays is directed onto a crystalline substance. X-ray beams, which are diffracted from this crystalline substance are measured and the angle at which they appear provides information about its crystal structure.

This interaction between X-rays and crystals was first analyzed by Max von Laue in 1912[67]. He realized that electromagnetic waves, such as X-rays, will be diffracted by a periodic arrangement of atoms. W.H. Bragg and W.L. Bragg later refined the method and postulated the conditions for which diffraction will occur[68, 69].

#### 5.1.1 Diffraction of X-Rays from Crystal Planes

If we want to examine semiconductor crystals, the wavelength of the radiation we use has to be on the same order of magnitude as the lattice constant of the crystal. Many metals exhibit characteristic X-Ray lines at wavelengths that can be used for that purpose[70]. For the analysis of III/V semiconductor crystals, most commonly the  $K\alpha_1$  line of copper, which appears at a wavelength of 0.154 18 nm is used. Figure 5.1 shows the typical configuration of single crystal diffraction experiment. This configuration is usually referred to as HRXRD setup. X-Rays are emitted from a source and directed onto a (single) crystalline sample, which is mounted on a sample holder, under the angle  $\omega_+$  with respect

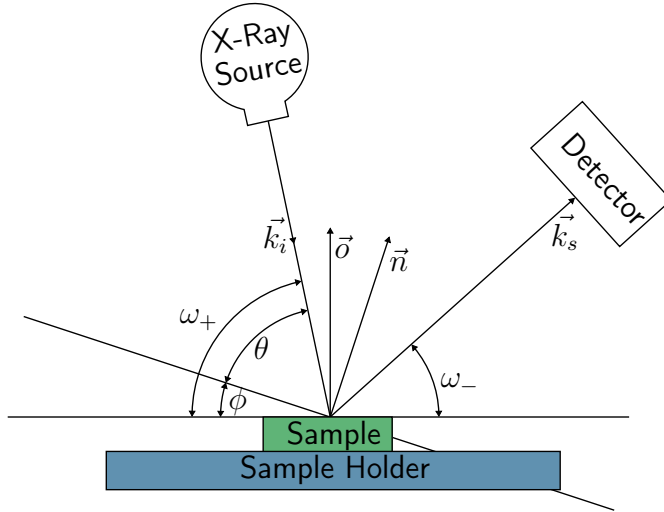


**Figure 5.1:** HRXRD Setup. X-Rays are emitted from the source and directed onto the crystal under the angle  $\omega_+$ . The diffracted rays exit the crystal under the angle  $\omega_-$  and reach the detector.  $\phi$  is the tilt angle of the crystal planes under examination with respect to the surface, i.e. the tilt angle between the surface normal  $\vec{o}$  and the normal to the crystal planes under examination  $\vec{n}$ . The angle  $\theta$  is the incidence angle with respect to this planes.

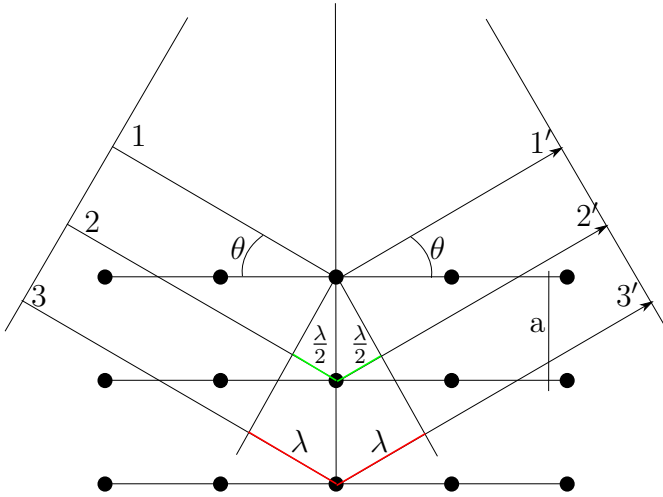


**Figure 5.2:** X-Rays scattered by a crystal. The rays 1, 2 and 3 are incident to the crystal surface under the angle  $\theta$ . The scattered rays 1', 2' and 3' exit the crystal under the same angle. If the path difference between two rays is equal to the wavelength of the rays they will interfere constructively at the detector.

to the crystal surface. They are scattered from the crystal under the angle  $\omega_-$  and reach the detector. The crystal planes under examination are tilted with respect to the surface by an angle  $\phi$  and the angle  $\theta$  is the incidence angle of the X-Rays with respect to that particular set of crystal planes.

Figure 5.2 shows how X-Rays, which are directed onto a crystal surface, will be scattered by the atoms of which the crystal is formed[71]. If we assume a plane wave of monochromatic X-Rays (of a wavelength  $\lambda$ ) which is incident to a crystal surface under the angle  $\theta$  they will be scattered by the atoms within that plane under the same angle. Rays which are scattered by the next row of atoms will have to travel a slightly longer distance depending on the spacing between the rows and the angle  $\theta$ . The path difference

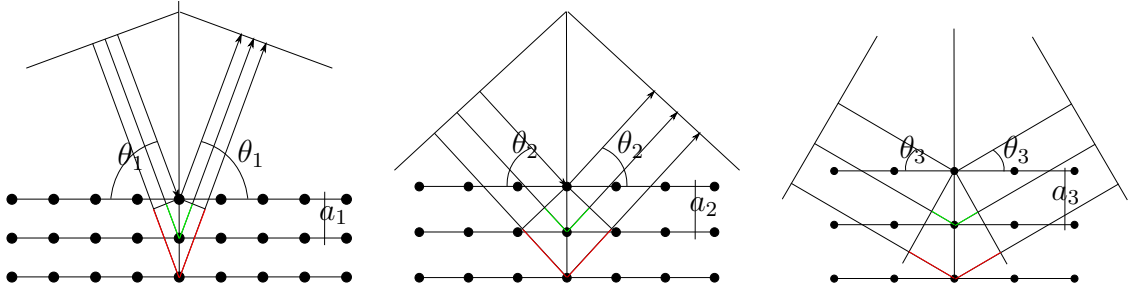


**Figure 5.3:** Symmetric scans of crystals with different lattice constants  $a$ . The Bragg angle  $\theta$  for which the Bragg condition is fulfilled depends on the spacing of the atom rows. For larger spacing constructive interference is found at smaller angles of  $\theta$ .

between the rays is given by

$$\begin{aligned}\Delta x_{12} &= 2a \sin(\theta) \\ \Delta x_{13} &= 4a \sin(\theta) = 2\Delta x_{12} \\ \Delta x_{23} &= 2a \sin(\theta) = \Delta x_{12}.\end{aligned}\tag{5.1}$$

If this path difference  $\Delta x_{12}$  of rays 1 and 2 is equal to  $\lambda$ , the two rays will interfere constructively. We can also see that in this case the path difference of the rays scattered by any two rows of atoms is a multiple of  $\lambda$  and hence they enforce the signal collected at the detector. The angle at which all rays interfere constructively is given by

$$n\lambda = 2a \sin(\theta)\tag{5.2}$$

which is known as Bragg's law. The angle  $\theta$  for which the condition is fulfilled is called the Bragg angle. This angle depends on the spacing of the atomic planes, or the lattice constant of the crystal. Figure 5.3 illustrates how the Bragg angle depends on the spacing of atom rows. It can be seen that for a given X-Ray wavelength, a larger spacing results in a smaller the Bragg angle  $\theta$ . Hence, the lattice constant can be measured by finding the Bragg angle and for a given wavelength.

Since the Bragg condition is also fulfilled if the path difference  $\Delta x_{12}$  is a multiple of the wavelength  $\lambda$ , constructive interference can also be found at larger angles  $\theta$ . Figure 5.4 shows the angle at which the second order diffraction peak is found. The path difference for rays scattered from the first row of atoms and the second row of atoms is exactly  $\Delta x = 2\lambda$ . The situation is the same as if there was a virtual row of atoms at  $\frac{a}{2}$  which would result in a path difference of  $\Delta x = \lambda$  for the scattered rays. This interpretation of this phenomenon lead to the use of the miller indices as described in section 2.3.

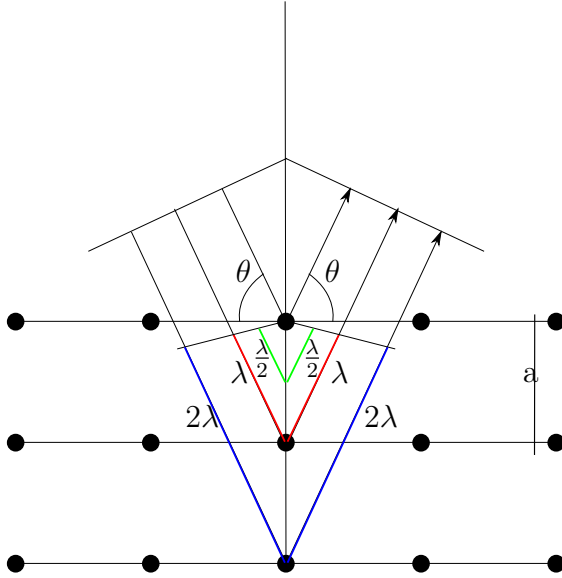


**Figure 5.4:** Second order diffraction. The second order diffraction appears at an angle where the path difference for rays scattered from the first and the second row of atoms is equal to  $2\lambda$ . The situation is the same as if there was a virtual row of atoms at  $\frac{a}{2}$ . If the crystal is oriented such that its surface is parallel to the  $(0\ 0\ 1)$  planes, this diffraction peak would be denoted the  $(0\ 0\ 2)$  diffraction.

The angle  $\theta$  at which the diffraction from a particular set of parallel planes in the lattice is found can be calculated from

$$\theta = \arcsin\left(\frac{\lambda}{2d_{hkl}}\right) \quad (5.3)$$

where  $d_{hkl}$  is given by the relation

$$\left(\frac{1}{d_{hkl}}\right)^2 = \left(\frac{h}{a}\right)^2 + \left(\frac{k}{b}\right)^2 + \left(\frac{l}{c}\right)^2 \quad (5.4)$$

where  $a, b$  and  $c$  are the lattice constants in an orthorhombic crystal and  $h, k$  and  $l$  are the miller indices of the planes.

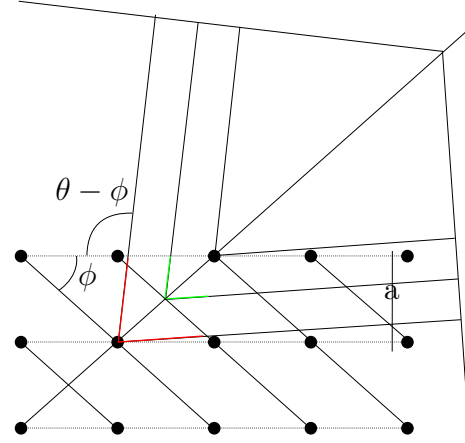
Diffraction is of course not limited to rows of atoms which are parallel to the crystal surface. Figure 5.5 shows the angle for an asymmetric scan. We see that for this type of scan, not only the out-of-plane lattice constant  $a_{\perp}$  but also the in-plane lattice constant  $a_{\parallel}$  influences the angles  $\theta$  and  $\phi$  at which the diffraction peak will appear, hence, performing asymmetric measurements is important in order to identify the structure of crystals which do not have a cubic base.

The tilt angle of a set of planes with respect to the crystal surface is given by

$$\phi = \arccos\left(\frac{\vec{S} \cdot \vec{A}}{\|\vec{S}\| \|\vec{A}\|}\right), \quad (5.5)$$

where  $\vec{S}$  is the surface normal and  $\vec{A}$  is the vector normal to the planes under examination, given by the miller indices of the plane.

**Figure 5.5:** Asymmetric HRXRD scan. The crystal is oriented such that its surface is parallel to the (0 0 1) planes. For the symmetric scan the incidence angle with respect to the sample surface is the same as the exit angle. In the asymmetric case the incidence angle with respect to the sample surface ( $\omega_+$ ) differs from the incidence angle with respect to the planes under examination ( $\theta$ ).



A measurement performed over  $\theta$  and  $\phi$  is called reciprocal space map. Such a map is shown in figure 5.6. A reciprocal space map is usually presented in terms of reciprocal lattice units which are calculated by

$$q_{\perp} = \frac{2}{\lambda} \sin(\theta) \cos(\phi) \quad (5.6)$$

$$q_{\parallel} = \frac{2}{\lambda} \sin(\theta) \sin(\phi). \quad (5.7)$$

As we have seen before, higher diffraction orders can be found at larger angles  $\theta$ . Since  $\theta$  cannot be larger than  $\frac{\pi}{2}$ , not all diffraction orders can be measured. The upper boundary in figure 5.6 is defined by this condition. The two half circles in the lower part of the figure are due to the fact that in an HRXRD setup the sample cannot be measured from behind the sample holder. All diffraction orders between these boundaries are accessible to examination in an HRXRD setup, although not all of them necessarily exist or provide valuable information.

### 5.1.2 HRXRD of hetero epitaxial layers

As we have seen in chapter MBE, it is possible to grow layers of different III/V materials on top of each other. If these materials have different lattice constants, they will show diffraction peaks at different Bragg angles, and hence, they can be distinguished in HRXRD. Figure 5.7 shows a symmetric scan around the GaAs (004) diffraction. The peak on the right side is due to a 400 nm thick layer of  $\text{Al}_{0.4}\text{Ga}_{0.6}\text{As}$  which has a larger native lattice constant  $a_0^L$  than the substrate. The oscillations around this peak are called Pendellösung fringes and appear due to the finite thickness of the layer. Moreover the presence of these fringes indicate high crystal quality since they only appear for samples with a low dislocation density.

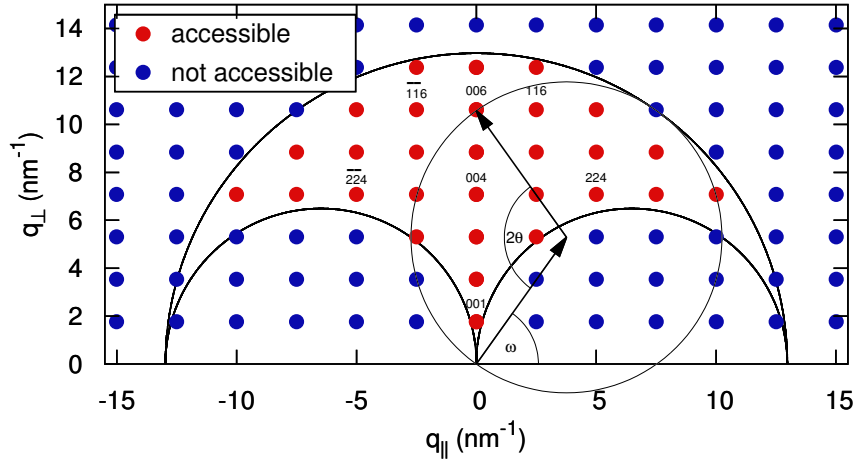


**Figure 5.6:** Diffraction orders of a simple cubic crystal in reciprocal space. The position of the peak gives the in-plane ( $q_{\parallel}$ ) and out of-plane ( $q_{\perp}$ ) reciprocal space coordinates from which the in-plane and out-of-plane lattice constants of the crystal can be calculated. The upper boundary is given by the size of the Ewald sphere, which depends on the used X-Ray wavelength. The lower boundary is given by the fact that the X-Rays cannot be incident to or leave the sample at an angle  $\omega$  of less than  $0^\circ$ .

As we have seen in figure 2.7, the lattice constant of ternary and quaternary materials depends on the composition of the materials. Hence, measuring the lattice constant can provide information on the composition of a layer.

Since the thickness of this layer is below the critical thickness for relaxation of this material, the layer is 100 % strained. This means its in-plane lattice constant ( $a_{\parallel}^L$ ) is equal to the lattice constant of the substrate  $a^s$  and smaller than the native lattice constant  $a_0^L$  of the layer material. Its out-of-plane lattice constant ( $a_{\perp}^L$ ) is larger than its native

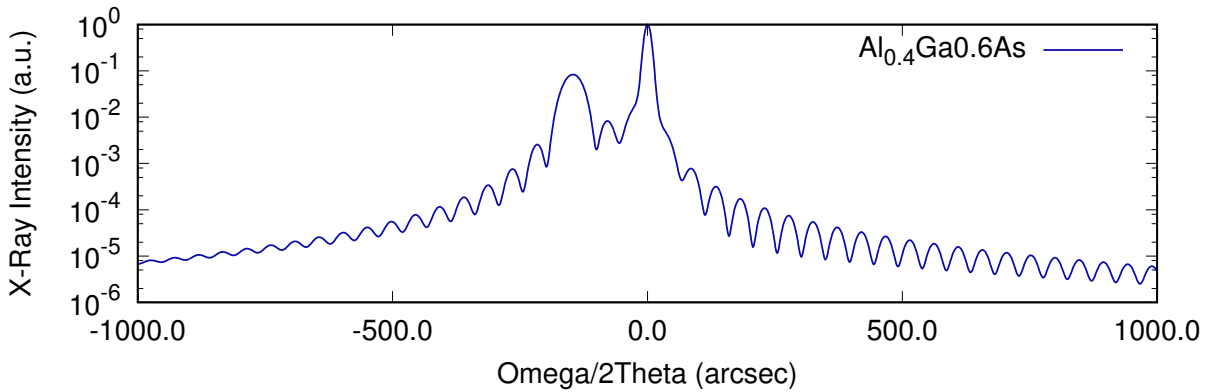


**Figure 5.7:** Symmetric  $\omega 2\theta$  scan around the GaAs (004) diffraction peak. The peak on the left of the substrate is due to a 400 nm thick  $\text{Al}_x\text{Ga}_{1-x}\text{As}_{0.4}$  layer.



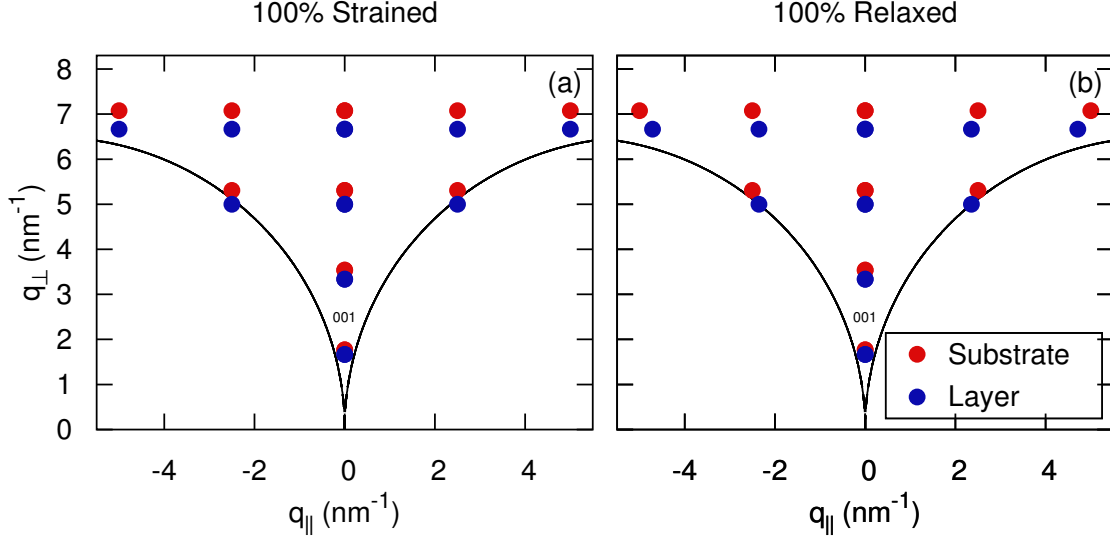


**Figure 5.8:** Comparison of a 100 % strained (a) and a 100 % relaxed (b) layer. The strained layer has the same in-plane lattice constants as the substrate. Hence, also its in-plane reciprocal space coordinate is the same. Its out-of-plane lattice constant, however, is different and its diffraction peaks are shifted vertically with respect to the substrate. For the relaxed layers the diffraction orders are shifted both vertically and horizontally with respect to the substrate since both, its in-plane and its out-of-plane lattice constant differ from that of the substrate.

lattice constant. This difference between the in-plane and the out-of-plane lattice constant can be measured by asymmetric scans. Figure 5.8 shows a comparison between a 100 % strained (a) and a 100 % relaxed (b) layer. Since the relaxed layer has a cubic crystal structure ( $a_{\parallel}^L = a_{\perp}^L$ ) both its in-plane and out-of-plane reciprocal space coordinates differ from that of the substrate. Since the in-plane lattice constant of the strained layer is equal to that of the substrate, also their in-plane reciprocal space coordinates are the same and the diffraction orders of the layer are shifted only vertically with respect to those of the substrate.

If the thickness of the layer is above the critical thickness it will start to relax. Depending on the degree of relaxation, the diffraction peak of the layer will appear anywhere between the two extremes shown in figure 5.8.

The degree of relaxation can be calculated from

$$r = \frac{a_{\parallel} - a^S}{a_{\parallel}^L - a^S}. \quad (5.8)$$

To measure the composition of a (partially) strained layer, we have to calculate the native

lattice constant of the layer ( $a_0^L$ ) which is given by

$$a_0^L = \frac{C_{11}}{C_{11} + 2C_{12}}(a_{\perp}^L - a_{\parallel}^L) + a_{\parallel}^L, \quad (5.9)$$

where  $C_{ij}$  are the stiffness coefficients of the layer material. From the position of the peak, the in-plane and out-of-plane lattice constants can be calculated, and using Vegards law the composition can be found. Due to the process of relaxation the atoms in the layer are not as well ordered to the substrate. This increases the roughness of the sample and leads to broadening of the peak and vanishing of the Pendelösung fringes.

## 5.2 Reflection High Energy Electron Diffraction

For the in-situ monitoring of the growth conditions, MBE-systems are equipped with a RHEED system[72]. RHEED uses high energy electrons to examine the structure of the surface of a sample. A beam of high energy electrons is incident onto the crystal surface at a shallow angle, typically  $\sim 2^\circ$ . It is diffracted by the crystal surface and thereafter incident to a phosphorus screen. Due to the shallow angle the penetration depth of the electron beam is only a few monolayers, and the diffraction pattern created on the phosphorus screen is mainly defined by the structure of the crystal surface, which acts as a diffraction grating for the electron beam.

The condition for diffraction on a one-dimensional grating is given by

$$a(\cos(\theta_{in}) - \cos(\theta_{out})) = n\lambda, \quad (5.10)$$

where  $a$  is the grating period,  $\theta_{in}$  and  $\theta_{out}$  are the angles of the incident and the diffracted wave respectively,  $n$  is the diffraction order and  $\lambda$  is the electron wavelength.

The de Broglie wavelength of the incident electrons for an acceleration voltage  $V$  is given by

$$\lambda = \frac{h}{\sqrt{2m_e E}} \approx \frac{1.2286 \times 10^{-9}}{\sqrt{V}} \quad (5.11)$$

where  $h$  is the Planck constant,  $m_e$  is the electron mass and  $E$  is the kinetic energy of the electron. For an acceleration voltage of 10 kV this results in an electron wavelength of  $1.2286 \times 10^{-2}$  nm.

By applying the wavenumber of the electrons  $|\vec{k}| = \frac{2\pi}{\lambda}$  we find

$$k(\cos(\theta_{in}) - \cos(\theta_{out})) = m \frac{2\pi}{a}. \quad (5.12)$$

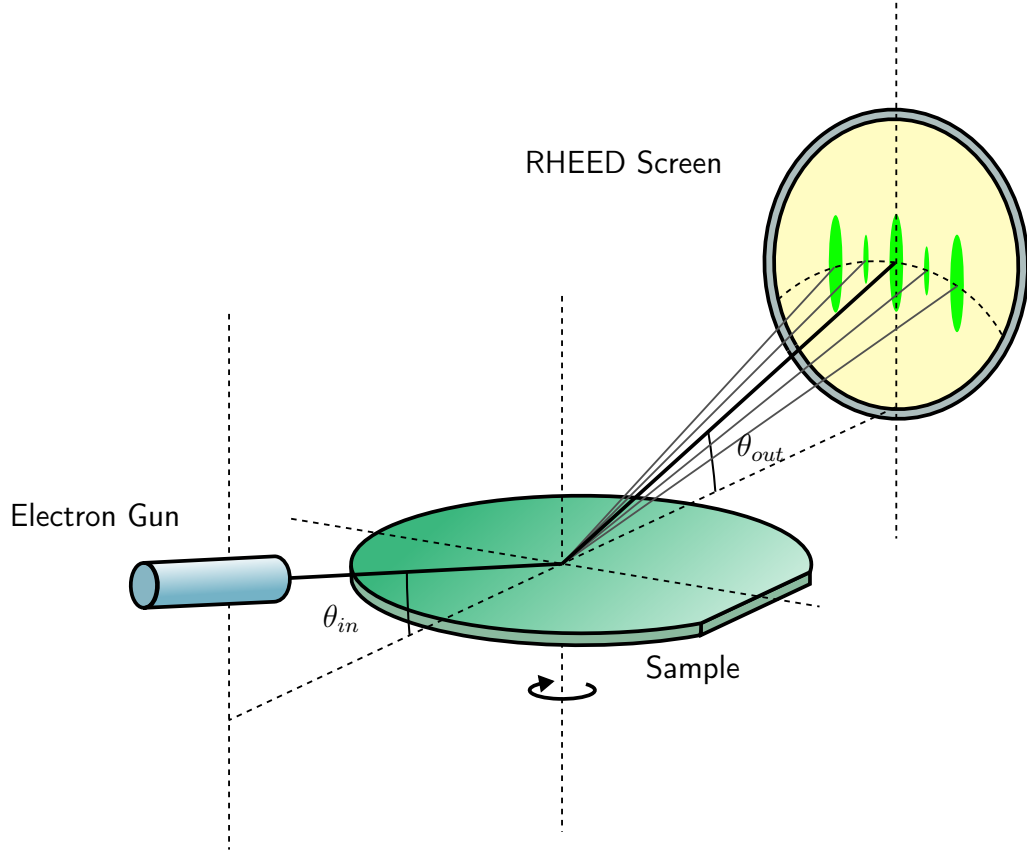


**Figure 5.9:** Components of a RHEED setup. A beam of electrons is emitted from an electron gun and is incident to the sample surface at a very shallow angle of  $\sim 2^\circ$ . On the surface the beam is diffracted and the electrons are incident onto a phosphorus screen (RHEED screen). The image created on the screen depends on the condition of the crystal surface. If the sample can be rotated, information about the surface with respect to different crystal orientations can be gathered.

This can also be written in terms of the wave vectors of the incident and the diffracted electrons as follows

$$\frac{\vec{a}^T}{|\vec{a}|} \cdot (\vec{k}_{in} - \vec{k}_{out}) = n \frac{2\pi}{a}. \quad (5.13)$$

If we introduce a vector  $\vec{a}'$  such that

$$\vec{a}' \cdot \vec{a}^T = 2\pi, \quad (5.14)$$

we find

$$\vec{k}_{in} - \vec{k}_{out} = n\vec{a}'. \quad (5.15)$$

Equation 5.14 defines  $\vec{a}'$  as the set of all vectors that connect the points of two parallel planes which are separated by  $\frac{2\pi}{|\vec{a}|}$ . Hence, the diffraction condition (Equation 5.15) is fulfilled for any two vectors  $\vec{k}_{in}, \vec{k}_{out}$  which connect  $n$  parallel planes.

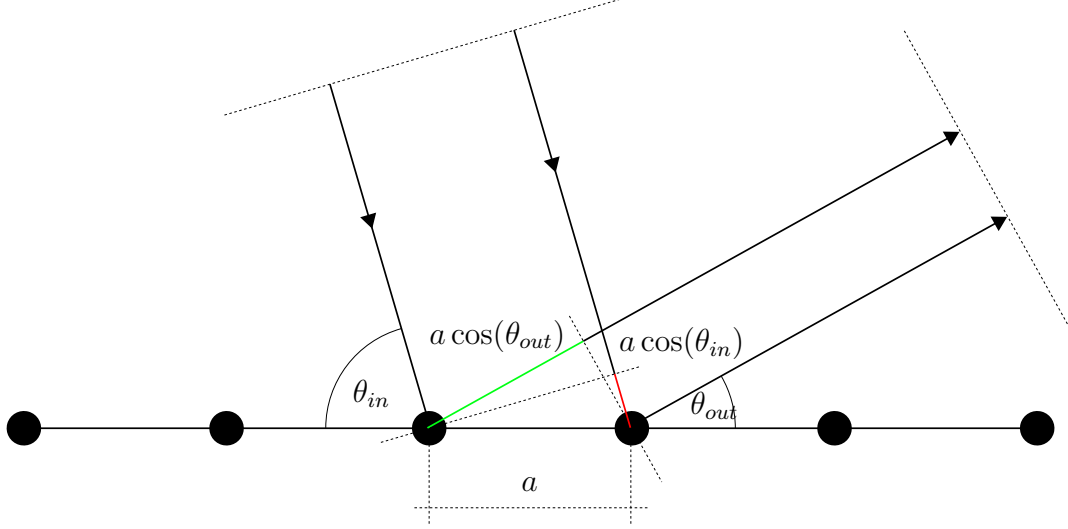


**Figure 5.10:** Diffraction from a one-dimensional row of atoms with a spacing of  $a$ . Electrons are incident to the row of atoms under the angle  $\theta_{in}$ . They are scattered by the atoms and exit under the angle  $\theta_{out}$ . The difference of the of the two beam paths is given by  $a \cos(\theta_{in}) - a \cos(\theta_{out})$ . After [72].

These parallel planes are the reciprocal lattice of the one-dimensional row of atoms and are defined by its reciprocal lattice vector  $\vec{a}^*$  which describes their spacing. If we assume that no momentum is transferred when the electrons are scattered then

$$|\vec{k}_{in}| = |\vec{k}_{out}| = k \quad (5.16)$$

is required, and all vectors which fulfill the diffraction condition are given by the intersections of the parallel planes of the reciprocal lattice and a sphere of radius  $k$  which is referred to as Ewald's sphere.

For simplicity, condition 5.15 can be rewritten as

$$\vec{S}_{\parallel} = n\vec{a}^*, \quad (5.17)$$

where  $\vec{S}_{\parallel}$  is the difference of the  $\vec{k}_{in}$  and  $\vec{k}_{out}$  parallel to  $\vec{a}^*$ .

Following the explanation above, the two dimensional lattice of a crystal surface is constructed by the vectors  $a_1$  and  $a_2$  by the linear combination

$$\vec{R} = n_1\vec{a}_1 + n_2\vec{a}_2. \quad (5.18)$$

Its corresponding reciprocal lattice

$$\vec{B}_m = m_1\vec{a}_1^* + m_2\vec{a}_2^*. \quad (5.19)$$

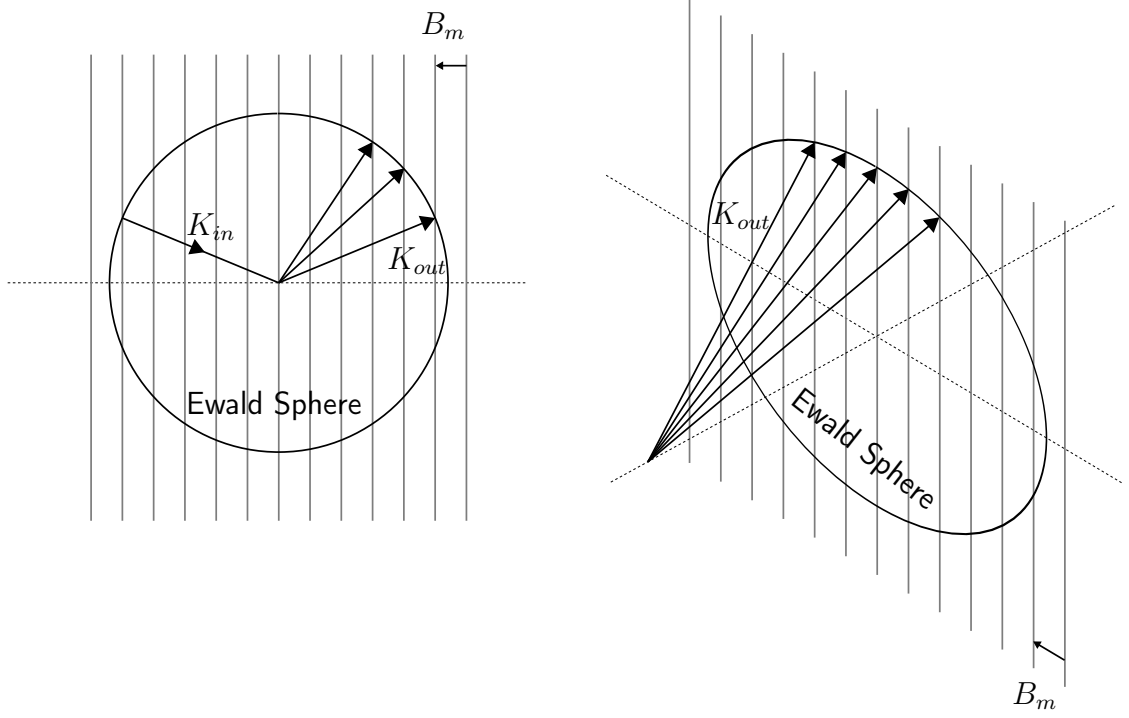


**Figure 5.11:** Diffraction in terms of the Ewald construction. The condition for diffraction is fulfilled at the intersections between the reciprocal lattice and the Ewald sphere which has the radius  $|k_{in}| = |k_{out}| = |k| = \frac{2\pi}{\lambda}$ . For diffraction from the two dimensional square lattice of the surface of a crystal the reciprocal lattice is composed of reciprocal lattice rods that are displaced by  $\vec{B}_m$ .

is defined by the two reciprocal lattice vectors

$$\begin{aligned} \vec{a}_1^* &= 2\pi \frac{a_2 \times \vec{z}}{a_1 \cdot (a_2 \times \vec{z})} \\ \vec{a}_2^* &= 2\pi \frac{a_1 \times \vec{z}}{a_2 \cdot (a_1 \times \vec{z})}. \end{aligned} \quad (5.20)$$

Due to the two dimensional nature of the crystal surface, its reciprocal lattice is composed of reciprocal lattice rods which are oriented perpendicular to the sample surface. For a square lattice ( $a_1 = a_2 = a$ ) the spacing of the rods is given by  $\frac{2\pi}{a}$ . Also in this case the Bragg condition is fulfilled at the intersections of the Ewald's sphere and the reciprocal lattice rods. Due to lattice vibrations of the crystal surface, the reciprocal lattice rods are of finite thickness. Moreover, the electron beam is not perfectly monochromatic which leads to finite width of the Ewald's sphere. Both these factors lead to the deviation of the diffraction image from an ideal point pattern into elongated ellipses. If the crystal surface is reconstructed, i.e. a two dimensional structure with a larger period then the lattice constant is present on the surface (see section 4.3.1), a diffraction image attributable to this reconstruction will be superimposed on the image created by the host crystal.

Since an  $(m \times n)$  reconstruction shows two spatial periods which are  $m$  and  $n$  times larger than the lattice constant of the host crystal, the period in the diffraction image will show an  $m$  or  $n$  times smaller period. Hence, RHEED can be used to identify the reconstructions of the crystal surface and helps to control the growth parameters.

As we have seen in chapter 4.3, epitaxial growth may not always occur in a layer-by-layer mode but may lead to the formation of three-dimensional structures. In such a case the diffraction scheme will change from the ideal reflection-diffraction scheme to a transmission-diffraction scheme. Hence, the reciprocal lattice will no longer consist of reciprocal lattice rods, but the three dimensional structure of the crystal leads to a reciprocal point lattice and the diffraction image will change from showing streaky features to showing spotty features. Monitoring the transition between these two mode can help to optimize the growth parameters.

## 5.3 Atomic Force Microscopy

MBE is capable of producing thin films of III/V semiconductors which show roughness values on the order of 0.2 nm. Interfaces showing such low roughness values are essential for applications which requires layer thicknesses of only a few nm. However, the morphology of such films is strongly dependent on the conditions under which they are grown. As described in chapter 4, choosing the wrong III/V ratio or substrate temperatures can lead to a 3-D growth mode which dramatically increases the roughness of the grown film. Moreover, roughening of the films can be found as a result of strain relaxation in highly lattice mismatched layers.

Atomic Force Microscopy (AFM) is a method to characterize the roughness of thin films[73]. It provides fast and reliable information about the quality of the film and can help to improve the growth parameters.

Figure 5.12 shows the basic principle of an AFM. An atomically sharp measurement tip, which is located at the end of a spring loaded cantilever is brought into contact with the sample surface. The cantilever is deformed due to the interaction between the tip and the sample surface. When the tip is moved towards the sample surface it will experience an attractive force at a few tens of nanometers due to van-deer-Waals interactions. At even smaller distances, the tip will experience a repulsive force due to short range coulomb interactions. The deformation of the cantilever is measured via a laser which is reflected off the backside of the cantilever onto a four-quadrant photo diode.

For the characterization of III/V thin films, contact mode and tapping mode are the most important modes of operation of an AFM[74]. In contact mode, the tip is brought

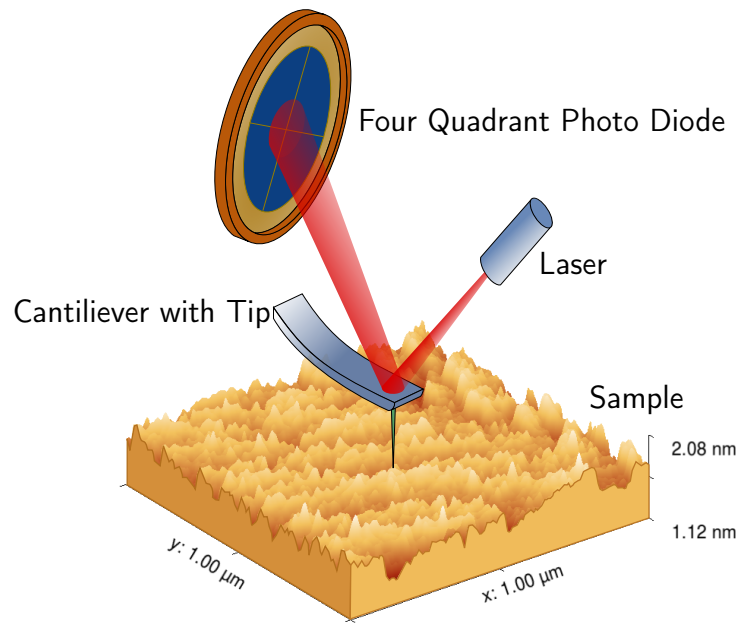


**Figure 5.12:** Schematic representation of an atomic force microscopy (AFM) setup. A measurement tip, which is in contact with the sample surface is located at the end of a spring loaded cantilever. The interaction of the measurement tip with the surface deforms the cantilever. A laser beam is reflected from the back of the cantilever onto a four-quadrant photo diode. By comparing the photo current produced in the four quadrants of the diode, the deflection of the beam, and hence, the deformation of the cantilever can be measured.

in contact with the surface. While the tip is moved across the sample, the deflection due to the topography of the surface is measured and the height of the cantilever is controlled such that the distance to the surface stays constant. Due to the close contact with the surface, operating the AFM in this mode may leave scratches on the sample surface or reduce the lifetime of the tip.

In tapping mode, the cantilever oscillates close to its resonance frequency. A control loop is used to keep amplitude and frequency of this oscillation constant. If the tip is close to the surface the amplitude of the oscillation will change since the interaction between the sample surface and will alter the resonance frequency of the system. In this case, the surface image can either be reconstructed from the amplitude or the phase signal of the oscillation.

## 5.4 Energy Dispersive X-ray Spectroscopy

Energy Dispersive X-Ray Spectroscopy (EDX), also commonly abbreviated EDS and XEDS, is a method to analyze of which elements a material is formed. As illustrated in figure 5.13, this method uses the characteristic X-Ray lines of atoms to distinguish between them. When high energy electrons are focused onto a sample they may transfer their energy to core electrons of the atoms in the sample, which are then ejected from the atom as secondary electrons. The vacancy in the inner shell which is created in this way is thereafter filled by an electron from any upper shell and the energy difference between the former and the new state of this electron is emitted via an X-Ray photon[75]. Hence, the energy of the photon provides information about the origin of the electron.

The line in the spectrum created by L shell electrons filling a K shell vacancy is referred to as  $K_\alpha$  line, while an M shell electron filling the same vacancy gives rise to the  $K_\beta$  line. Likewise is the  $L_\alpha$  line due to M electron filling an L shell vacancy and so forth.

A vacancy may be filled by electrons from any shell, however, electrons from different shells have different probabilities to do so. These probabilities manifest in an EDX measurements as the relative intensities measured from the different characteristic lines. Since the probability for a K shell vacancy to be filled by an L shell electron is higher than for M shell electron, the  $K_\alpha$  line will be stronger than the  $K_\beta$  line. Also these relative intensities are characteristic and may help to distinguish between elements.

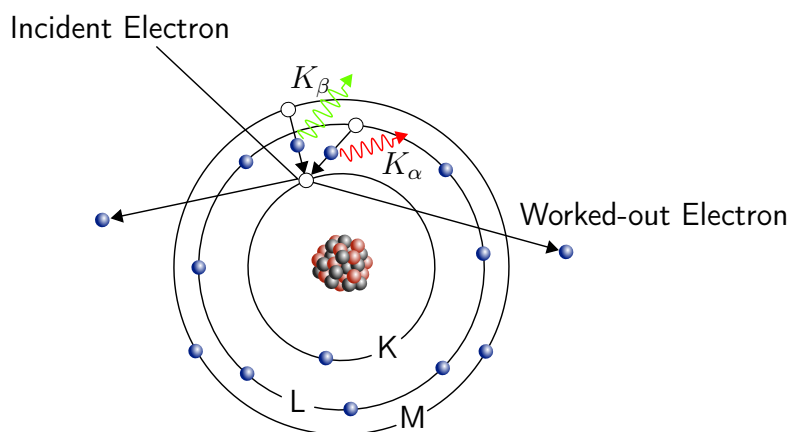


**Figure 5.13:** Generation of characteristic X-Ray photons by emission of secondary electrons. An incident electron with an energy above the ionization energy of the electrons in the K shell is incident to the atom. An electron in the K shell is excited and emitted as secondary electron. The hereby created hole state is filled by an electron of the L or M shell. The difference in energy of the former and the new state of this electron is emitted as characteristic X-Ray photon.



Since the energy difference between different shells of an atom depends on its atomic number, the lines we find in the X-Ray emission spectrum are called characteristic lines. The energy of K and L lines with respect to the atomic number is shown in figure 5.14. We can see that the energy of the lines rises with the atomic number and hence, heavier atoms require higher energies of the incident electrons. If e.g. the work required to excite the K lines is higher than this energy, only L lines will be found in the spectrum.

An example EDX spectrum is shown in figure 5.15. This spectrum measured from a multi-element glass sample K and L lines of various elements. For the light elements (O,Al,Si,Ca) we only find K lines. For Fe we find both K and L lines while very heavy elements like Ba only exhibit L lines in this measurements since the ionization threshold of the K shell electrons is above the energy of the electrons in the incident beam. Not only the energy at which they appear, but also the relative magnitude of the different lines is characteristic for an element, this can be seen e.g. from the L lines of Ba in figure 5.15. If the energies of the lines of different elements overlap, e.g. the L lines of Ba overlap with the K lines of V and Ti, the relative height of the lines can be used to determine the elements within the sample.

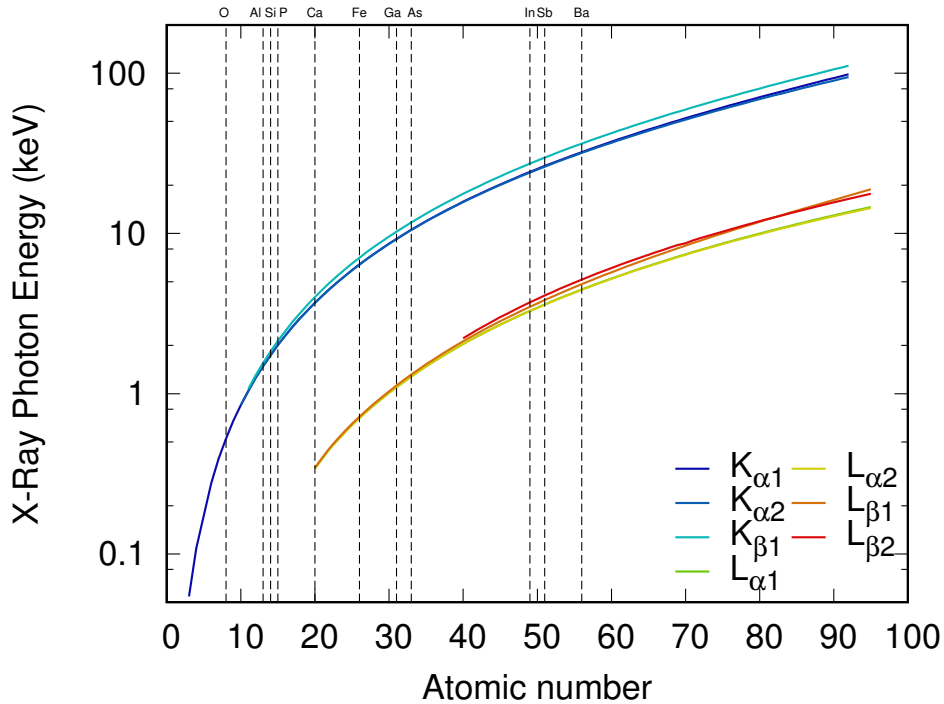


**Figure 5.14:** Energy of characteristic X-Ray photons versus Atomic number. Values taken from [76].

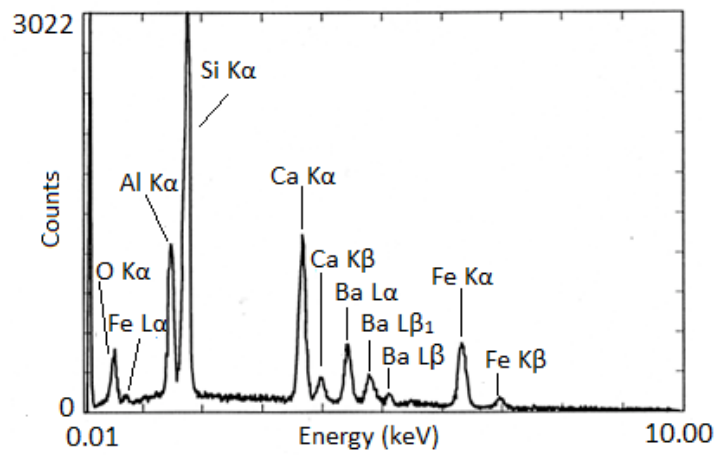


**Figure 5.15:** EDX spectrum of NIST K309 glass. Composition: O: 38.7 wt%, Si: 18.7 wt%, Ba: 13.4 wt%, Ca: 10.7 wt%, Fe: 10.5 wt%, Al: 7.94 wt%. Copyright holder: Andrew R. Barron, published under Creative Commons Attribution License (by 4.0), Taken from <http://cnx.org/contents/uieDnVBC@21.1:vcZrdZIQ@1/An-Introduction-to-Energy-Disp> (2016/05/04 16:22). Original by Goldstein, D. et. al. Springer, New York (2003)[75].

## CHAPTER 6

---

### MBE growth of InAs-based QCLs

---

In chapter 3 we have seen that the maximum operation temperature of THz-QCLs is still limited to cryogenic temperatures. In order to improve the performance of these devices, new material systems with beneficial properties have to be explored. It will be shown that well materials with a low effective electron mass can provide higher gain in QCLs and that the use of InAs is an interesting option for the further improvement of the temperature performance of these devices. In the following, different barrier materials will be discussed and it will be shown that  $\text{Al}_x\text{In}_{1-x}\text{As}_y\text{Sb}_{1-y}$  is a suitable material for the fabrication of InAs based lasers. We will furthermore see that substantial challenges arise when trying to grow this material. Thereafter we will see that careful tuning of the growth parameters allows for the growth of  $\text{Al}_x\text{In}_{1-x}\text{As}_y\text{Sb}_{1-y}$  with high crystal quality.

### 6.1 Influence of the Effective Electron Mass

In chapter 3.2 we have derived a simple expression for the intersubband gain in a quantum cascade structure. Using equation 3.20 and assuming fast depopulation of the lower laser level ( $\tau_2 \ll \tau_{32}$ ) we receive

$$g_c = \frac{\omega e |\langle z_{if} \rangle|^2}{\epsilon_0 n c L_p \gamma} \eta_i \tau_3. \quad (6.1)$$

### 6.1. Influence of the Effective Electron Mass

Well Material	$\frac{m^*}{m_0}$	$\frac{g_c}{g_{cGaAs}}$	exp. $\frac{QE}{QE_{GaAs}}$
GaAs	0.067	1.0	1.0
Ga <sub>0.47</sub> In <sub>0.53</sub> As	0.041	1.8	2.1
InAs	0.023	5.0	5.2

**Table 6.1:** Effective electron mass and gain coefficient ratios of different III/V semiconductors. Lower effective electron masses provide higher gain. The highest gain coefficient is found for structures based on InAs[77].

If we compare the gain in two structures designed to emit light of the same wavelength ( $\omega_a = \omega_b$ ), we will find that the ratio between their gain coefficients is given by

$$\frac{g_{ca}}{g_{cb}} = \frac{|\langle z_{if_a} \rangle|^2 \tau_{3a}}{|\langle z_{if_b} \rangle|^2 \tau_{3b}}. \quad (6.2)$$

Since

$$\langle z_{if} \rangle = \frac{8L}{\pi^2} \frac{ij}{(j^2 - i^2)^2}, \quad (6.3)$$

and for an infinitely deep quantum well, the energy separation between the upper and the lower laser state is given by

$$E_{ij} = \hbar\omega = \frac{\hbar^2 \pi^2}{2m^* L^2} (j^2 - i^2), \quad (6.4)$$

with  $L$  being the width of the quantum well,  $\langle z_{if} \rangle$  is found to be proportional to  $m^{*-\frac{1}{2}}$ .

At low temperatures  $\tau_3$  is limited by depopulation due to longitudinal optical (LO) phonons. In this case it can be shown that also  $\tau_3$  is proportional to  $m^{*-\frac{1}{2}}$  and hence the ratio of the gain coefficients is given by

$$\frac{g_{ca}}{g_{cb}} = \left[ \frac{m_a^*}{m_b^*} \right]^{-\frac{3}{2}}. \quad (6.5)$$

We see that the use of a well materials with a low effective mass can be beneficial for the performance of QCLs. In table 6.1, the effective masses and theoretical gain coefficient ratios of different well materials are compared. We see that the use of Ga<sub>0.47</sub>In<sub>0.53</sub>As should provide an almost two fold increase in the gain coefficient of a QCL with respect to GaAs. An even higher ratio is found when we switch from GaAs to InAs, since these structures should provide a five fold increase in the gain coefficient.

The quantum efficiency of intersubband devices employing different well materials has been measured by Benveniste et. al.[77]. It was found that indeed, devices based on low effective-electron-mass materials show a higher QE and that the ratio of the QEs

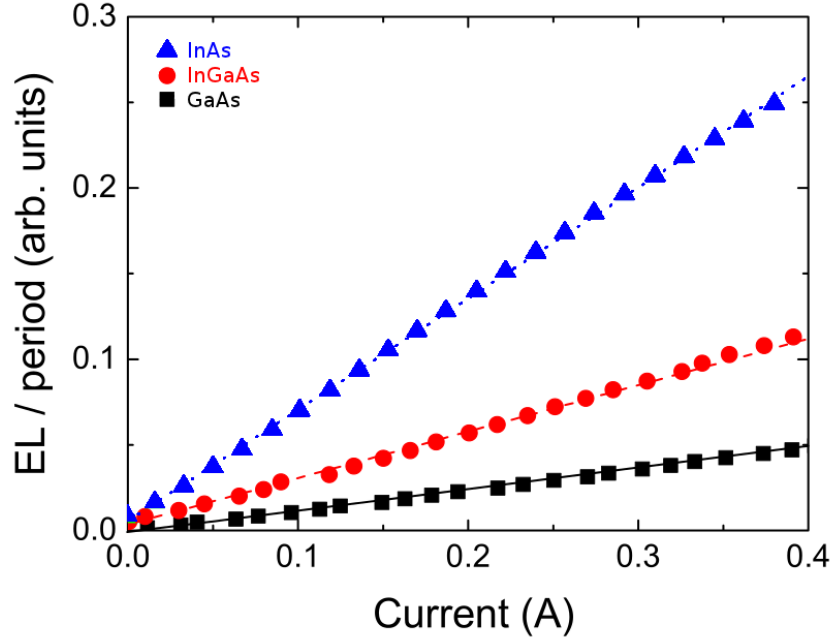


**Figure 6.1:** Electroluminescence per period measured from intersubband devices using different well materials. The measurement clearly shows an enhanced Quantum Efficiency (QE) for materials having a lower effective mass. Taken from [77].

closely follows the effective mass ratio that was derived in equation 6.5. The results of this experiment are summarized in figure 6.1 and table 6.1.

## 6.2 Barrier Materials for InAs Based QCLs

Since a QCL is built out of at least two different materials, one being the well, one being the barrier material, a well suited partner for InAs is necessary. In section 4.1.1 we have seen that a low lattice mismatch between the well and the barrier material is necessary in order to grow thick structures like QCLs. Hence, only a hand full of materials are qualified as potential barrier materials. A review on these materials can be found in [78]. Figure 6.2 shows some of these materials. Of the binary alloys AlSb and GaSb are have the smallest lattice mismatch with InAs. However, since the critical thickness of these materials is on the order of a few nm when they are grown on InAs, they are not suitable for the growth of QCL structures.

The two ternary alloys  $\text{GaAs}_{1-x}\text{Sb}_x$  and  $\text{AlAs}_{1-x}\text{Sb}_x$  can be grown lattice matched to InAs.  $\text{GaAs}_{0.91}\text{Sb}_{0.09}$  shows a conduction band offset of 0.93 eV and a broken gap configuration. Although intersubband devices using these materials have been discussed theoretically, no reports on experimental realizations can be found in literature.

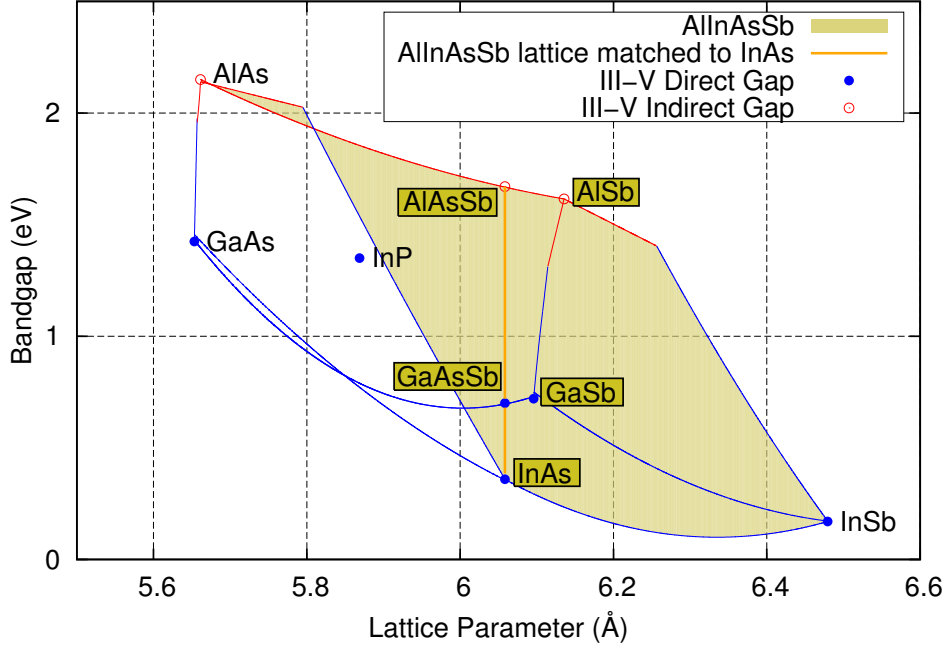


**Figure 6.2:** III/V semiconductors which are considered part of the 6.1 Å family. The binary alloys AlSb and GaSb show a high degree of lattice mismatch with InAs. The ternary alloys  $\text{AlAs}_{1-x}\text{Sb}_x$  and  $\text{GaAs}_{1-x}\text{Sb}_x$ , as well as all compositions of the quaternary  $\text{Al}_x\text{In}_{1-x}\text{As}_y\text{Sb}_{1-y}$  alloy, indicated by the shaded area, which reside on the line connecting InAs and  $\text{AlAs}_{1-x}\text{Sb}_x$  can be grown lattice matched with InAs.

$\text{AlAs}_{0.16}\text{Sb}_{0.84}$  shows an indirect conduction band offset of 1.2 eV and a direct conduction band offset of 2.2 eV. This makes it an interesting barrier material for short wavelength QCLs. Although excellent results for mid-infrared (MIR) devices [79, 80, 37, 81], have been shown using this materials, devices designed to emit in the terahertz (THz) regime require the use of monolayer and sub-monolayer thin barriers. The growth of such thin layers is very difficult to control, and to date, no THz laser operation has been shown.

A viable option for the barrier material is the quaternary  $\text{Al}_x\text{In}_{1-x}\text{As}_y\text{Sb}_{1-y}$  material which is indicated by the shaded area in figure 6.2. The vertical line which connects InAs and  $\text{AlAs}_{0.16}\text{Sb}_{0.84}$  indicated those compositions which are lattice matched to InAs and hence would be suitable for the growth of QCLs. Having InAs and  $\text{AlAs}_{0.16}\text{Sb}_{0.84}$  as its endpoints, this material should allow for the tuning of its properties and provide a similar flexibility as the GaAs/ $\text{Al}_x\text{Ga}_{1-x}\text{As}$  material system. By choosing an appropriate composition, it would be possible to grow InAs based THz-QCLs with a suitably low conduction band offset and therefore easy to control barrier thicknesses.

A Summary of the properties of possible barrier materials is given in figure 6.3.

	GaSb	AlSb	$\text{AlAs}_{1-x}\text{Sb}_x0.16$	$\text{Al}_x\text{In}_{1-x}\text{As}_y\text{Sb}_{1-y}$
Lattice Constant	6.10	6.14	6.06	6.06
Mismatch	0.6 %	1.3 %	0.0 %	0.0 %
$E_c$	0.93 eV	1.35 eV	1.2 eV	0 eV to 1.2 eV
Band Alignment	Broken gap	Type II	Type I	Type I

The figure displays four energy band diagrams for different barrier materials grown on an InAs substrate. Each diagram shows the conduction band (CB) and valence band (VB) of the barrier material relative to the InAs bands. GaSb shows a broken gap with a 0.78 eV offset and a 0.15 eV barrier. AlSb shows a Type II alignment with a 1.35 eV offset. AlAsSb shows a Type I alignment with a 1.2 eV offset. AlInAsSb shows a Type I alignment with a tunable band offset.

**Figure 6.3:** Properties of Barrier material that can be grown on InAs. The binary alloys GaSb and AlSb show a high lattice mismatch with InAs, hence thick structures are not possible. The ternary  $\text{AlAs}_{0.16}\text{Sb}_{0.84}$  alloy can be grown lattice matched but shows a very high conduction band offset. The quaternary  $\text{Al}_x\text{In}_{1-x}\text{As}_y\text{Sb}_{1-y}$  alloy can be grown lattice matched to InAs with a tunable band offset.

### 6.3 $\text{Al}_{0.20}\text{In}_{0.80}\text{As}_y\text{Sb}_{1-y}$ Barrier determination

The conduction band offset is an important material parameter for the design of QCLs. Since the dependency of the conduction band offset between InAs and  $\text{Al}_x\text{In}_{1-x}\text{As}_y\text{Sb}_{1-y}$  on its composition is not known, a first order approximation was used to estimate which composition will result in a band offset, sufficient for the fabrication of intersubband devices. Under this assumption and following the data given by Kroemer[78] an Sb mole fraction of 0.2 should provide a conduction band offset of roughly 400 meV, which is appropriate for the design of a THz-QCL structure.

Since initial C-V measurements at room temperature did not show signs of rectifying behavior, a Thermionic emission (TE) experiment was carried out, in order to determine the conduction band offset between InAs and  $\text{Al}_{0.20}\text{In}_{0.80}\text{As}_y\text{Sb}_{1-y}$ . TE is largely used for the determination of conduction band discontinuities between III/V semiconductors by measuring the current across a barrier under low bias. Since the density of electrons at a certain energy is defined by Fermi-Dirac statistics, the number of electrons above a certain energy depends exponentially on the temperature[82]. As shown in figure 6.4, if a

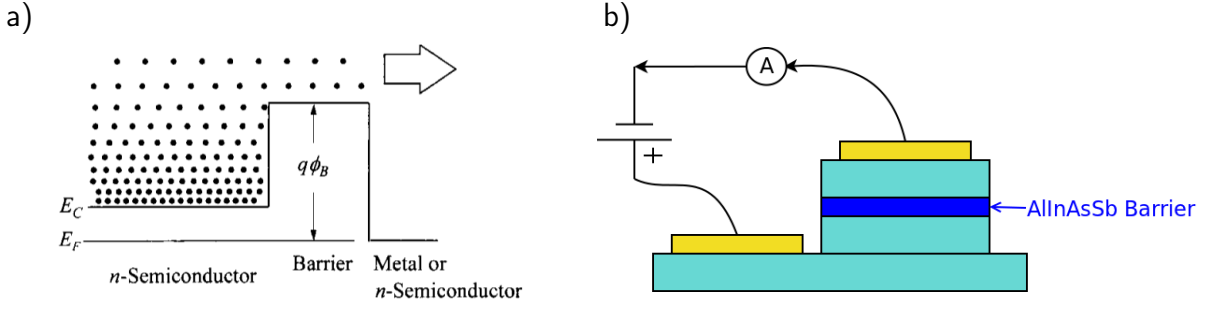


**Figure 6.4:** Principle of thermionic emission. A low bias is applied to the barrier, the measured current density is related to the temperature and the barrier height, since only electrons which are above the barrier contribute to the current. (a) Taken from[82].

low bias is applied to the barrier, only those electron will contribute to the current which are at energies above the barrier. Hence, TE measures the integrated number of carriers above a barrier, and the current density is given by

$$J = A^*T^2 e^{-\frac{q\Phi_G}{k_B T}}, \quad (6.6)$$

where  $q$  is the electron charge,  $k_B$  is the Boltzmann constant  $T$  is the absolute temperature and  $A^*$  is a material specific pre-exponential factor called the Richardson constant. As shown in figure 6.5, the barrier height  $\Phi_G$  is given by a linear fit to  $\ln(JT^{-2})$ .

Hickmott and coworkers used this technique to find the conduction band discontinuity between GaAs and  $\text{Al}_{0.4}\text{Ga}_{0.6}\text{As}$ [83]. An undoped  $\text{Al}_{0.4}\text{Ga}_{0.6}\text{As}$  layer was sandwiched between a highly and a lightly n-type GaAs layers, and capacitance-voltage and current-voltage measurements were performed. The conduction band discontinuity  $\Phi_B$  is obtained through

$$\Phi_B = \Phi_G(0) + \eta_G - \Psi_G - \Phi_{MB}, \quad (6.7)$$

where  $\Phi_G(0)$  is the measured barrier height extrapolated to zero barrier thickness,  $\Psi_G$  is the band bending in the gate,  $\eta_G$  is the position of the Fermi level above the conduction band edge in the gate, and  $\Phi_{MB}$  is a correction for many body effects due to high doping in the gate. The authors measured a  $\Phi_G(0)$  of 300 meV and from that calculate a conduction band discontinuity of 630 meV.

Peng and coworkers used the same technique to determine the band offset between  $\text{Ga}_{0.47}\text{In}_{0.53}\text{As}$  and  $\text{Al}_{0.48}\text{In}_{0.52}\text{As}$  grown on InP[84]. For this measurement 25 nm and 40 nm thick, undoped  $\text{Al}_{0.48}\text{In}_{0.52}\text{As}$  layers were sandwiched between n-type  $\text{Ga}_{0.47}\text{In}_{0.53}\text{As}$  layers, and measured a barrier height of 360 meV from which a conduction band offset of 510 meV is calculated.



In order to determine the conduction band offset, single layers of  $\text{Al}_{0.20}\text{In}_{0.80}\text{As}_y\text{Sb}_{1-y}$  were grown in a Riber 32 MBE system on indium bonded (100), n-type InAs substrates. The growth rates of AlAs (on InAs) ( $R_{\text{AlAs}}$ ) and InAs ( $R_{\text{InAs}}$ ) were determined using double superlattice structures and set to  $0.0843 \text{ ML s}^{-1}$  and  $0.3251 \text{ ML s}^{-1}$  respectively. As flux was supplied as tetramers using a cracking zone temperature of  $650^\circ\text{C}$  at a  $P_{\text{As}_4}$  of  $1.33 \times 10^{-5}$  torr. Sb flux was supplied in form of dimers using a cracking zone temperature of  $1000^\circ\text{C}$ . Lattice matching was achieved at an  $P_{\text{Sb}_2}$  of  $2.71 \times 10^{-7}$  torr. The structural quality of the samples was confirmed by HRXRD and AFM measurements.

Figure 6.5 shows thermionic emission measurements performed on pillars of  $700 \mu\text{m}$  diameter at different bias voltages. We can see that the slope does not change with the applied bias and hence it can be concluded that the current density is only defined by thermionic emission. The conduction band offset measured in this experiment was  $\sim 80 \text{ meV}$ .

Reports in literature about measurements performed on  $\text{Ga}_{0.47}\text{In}_{0.53}\text{As}/\text{Al}_{0.48}\text{In}_{0.52}\text{As}$  and  $\text{GaAs}/\text{Al}_{0.4}\text{Ga}_{0.6}\text{As}$ , suggest that the contributions of  $\eta_G$ ,  $\Psi_G$  and  $\Phi_{MB}$  have to be fairly large with respect to the measured  $\Phi_G$  for the conduction band offset between  $\text{Al}_{0.20}\text{In}_{0.80}\text{As}_y\text{Sb}_{1-y}$  and InAs. This makes the value that would be obtained through this method very questionable. Moreover, since no rectifying behavior could be measured at room temperature,  $\eta_G$  could not be determined for these structures. Furthermore, surface pinning of the Fermi level is known to cause electron accumulation at the InAs surface [78, 85, 86, 87], this effect can strongly influence the barrier height measured in the TE experiment by creating a parallel current path.

The results obtained in this experiment suggest that a higher conduction band offset, and hence a higher Al mole fraction in the  $\text{Al}_x\text{In}_{1-x}\text{As}_y\text{Sb}_{1-y}$  layers is necessary in order for this material to be used for intersubband devices.

## 6.4 $\text{Al}_{0.462}\text{In}_{0.538}\text{As}_y\text{Sb}_{1-y}$

This section is based on Ref [89].

Due to the strict requirements towards lattice matching for intersubband devices, the growth of  $\text{Al}_x\text{In}_{1-x}\text{As}_y\text{Sb}_{1-y}$  can be very challenging. Great control over the fluxes of the four atom species, as well as the temperature of the substrate are necessary in order to achieve the desired composition. Moreover, large miscibility gaps exist in quaternary alloys of III/V materials [90, 91, 92].

Within this region the four atom species will not form a homogeneous alloy but will decompose making it impossible to obtain single crystalline material using equilibrium

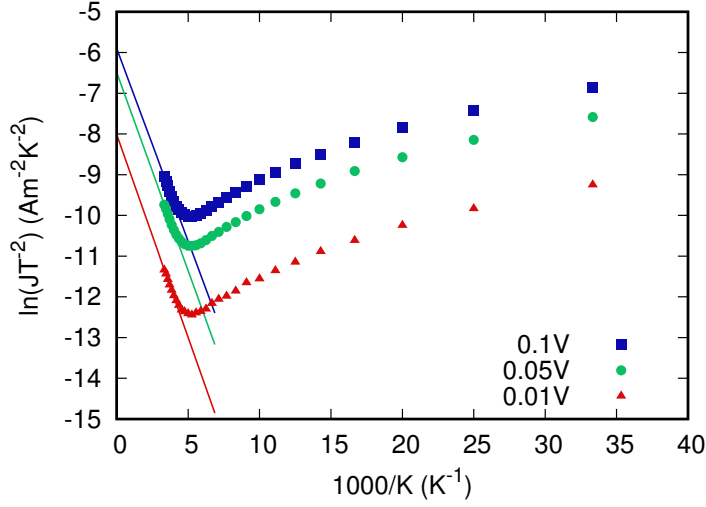


**Figure 6.5:** Thermionic emission measurement of the conduction band offset between InAs and  $\text{Al}_{0.20}\text{In}_{0.80}\text{As}_y\text{Sb}_{1-y}$ . For pillars with a diameter of  $700\text{ }\mu\text{m}$ , the TE measurement was performed at bias voltages between  $0.01\text{ V}$  to  $0.1\text{ V}$ . At all bias voltages a  $\Phi_G$  of  $\sim 80\text{ meV}$  was measured.

growth techniques like Liquid Phase Epitaxy (LPE). Since MBE happens far from equilibrium, it is possible to obtain perfectly mixed alloys with compositions which are impossible with LPE, however, significant challenges may still arise with these regions[92, 88]. Figure 6.6 shows binodal and spinodal decompositions lines of  $\text{Al}_x\text{In}_{1-x}\text{As}_y\text{Sb}_{1-y}$  calculated at  $450^\circ\text{C}$ .

Reports about the growth of  $\text{Al}_x\text{In}_{1-x}\text{As}_y\text{Sb}_{1-y}$  at various compositions can be found in literature, however, most of these works do not specifically study the growth of the  $\text{Al}_x\text{In}_{1-x}\text{As}_y\text{Sb}_{1-y}$  material and hence little information exists on the effect of the various growth parameters on the crystal quality and layer composition. An overview of the compositions and the respective growth temperatures is given in Figure 6.7. Turner *et al.* [93] and Wilk *et al.* [94] report on the growth  $\text{Al}_x\text{In}_{1-x}\text{As}_y\text{Sb}_{1-y}$  with Al mole fractions below 0.20 at growth temperatures ( $T_g$ ) of  $430^\circ\text{C}$  and  $420^\circ\text{C}$ , while Semenov *et al.* [88] show that compositions with Al mole fractions of up to 0.25 can be grown at a  $T_g$  of  $450^\circ\text{C}$  to  $500^\circ\text{C}$ . For the greatest flexibility when it comes to designing devices employing  $\text{Al}_x\text{In}_{1-x}\text{As}_y\text{Sb}_{1-y}$ , composition with higher Al mole fractions have to be investigated and conditions have to be found which suit the widest range of compositions. The growth of  $\text{Al}_x\text{In}_{1-x}\text{As}_y\text{Sb}_{1-y}$  on GaAs with higher Al mole fractions is reported at a  $T_g$  well below  $400^\circ\text{C}$ . Kudo *et al.* [95] studied the incorporation of Sb into  $\text{Al}_x\text{In}_{1-x}\text{As}_y\text{Sb}_{1-y}$  with an Al mole fraction of 0.5 at a  $T_g$  of  $350^\circ\text{C}$  grown on GaAs. The authors report a high dislocation density, found in a transmission electron microscopy study of the grown material, resulting

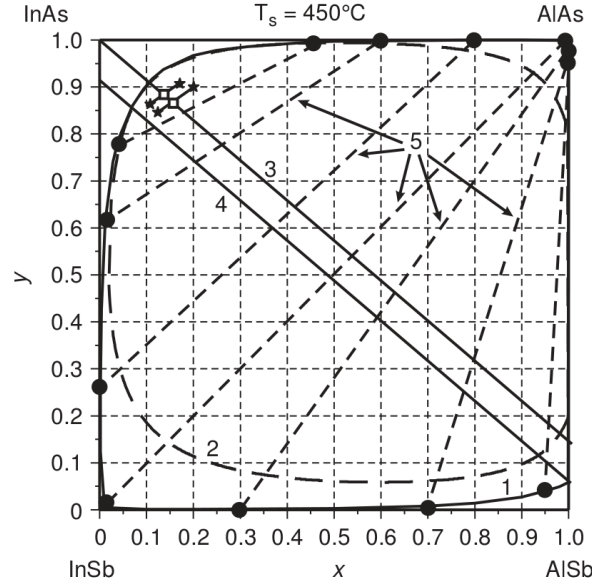


**Figure 6.6:** Instability region of  $\text{Al}_x\text{In}_{1-x}\text{As}_y\text{Sb}_{1-y}$  calculated using a regular solid solution model at  $450^\circ\text{C}$ . The binodal isotherm is indicated by the solid line (1). The spinodal isotherm is given by the dashed line (2). The simulation shows that the instability region for this alloy is relatively large. Although MBE is a non equilibrium process, the growth of compositions which reside within the instability region is expected to be challenging. Taken from [88].

from the highly lattice-mismatched conditions. It is questionable whether this result is applicable to the growth of  $\text{Al}_x\text{In}_{1-x}\text{As}_y\text{Sb}_{1-y}$  on InAs. Washington-Stokes *et al.* [96] report on the growth of  $\text{Al}_x\text{In}_{1-x}\text{As}_y\text{Sb}_{1-y}$  with an Al mole fraction between 0.37 and 0.72 at a  $T_g$  between  $355^\circ\text{C}$  and  $378^\circ\text{C}$  on GaSb substrates and report good crystal quality for the grown layers. The influence of the Sb and As beam equivalent pressures (BEP) or the  $T_g$  on the quality and composition of the layers is not mentioned.

The lack of information on the growth of  $\text{Al}_x\text{In}_{1-x}\text{As}_y\text{Sb}_{1-y}$  with Al mole fractions around 0.5 at a  $T_g$  above  $400^\circ\text{C}$  suggests that challenges, possible due to its miscibility gap, arise from such conditions. Since high crystal quality is expected to be achieved at high  $T_g$ , the upper limit for the growth of  $\text{Al}_x\text{In}_{1-x}\text{As}_y\text{Sb}_{1-y}$  and the dependence of the crystal quality on the  $T_g$  have to be investigated.

## 6.5 MBE Growth of $\text{Al}_{0.462}\text{In}_{0.538}\text{As}_y\text{Sb}_{1-y}$

$\text{Al}_x\text{In}_{1-x}\text{As}_y\text{Sb}_{1-y}$  with an aluminum mole fraction fixed to 0.462, was grown on InAs. The growth rates of AlAs (on InAs) ( $R_{\text{AlAs}}$ ) and InAs ( $R_{\text{InAs}}$ ) were determined using triple superlattice structures. The structure of the samples was adjusted to minimize the error of the measurement and the obtained growth rates were correlated the measured

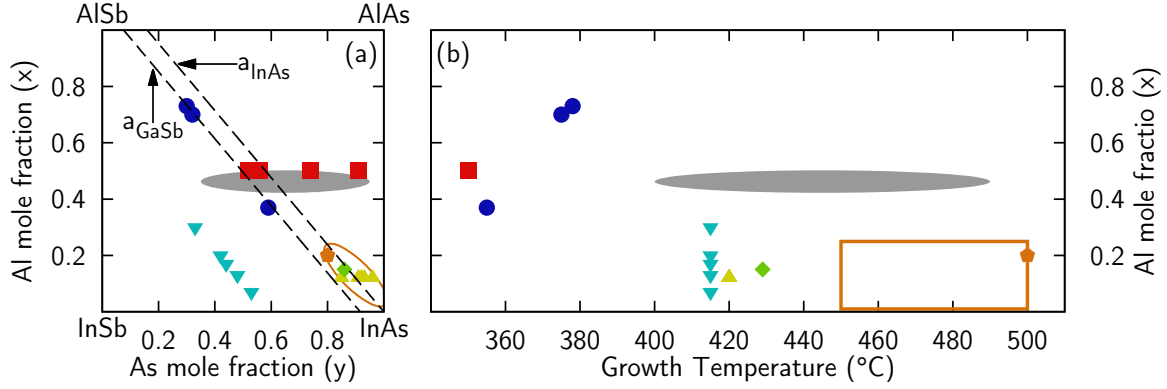


**Figure 6.7:** Reports on the growth of  $\text{Al}_x\text{In}_{1-x}\text{As}_y\text{Sb}_{1-y}$  found in literature. (a) Compositions and (b) their respective  $T_g$ . The dashed lines in (a) indicate the compositions of  $\text{Al}_x\text{In}_{1-x}\text{As}_y\text{Sb}_{1-y}$  which are lattice matched to InAs or GaSb according to Vegard's Law. (orange diamond condition explicitly mentioned; the range studied is indicated by the outlined areas) Semenov *et al.* [88] grown on InAs; similar results were obtained by Rojas-Ramirez *et al.* [97]; (blue circle) Washington-Stokes *et al.* [96] grown on GaSb; (green diamond) Turner *et al.* [93] grown on GaSb; (red square) Kudo *et al.* [95] grown on GaAs; (yellow triangle) Wilk *et al.* [94] grown on InAs; (cyan inverted triangle) Sarney *et al.* [98] grown on a lattice-constant shifting AlGaInSb buffer on GaSb; The regions of temperature and composition studied within this work are indicated by the gray shaded areas.

Beam Equivalent Pressure (BEP). Both group III growth rates were kept constant for all samples.  $R_{\text{AlAs}}$  was set to 0.25 monolayers per second ( $\text{MLs}^{-1}$ ) which corresponds to an aluminum BEP  $1.3 \times 10^{-7}$  torr.  $R_{\text{InAs}}$  was set to  $0.29 \text{ MLs}^{-1}$  equaling an indium BEP of  $4.5 \times 10^{-7}$  torr. For the comparison of the group V BEPs to other MBE systems, the  $\text{As}_2$  flux was calibrated by the  $(2 \times 4)$  to  $(4 \times 2)$  transition during growth at different temperatures and normalized to  $1 \text{ MLs}^{-1}$ . A fit to the exponential function  $P_{\text{As}_2}(T) = a + be^{\frac{T}{c}}$  resulted in the parameters  $a = 0.531$  torr,  $b = 2.14 \times 10^{-14}$  torr,  $c = 23.24 \text{ K}^{-1}$ .

To find the optimum growth conditions,  $T_g$ ,  $\text{As}_2$  BEP ( $P_{\text{As}_2}$ ) and  $\text{Sb}_2$  BEP ( $P_{\text{Sb}_2}$ ) were varied. The range of  $T_g$  used in this study was  $410^\circ\text{C}$  to  $480^\circ\text{C}$ . Since  $\text{Al}_x\text{In}_{1-x}\text{As}_y\text{Sb}_{1-y}$  should be used in heterostructures with InAs,  $P_{\text{As}_2}$  is in principle, dictated by the optimum BEP to grow high quality InAs [99]. In this study,  $P_{\text{As}_2}$  was varied in order to investigate its influence on the composition of  $\text{Al}_{0.462}\text{In}_{0.538}\text{As}_y\text{Sb}_{1-y}$ . The growth parameter regions investigated in this study are indicated by the gray shaded areas in Figure 6.7.

To investigate the influence of growth parameters, a set of samples was grown in a Riber 32 MBE system on indium-bonded n+ InAs (001) wafers. For the group V materials, valved cracking cells were used with the cracking zone temperatures set to  $850^\circ\text{C}$  and  $1000^\circ\text{C}$  to produce  $\text{As}_2$  and  $\text{Sb}_2$  respectively. For all samples, first the oxide was thermally desorbed under  $P_{\text{As}_2}$  of  $1.5 \times 10^{-5}$  torr at  $510^\circ\text{C}$  for 20 min. The temperature

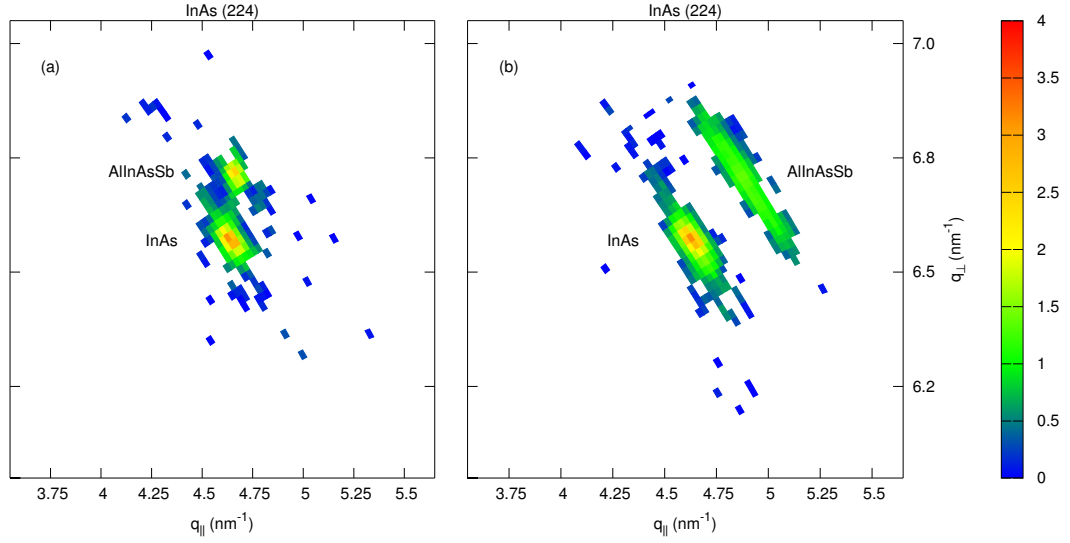


**Figure 6.8:** Reciprocal space maps around the InAs (224) diffraction. (a) The  $\text{Al}_{0.462}\text{In}_{0.538}\text{As}_y\text{Sb}_{1-y}$  is fully strained. The in-plane lattice constant ( $q_{\parallel}$ ) is the same as that of the substrate while the out-of-plane lattice constant is smaller. (b) The  $\text{Al}_{0.462}\text{In}_{0.538}\text{As}_y\text{Sb}_{1-y}$  layer is partially relaxed. The in-plane lattice constant is different from that of the substrate. The layer peak is strongly broadened in the  $\omega$  direction which is a sign of a high dislocation density, resulting from the relaxation.

was then reduced to 480 °C where a 150 nm InAs buffer layer was grown to enhance the surface quality after the desorption of the oxide. Next, the  $T_g$  was adjusted to the growth temperature, at which a 150 nm thick  $\text{Al}_{0.462}\text{In}_{0.538}\text{As}_y\text{Sb}_{1-y}$  layer and a 5 nm InAs cap, were grown.

All fabricated heterostructures were measured with HRXRD to investigate the crystal quality and composition. Figure 6.8 shows two typical reciprocal space maps of  $\text{Al}_{0.462}\text{In}_{0.538}\text{As}_y\text{Sb}_{1-y}$  layers. Subfigure (a) shows a fully strained sample for which the in-plane lattice constant is the same as the that of the substrate. Subfigure (b) shows a relaxed sample for which both the in-plane and the out-of-plane lattice constants are different from that of the substrate.

The out-of-plane lattice constant is used to calculate an initial guess for the composition. Using this composition the stiffness coefficients of the alloy are calculated from table 4.1 using Vegard's law. The native lattice constant of the alloy is the calculated using

$$a_0^L = \frac{C_{11}}{C_{11} + 2C_{12}}(a_{\perp}^L - a_{\parallel}^L) + a_{\parallel}^L. \quad (6.8)$$

From this lattice constant again the composition of the alloy is derived and the stiffness coefficients are calculated. This process is repeated until the  $a_0^L$  converges. AFM was used to determine the surface roughness of all samples.

## 6.5.1 Influence of the Substrate Temperature

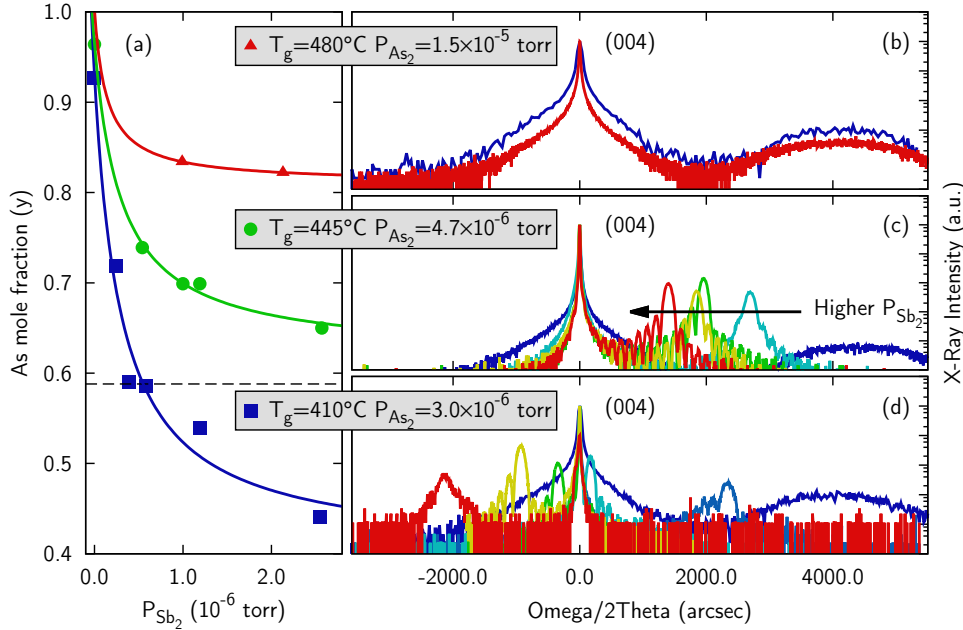


**Figure 6.9:** (a) As mole fraction ( $y$ ) in  $\text{Al}_{0.462}\text{In}_{0.538}\text{As}_y\text{Sb}_{1-y}$  layers with respect to  $P_{\text{Sb}_2}$  at the values for  $T_g$  and  $P_{\text{As}_2}$  shown in (b–d). Lattice-matching (indicated by the dashed line at  $y = 0.588$ ) is only achieved at  $410^\circ\text{C}$ . high resolution x-ray diffraction (HRXRD) measurements around the InAs (004) diffraction of samples grown at (b)  $480^\circ\text{C}$ ,  $P_{\text{As}_2} = 1.5 \times 10^{-5}$  torr (c)  $445^\circ\text{C}$ ,  $P_{\text{As}_2} = 4.7 \times 10^{-6}$  torr (d)  $410^\circ\text{C}$ ,  $P_{\text{As}_2} = 3.0 \times 10^{-6}$  torr. Fully strained films are found for samples grown at intermediate  $P_{\text{Sb}_2}$  values at  $410^\circ\text{C}$  and  $445^\circ\text{C}$ .  $P_{\text{Sb}_2}$  in the subfigures (b–d) given in  $1 \times 10^{-6}$  torr starting from the left most peak: (b): ■ 2.13 ■ 0.99 (c): ■ 2.57 ■ 1.19 ■ 1.00 ■ 0.54 ■ 0.00 (d): ■ 2.55 ■ 1.19 ■ 0.58 ■ 0.39 ■ 0.24 ■ 0.00 .

To investigate the incorporation of Sb into  $\text{Al}_{0.462}\text{In}_{0.538}\text{As}_y\text{Sb}_{1-y}$ , three series of samples were grown. For each series  $P_{\text{As}_2}$  and the  $T_g$  were kept constant while  $P_{\text{Sb}_2}$  was varied.  $P_{\text{As}_2}$  was chosen such that high crystal quality InAs can be grown under the same conditions [99]. The results are summarized in Figure 6.9a. It shows that with increasing  $P_{\text{Sb}_2}$ , the rate of Sb incorporation is lowered and a maximum achievable Sb mole fraction is approached asymptotically. Only at a  $T_g$  of  $410^\circ\text{C}$  can lattice matching with InAs be achieved. An explanation for this behavior may be found in the As-for-Sb exchange reaction found for other mixed group V materials like  $\text{GaAs}_{1-x}\text{Sb}_x$  [100]. Due to its negative enthalpy, this reaction is favored with respect to the reverse reaction and its rate rises with  $T_g$  for experiments using  $\text{As}_2$ , which is in agreement with our observations.

HRXRD measurements, shown in figure 6.9b–d, show high crystal quality for a  $P_{\text{Sb}_2}$  between  $0.5 \times 10^{-6}$  torr and  $1 \times 10^{-6}$  torr at  $T_g$  of  $410^\circ\text{C}$  as well as  $1 \times 10^{-6}$  torr and  $2.5 \times 10^{-6}$  torr at  $445^\circ\text{C}$   $T_g$ . This is indicated by sharp layer peaks and Pendellösung



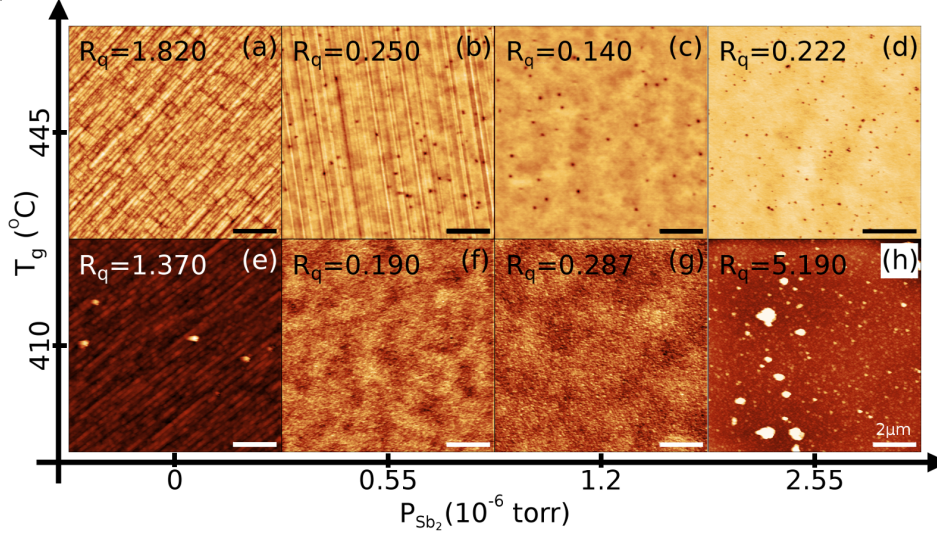


**Figure 6.10:** AFM images of samples grown at 445 °C (a–d) 410 °C (e–h) with root mean square roughness values ( $R_q$ ).  $P_{\text{Sb}_2}$  is increased left-to-right. Samples grown at low  $P_{\text{Sb}_2}$  show crosshatch due to the high lattice mismatch (a,b,e). At intermediate  $P_{\text{Sb}_2}$ , smooth films are obtained (c,d,f,g). At high  $P_{\text{Sb}_2}$ , high surface roughness is observed (h), scale bar = 2  $\mu\text{m}$ . Peak-to-valley values are: (a) 15.9 nm; (b) 3.2 nm; (c) 3.9 nm; (d) 6.4 nm; (e) 23.7 nm; (f) 1.8 nm; (g) 1.5 nm; (h) 44.2 nm.

fringes. At lower  $P_{\text{Sb}_2}$ , the layer peaks are broadened due to partial relaxation resulting from the high lattice mismatch. At 410 °C, even higher  $P_{\text{Sb}_2}$  also leads to peak broadening. The respective (224) reciprocal space map shows partial relaxation. Strong peak broadening due to partial relaxation was also found for all samples grown at 480 °C

AFM measurements performed on the same heterostructures, shown in Figure 6.10, confirm these observations. Layers containing very little Sb show crosshatch patterns, a sign of partial relaxation. When the  $P_{\text{Sb}_2}$  is increased to values between  $0.5 \times 10^{-6}$  torr and  $1 \times 10^{-6}$  torr for a  $T_g$  of 410 °C and  $1 \times 10^{-6}$  torr and  $2.5 \times 10^{-6}$  torr at 445 °C, the surface roughness is dramatically reduced and no sign of crosshatch can be found. At  $2.55 \times 10^{-6}$  torr and a  $T_g$  of 410 °C, the measurements show an increased surface roughness. Since these conditions cause a 3-D growth mode it is evident that excess  $\text{Sb}_2$  has to be avoided at low  $T_g$  in order to achieve high crystal quality.

### 6.5.2 Temperature limit for lattice matching

To determine at which substrate temperature lattice matching can be achieved within the applied growth parameter limits, a series of samples was grown at the maximum  $\text{Sb}_2$  pressure. At each temperature the  $\text{As}_2$  pressure was chosen by first finding the  $(2 \times 4)/(4 \times 2)$  transition of InAs and then increasing the pressure until a stable  $(2 \times 4)$  reconstruction was observed by RHEED. We consider this pressure the absolute minimum

for the growth of InAs. For high quality InAs layers, however, an even higher  $\text{As}_2$  pressure is necessary. The result is given in figure 6.11. It shows the respective  $\text{As}_2$  pressure for each temperature (Fig. 6.11(a)) as well as the measured As mole fraction in the grown  $\text{Al}_{0.462}\text{In}_{0.538}\text{As}_y\text{Sb}_{1-y}$  layer (Fig. 6.11(b)). We can see an almost linear increase in the As mole fraction found in the  $\text{Al}_{0.462}\text{In}_{0.538}\text{As}_y\text{Sb}_{1-y}$  layer with the temperatures. The restrictions we applied allow for lattice matching of  $\text{Al}_{0.462}\text{In}_{0.538}\text{As}_y\text{Sb}_{1-y}$  with InAs, indicated by the dashed line, only at growth temperatures of 445 °C and below.

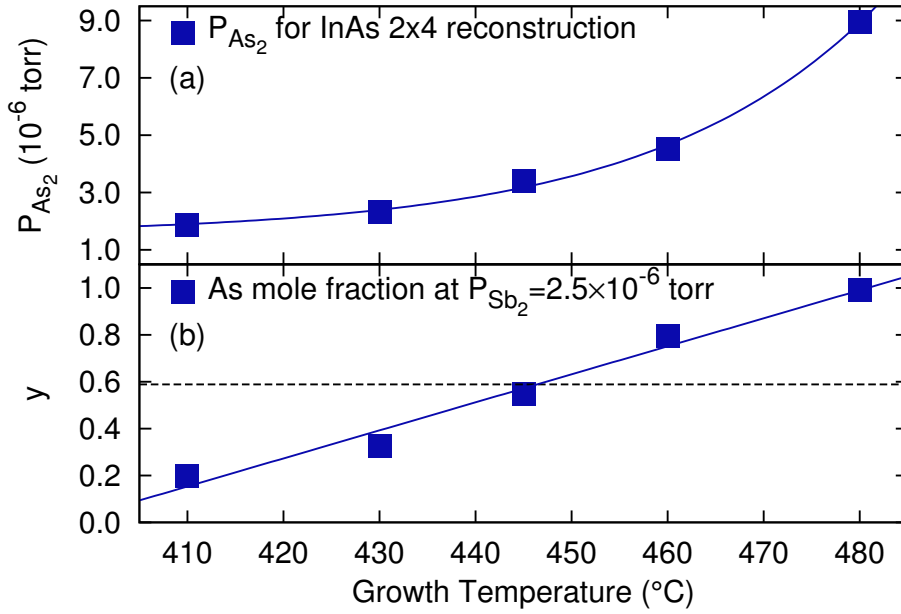


**Figure 6.11:** Maximum achievable As mole fraction ( $y$ ) in  $\text{Al}_{0.462}\text{In}_{0.538}\text{As}_y\text{Sb}_{1-y}$  at  $P_{\text{Sb}_2}=2.5 \times 10^{-5}$  torr. The  $\text{As}_2$  pressure was chosen such that InAs changes from a  $(2 \times 4)$  to a  $(4 \times 2)$  RHEED reconstruction, this is considered the absolute minimum to grow InAs, although the  $\text{As}_2$  pressure for optimal InAs quality should be higher. At the constant  $\text{Sb}_2$  pressure used in this experiment, lattice matched  $\text{Al}_{0.462}\text{In}_{0.538}\text{As}_y\text{Sb}_{1-y}$  can only be grown at substrate temperatures of 445 °C and below

### 6.5.3 Influence of $P_{\text{As}_2}$

Although it is convenient to keep  $P_{\text{As}_2}$  at a value that is optimal for the growth of the InAs throughout the whole growth, it is possible to change the conditions for each layer, since modern As cracking cells are equipped with valves that allow for the quick change of the flux. It could be beneficial to change  $P_{\text{As}_2}$  to a lower value for the growth of  $\text{Al}_x\text{In}_{1-x}\text{As}_y\text{Sb}_{1-y}$  in order to achieve a lower As mole fraction in the layer and hereby circumvent the restrictions imposed by the growth of InAs. To investigate the influence of  $P_{\text{As}_2}$  on the composition of  $\text{Al}_{0.462}\text{In}_{0.538}\text{As}_y\text{Sb}_{1-y}$ , a series of samples was grown in which



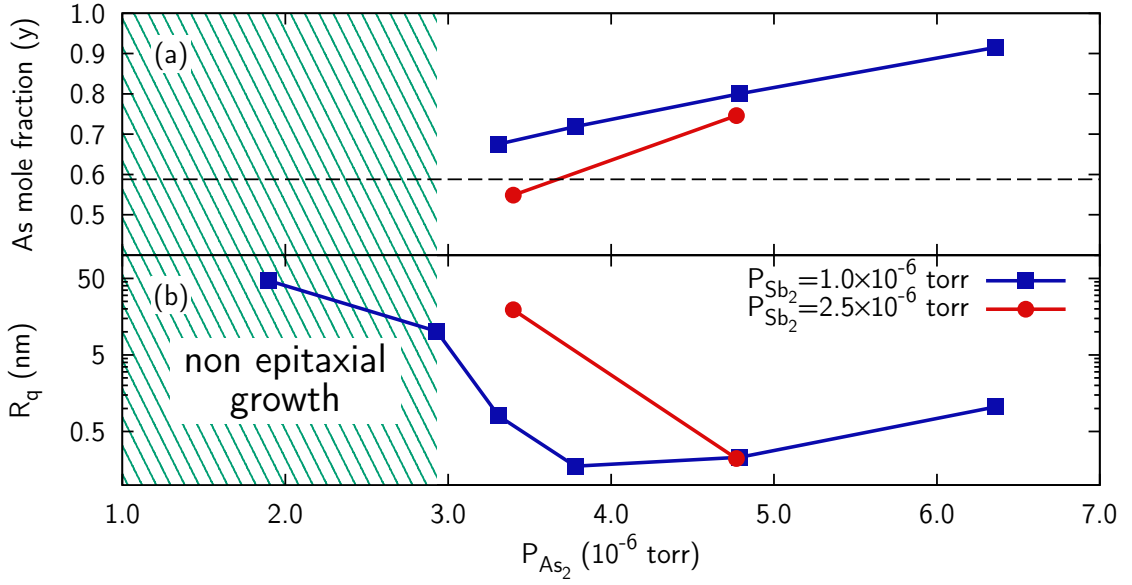


**Figure 6.12:** (a) Arsenic mole fraction and (b) root mean square surface roughness ( $R_q$ ) of  $\text{Al}_{0.462}\text{In}_{0.538}\text{As}_y\text{Sb}_{1-y}$  with respect to  $P_{\text{As}_2}$ , at two different  $P_{\text{Sb}_2}$  values and  $T_g = 445^\circ\text{C}$ . Lattice matching with InAs is indicated by the dashed line in (a). By decreasing  $P_{\text{As}_2}$ , the As fraction in the grown layer is decreased. The minimum of the surface roughness was found around  $P_{\text{As}_2} = 4 \times 10^{-6}$  torr. Below  $P_{\text{As}_2} = 3 \times 10^{-6}$  torr no epitaxial growth is possible under these conditions

$P_{\text{Sb}_2}$  ( $1 \times 10^{-6}$  torr and  $2.5 \times 10^{-6}$  torr) and the growth temperature ( $T_g = 445^\circ\text{C}$ ) were kept constant while  $P_{\text{As}_2}$  was varied. AFM measurements of these samples are shown in Figure 6.13. From Figure 6.12a it can be seen that, as expected, decreasing  $P_{\text{As}_2}$  leads to a lower As concentration ( $y$ ) in the layer. Figure 6.12b, shows that the  $P_{\text{As}_2}$  can only be adjusted within a very small range since too little  $\text{As}_2$  leads to a dramatic increase in surface roughness, due a 3-D growth mode (Figure 6.13c). This behavior is even more pronounced for samples grown at  $P_{\text{Sb}_2}$  of  $2.5 \times 10^{-6}$  torr (Figure 6.13a). When  $P_{\text{As}_2}$  is decreased below  $\sim 3 \times 10^{-6}$  torr no epitaxial growth is possible, illustrating that there is a lower limit to the  $P_{\text{As}_2}$ . This was determined by both a vanishing RHEED pattern during growth and the absence of a layer peak in the HRXRD measurement.

#### 6.5.4 SEM and EDX measurements on $\text{Al}_{0.462}\text{In}_{0.538}\text{As}_y\text{Sb}_{1-y}$ films

To understand its origin, samples showing high roughness but no cross hatch in the AFM analysis have been inspected by SEM and EDX. The micrographs of these samples are shown in Figure 6.14. Figure 6.14a shows the effect of low  $P_{\text{As}_2}$  on the surface morphology. The too low As flux on the surface leads to a lower surface mobility of the group III adatoms, breaking the layer-by-layer growth mode and resulting in a rough surface.

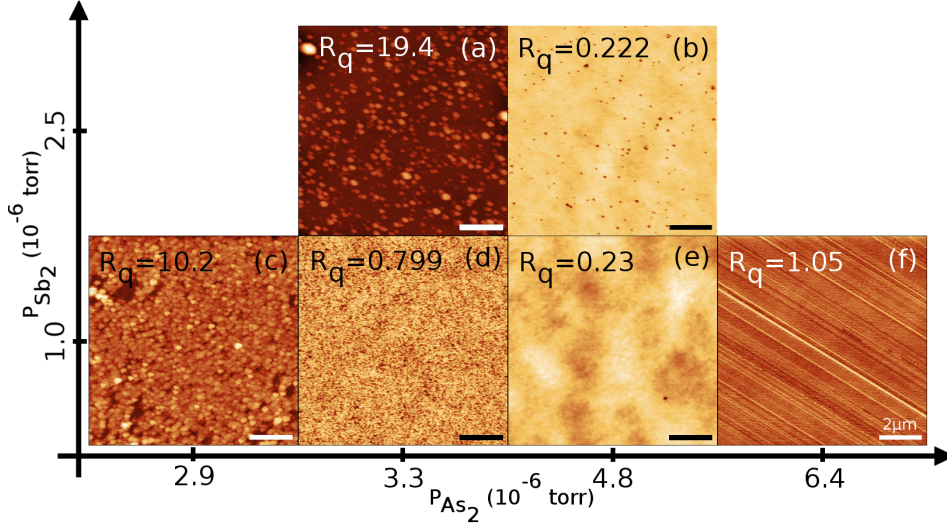


**Figure 6.13:** AFM images of samples grown at  $445^\circ\text{C}$  at  $P_{\text{Sb}_2} = 1.0 \times 10^{-6}$  torr and  $2.5 \times 10^{-6}$  torr.  $P_{\text{As}_2}$  is increased left-to-right. At both values of  $P_{\text{Sb}_2}$  smooth films were obtained at a  $P_{\text{As}_2}$  of  $4.8 \times 10^{-6}$  torr. When  $P_{\text{As}_2}$  is reduced below this value, the roughness is increased dramatically. This is even more pronounced at the higher value of  $P_{\text{Sb}_2}$ , indicating that this behavior is not caused by a too low total group V flux. It can be concluded that in absence of As, high values of  $P_{\text{Sb}_2}$  are causing the roughening of the surface. Growing  $\text{Al}_{0.462}\text{In}_{0.538}\text{As}_y\text{Sb}_{1-y}$  at  $P_{\text{Sb}_2}$  of  $1 \times 10^{-6}$  torr and  $P_{\text{As}_2}$  of  $6.4 \times 10^{-6}$  torr leads to a high lattice mismatch, which causes crosshatch and an increased surface roughness. Scale bar =  $2\mu\text{m}$ . Peak-to-valley values are: (a) 236.2 nm; (b) 6.4 nm; (c) 103.6 nm; (d) 6.9 nm; (e) 2.9 nm; (f) 13.2 nm.

EDX measurements at different spots of the sample show that the four atom species (Al, In, As, Sb) are equally distributed ( $\sigma < 0.5 \text{ at.}\%$ ). Figure 6.14b shows the effect of high  $P_{\text{Sb}_2}$  at low  $T_g$ . Similar to Figure 6.14a 3-D growth was found. Since this sample was grown with excess  $P_{\text{As}_2}$ , group V deficiency can be ruled out as the source. As for the previous sample, the EDX analysis showed that all four atom species are homogeneously distributed ( $\sigma < 0.5 \text{ at.}\%$ ). Increasing  $P_{\text{Sb}_2}$  well beyond lattice-matching seems to limit the diffusion length of the group III elements and promote a 3-D growth mode. For both sample (a) and (b) no signs of phase separation due to immiscibility were found and the 3-D morphology seems to be caused by the III/V BEP ratios.

High surface roughness was also found for the sample shown in Figure 6.14(c). Unlike for samples (a) and (b) it seems to be due to crystallites with an octagonal base that are well ordered to the substrate. The EDX measurement on this sample, shown in figure 6.15, shows that the crystallites are rich in antimony while in the surrounding area the composition is close to that found in the HRXRD study. Al and In are homogeneously distributed across the whole sample. This result suggests that  $\text{Al}_{0.462}\text{In}_{0.538}\text{As}_y\text{Sb}_{1-y}$  decomposes into  $\text{Al}_x\text{In}_{1-x}\text{As}$  and  $\text{Al}_x\text{In}_{1-x}\text{Sb}$  under these conditions.

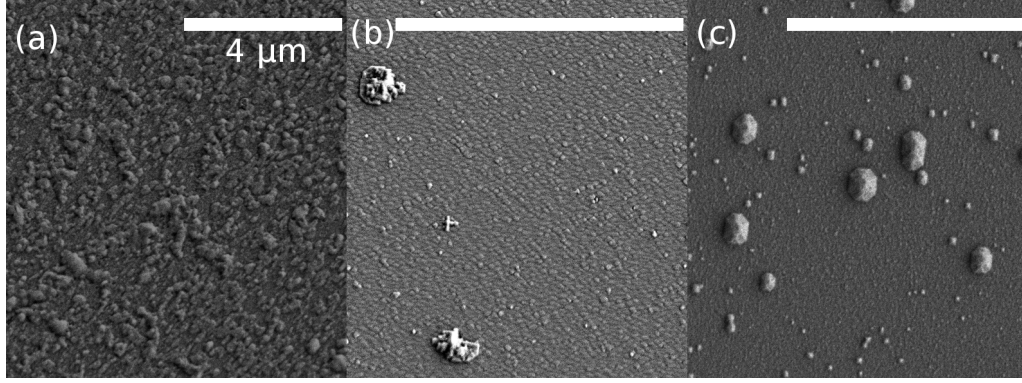
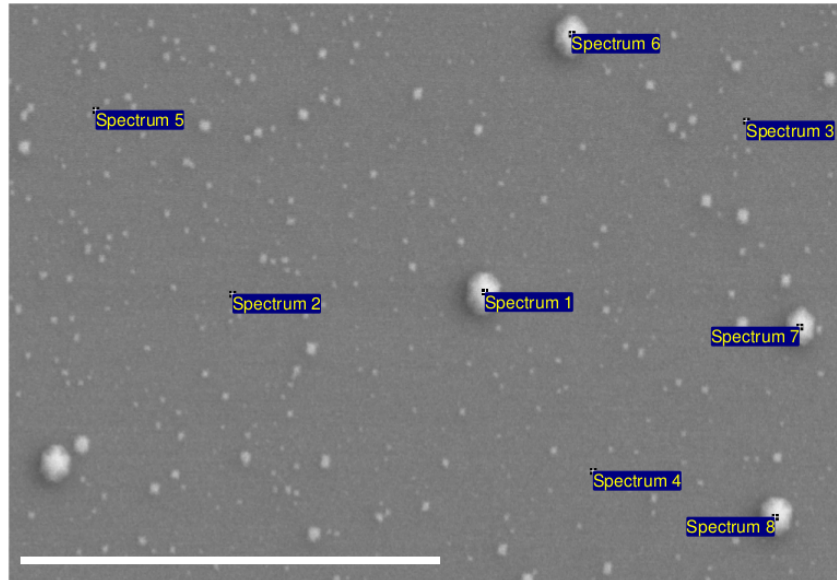


**Figure 6.14:** Samples that exhibited high surface roughness but no cross hatch in the AFM analysis have been measured by Scanning Electron Microscopy (SEM). (a) corresponds to Figure 6.13c:  $T_g = 445^\circ\text{C}$ ,  $P_{\text{As}_2} = 2.9 \times 10^{-6}$  torr,  $P_{\text{Sb}_2} = 1.0 \times 10^{-6}$  torr. 3-D island growth, caused by a low  $\text{As}_2$  coverage of the sample, was found. EDX measurements show homogeneous distributions of Al, In, As and Sb; (b) corresponds to Figure 6.10h:  $T_g = 410^\circ\text{C}$ ,  $P_{\text{As}_2} = 3 \times 10^{-6}$  torr,  $P_{\text{Sb}_2} = 2.55 \times 10^{-6}$  torr. 3-D island growth, seem to be caused by a too high  $\text{Sb}_2$  flux. Al, In, As and Sb are homogeneously distributed according to the EDX analysis; (c) corresponds to Figure 6.13a:  $T_g = 445^\circ\text{C}$ ,  $P_{\text{As}_2} = 3.3 \times 10^{-6}$  torr,  $P_{\text{Sb}_2} = 2.5 \times 10^{-6}$  torr. Octagonally shaped, well order crystallites are found on this samples. The EDX study shows that the crystallites are rich in Sb with respect to the surrounding area. Scale bar = ( $4 \mu\text{m}$ ).

In literature it usually assumed that Sb does not behave like As, which can be assumed to have a non-zero sticking coefficient only in the presence of group III atoms, and its sticking coefficient can be assumed to be independent of the group III pressures[101]. As we have seen, however, the rate of incorporation of Sb is lowered at higher  $P_{\text{Sb}_2}$ . It is therefore important to understand if the excess Sb leaves the crystal surface or if it segregates or forms clusters which deteriorate the crystal quality. An EDX study was carried out in order to determine if excess Sb can be found in the  $\text{Al}_x\text{In}_{1-x}\text{As}_y\text{Sb}_{1-y}$  layers.

Due to their high energy, incident electrons are able to travel great distances in the sample. At each encounter with an atom in the sample the incident electrons may change their trajectory which leads to a chaotic path. As shown in figure 6.16 (a), the interaction volume of the incident electrons with the sample is a pear or spherically shaped region beneath the focal point of the electron beam. Secondary electrons from a region a few 10 nm into the sample can be used for Scanning Electron Microscopy. Due to their low energy, secondary electrons from regions deeper in the sample will not escape be able to escape.

Since the size of the interaction volume can extend up to a few  $\mu\text{m}$  both the lateral as well as the depth resolution of EDX is disadvantageous for the characterization of thin films with thicknesses in the range of a few 10 nm since the signal will be a mix of the



Spectrum	Al	As	In	Sb
Spectrum 1	6.20	24.78	41.45	27.57
Spectrum 2	6.91	42.72	43.69	6.67
Spectrum 3	7.17	42.56	43.85	6.42
Spectrum 4	6.94	42.76	44.20	6.09
Spectrum 5	6.82	42.93	44.21	6.04
Spectrum 6	6.36	33.52	41.96	18.16
Spectrum 7	6.53	35.87	41.81	15.78
Spectrum 8	6.81	33.86	41.11	18.23

**Figure 6.15:** EDX measurements performed on and off of the octagonally shaped crystallites. Measurements performed on the crystallites show a higher concentration of Sb than those performed in between the crystallites. This measurement lets us conclude that the  $\text{Al}_x\text{In}_{1-x}\text{As}_y\text{Sb}_{1-y}$  is decomposing into  $\text{Al}_x\text{In}_{1-x}\text{As}$  and  $\text{AlAs}_{1-x}\text{Sb}_x$  under these conditions. Scale bar =  $6.0\text{ }\mu\text{m}$ .

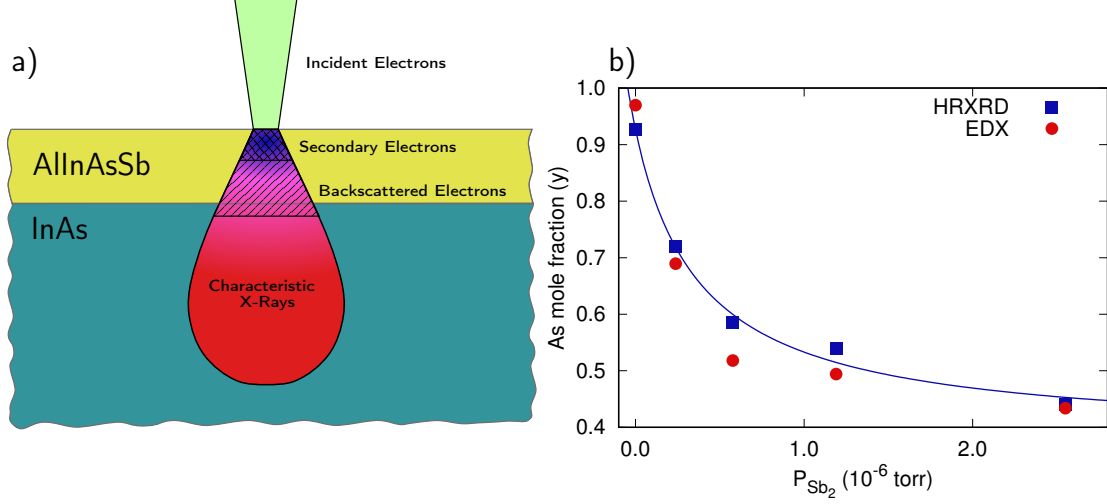


**Figure 6.16:** (a) EDX interaction volume and (b) comparison of the composition acquired by EDX and HRXRD. Due to the large interaction penetration depth of the incident electrons the EDX signal is a mix of the compositions of the  $\text{Al}_{0.462}\text{In}_{0.538}\text{As}_y\text{Sb}_{1-y}$  layer and the  $\text{InAs}$  substrate. The As content of the  $\text{Al}_{0.462}\text{In}_{0.538}\text{As}_y\text{Sb}_{1-y}$  layer can be calculated when the Al to In ratio is known. (b) shows that the compositions obtained from EDX and HRXRD match sufficiently. It can be concluded that no excess Sb is in the  $\text{Al}_{0.462}\text{In}_{0.538}\text{As}_y\text{Sb}_{1-y}$  layer.

composition of the  $\text{Al}_x\text{In}_{1-x}\text{As}_y\text{Sb}_{1-y}$  layer and the  $\text{InAs}$  substrate.

For  $\text{Al}_x\text{In}_{1-x}\text{As}_y\text{Sb}_{1-y}$ , however, the As mole fraction can be calculated if the ratio between Al and In in the layer is known. Since this ratio is given by the ratio of the growth rates the As mole fraction ( $y$ ) can be calculated by

$$y = 1 - \frac{Sb_{\text{edx}}}{Al_{\text{edx}} \left( 1 + \frac{Gr_{\text{In}}}{Gr_{\text{Al}}} \right)}. \quad (6.9)$$

Figure 6.16 (b) shows a comparison between the composition obtained by HRXRD and EDX. Although EDX is not the optimal method to determine the composition of such thin films, both results are close enough to each other that we can conclude that no excess Sb remains in the layer.

## 6.6 Discussion

A summary of all samples used in this study that have been grown at  $T_g=445^\circ\text{C}$  (a) and  $410^\circ\text{C}$  (b) is given in Figure 6.17. In both cases, a large  $P_{\text{As}_2}/P_{\text{Sb}_2}$  ratio leads to cross hatch, due to a large lattice mismatch. For a  $T_g$  of  $445^\circ\text{C}$ , a  $P_{\text{As}_2}$  below  $3.3 \times 10^{-6}$  torr leads to a rough surface. Roughening was also found for samples grown at a  $T_g$  of

## 6.6. Discussion

---

410 °C for the highest  $P_{\text{Sb}_2}$  of  $2.5 \times 10^{-6}$  torr. While partial relaxation was found in the reciprocal space map around the InAs (224), the roughening seems to be mainly caused by the high  $P_{\text{Sb}_2}$  since no sign of cross hatch was found in either EDX or AFM measurements. Growing at higher  $P_{\text{Sb}_2}$  at a  $T_g$  of 445 °C results in lower film quality, due to the formation of ordered crystallites with an octagonal base. Since these crystallites were found to be rich in Sb in the EDXEDX analysis, it appears that decomposition, probably due to the miscibility gap of the material occurs under these conditions. A first order approximation, shown as the gray shaded area in Figure 6.17, was used to locate the region of pressures for which lattice matching can be expected. At a  $T_g$  of 445 °C this region is close, if not within, the region which leads to decomposition and the formation of Sb rich crystallites. At a  $T_g$  of 410 °C the region at which lattice matching is expected is far below the region for which the roughening due to high  $P_{\text{Sb}_2}$  is observed and the growth of lattice-matched high quality material is easily achieved.

The data presented in this study suggests that a  $T_g$  of 445 °C is the upper limit for lattice matched growth of  $\text{Al}_{0.462}\text{In}_{0.538}\text{As}_y\text{Sb}_{1-y}$ . For a stable growth and high quality material, however, it is advised to use even lower  $T_g$ . This is even more critical if the conditions for high-quality InAs and  $\text{Al}_{0.462}\text{In}_{0.538}\text{As}_y\text{Sb}_{1-y}$  have to be met simultaneously.

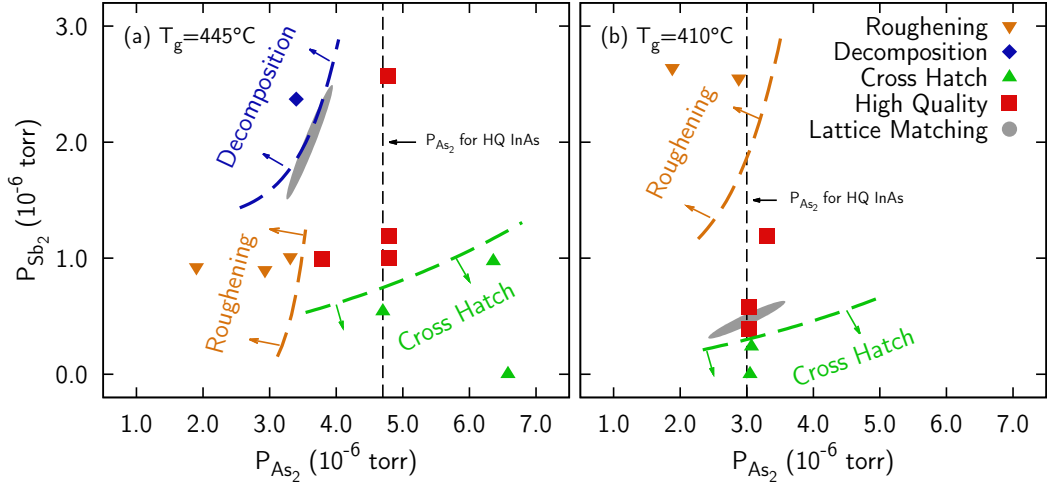


**Figure 6.17:** Summary of all samples used in this study that have been grown at  $T_g = 445^\circ\text{C}$  (a) and  $410^\circ\text{C}$  (b). At both  $T_g$ , high  $P_{\text{As}_2}/P_{\text{Sb}_2}$  ratios lead to cross hatch due to a large lattice mismatch. For a  $T_g$  of  $445^\circ\text{C}$ ,  $P_{\text{As}_2}$  below  $3.3 \times 10^{-6}$  torr leads to a rough surface. Growth performed at high  $P_{\text{Sb}_2}$  leads to the formation of crystallites which suggest that the material is decomposing due to the miscibility gap. At higher values of  $P_{\text{As}_2}$  high quality material is grown. At this  $T_g$  the region in which lattice matching can be achieved is close to the region for which the formation of crystallites is observed. Samples grown at a  $T_g$  of  $410^\circ\text{C}$  show roughening of the surface at high  $P_{\text{Sb}_2}$ . At this  $T_g$  the region in which lattice matching is possible is far away from the region in which surface roughening was found.





---

## GaAsSb as a Model System for Group V mixing

---

We have seen that the growth of III/V semiconductors in which As and Sb are mixed is non trivial in MBE and extensive tuning of the growth parameters is necessary in order to achieve high-quality material.  $\text{GaAs}_{1-x}\text{Sb}_x$  is an interesting material to study the incorporation of As and Sb since only one group III material is present in this alloy and thus the mixing of the two group V elements can be examined separately. Moreover, the crystal quality with respect to growth parameters like  $T_g$ , III/V ratio and V/V ratio can be examined without the necessity to also control a III/III ratio. This limits the room for interpretations and facilitates the collection of reliable data. Furthermore,  $\text{Ga}_{0.47}\text{In}_{0.53}\text{As}/\text{GaAs}_{0.51}\text{Sb}_{0.49}$  based structures are interesting for many different fields of research like MIR-devices[102, 103, 104, 105], THz-QCLs[106, 53, 107], resonant tunneling diodes[108, 109, 110] where enhanced crystal quality may lead to higher performance as well as basic material characterization[111, 112]. Figure 7.1 shows an overview of the InP family, i.e. III/V semiconductors which can be grown lattice-matched to InP.

### 7.1 The $\text{Ga}_{0.47}\text{In}_{0.53}\text{As}/\text{GaAs}_{0.51}\text{Sb}_{0.49}$ material system

$\text{Ga}_x\text{In}_{1-x}\text{As}$  and  $\text{GaAs}_{1-x}\text{Sb}_x$  lattice matched to InP form a material system which shows promising properties for THz-QCLs. The low effective electron mass in the well ( $\text{Ga}_{0.47}\text{In}_{0.53}\text{As}$ ) of  $0.043m_e$ [113] can provide higher gain in these structures while the low effective electron mass in the barrier ( $\text{GaAs}_{0.51}\text{Sb}_{0.49}$ ) of  $0.045m_e$ [114] allows the use of thicker barriers for THz-QCL structures which are easier to control in terms of growth.

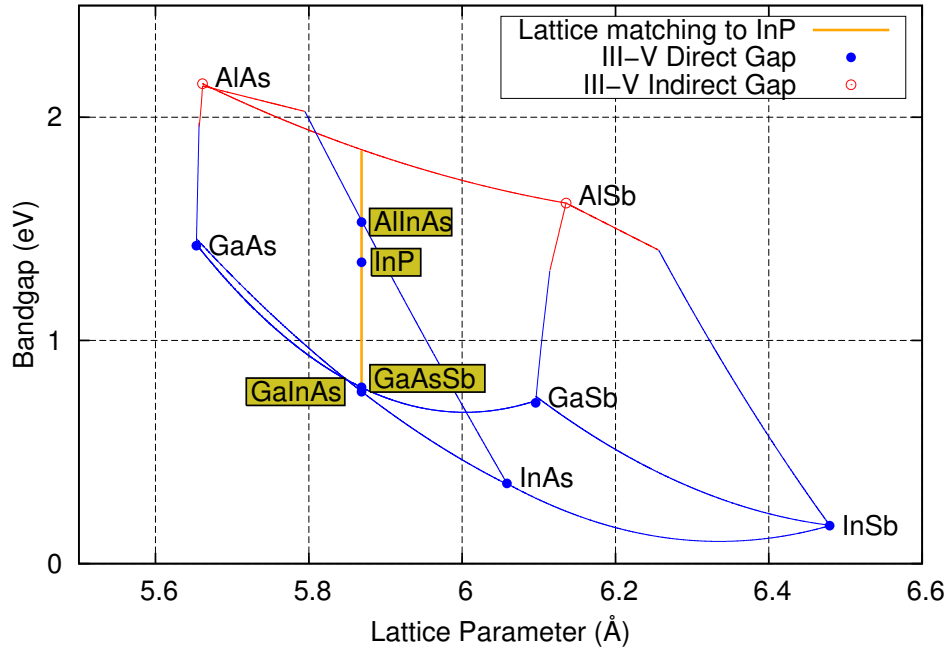


**Figure 7.1:** Band Gap versus lattice constant of III/V semiconductors. Direct band gap semiconductors are displayed in blue, indirect band gap semiconductors are shown in red. Ternary alloys are indicated by the curves connecting the binary components. The ternary alloys  $\text{Ga}_x\text{In}_{1-x}\text{As}$ ,  $\text{Al}_x\text{In}_{1-x}\text{As}$  and  $\text{GaAs}_{1-x}\text{Sb}_x$  which can be grown lattice matched to InP are highlighted.

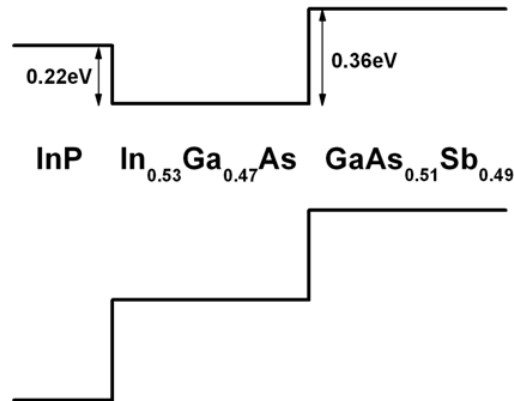


**Figure 7.2:** Band alignment of the  $\text{Ga}_{0.47}\text{In}_{0.53}\text{As}/\text{GaAs}_{0.51}\text{Sb}_{0.49}/\text{InP}$  material system.  $\text{Ga}_{0.47}\text{In}_{0.53}\text{As}$  and  $\text{GaAs}_{0.51}\text{Sb}_{0.49}$  show a type two band alignment with a conduction band offset of 360 meV. The large band gap of InP allows for the fabrication of dielectric waveguides for MIR applications.

## 7.2. Crystal Quality of $\text{GaAs}_{1-x}\text{Sb}_x$ with Respect to the Substrate Temperature

The materials shows a type II band alignment, i.e. the conduction band maximum is one material while the valence band minimum is in the other material, and a conduction band offset of 360 meV, which is high enough to allow for the design of MID-infrared lasers but also not too high to design excellent THz-QCL structures. InP can be used to create efficient dielectric waveguides for MID-infrared devices made from this material system, since it allows for good confinement of the optical modes. The band alignment of this material system is shown in figure 7.2

In terms of maximum operation temperature, THz-QCLs made from this material are on par with the much more mature  $\text{Ga}_{0.47}\text{In}_{0.53}\text{As}/\text{Al}_{0.48}\text{In}_{0.52}\text{As}$  material system, and it can be expected that enhanced growth methods will enable it to outperform this material system in the future. Table 7.1 shows a comparison of the maximum operation temperatures of THz-QCLs made from different material systems.

Material System	Conduction Band Offset	Thinnest Layer	$T_{\max}$ (THz QCL)
$\text{GaAs}/\text{Al}_{0.15}\text{Ga}_{0.85}\text{As}$	120 meV	2 nm	199.5 K (Waterloo[43])
$\text{In}_{0.53}\text{Ga}_{0.47}\text{As}/\text{GaAs}_{0.51}\text{Sb}_{0.49}$	360 meV	1 nm	142 K (TU-Wien[54])
$\text{In}_{0.53}\text{Ga}_{0.47}\text{As}/\text{In}_{0.53}\text{Al}_{0.47}\text{As}$	520 meV	0.3 nm	145 K (TU-Wien)

**Table 7.1:** Comparison of maximum operation temperatures of different THz-QCLs materials. In terms of maximum operation temperature, THz-QCLs produced from the  $\text{Ga}_{0.47}\text{In}_{0.53}\text{As}/\text{GaAs}_{0.51}\text{Sb}_{0.49}$  material system is on par with devices produced from  $\text{Ga}_{0.47}\text{In}_{0.53}\text{As}/\text{Al}_{0.48}\text{In}_{0.52}\text{As}$ . Due to the lower effective mass in the barrier material and the lower conduction band offset, much thicker barrier layers can be grown for similar structures which is a clear advantage in terms of growth control.

## 7.2 Crystal Quality of $\text{GaAs}_{1-x}\text{Sb}_x$ with Respect to the Substrate Temperature

We have seen in section 6 that the substrate temperature has a strong influence on the crystal quality of  $\text{Al}_x\text{In}_{1-x}\text{As}_y\text{Sb}_{1-y}$ . Since in  $\text{GaAs}_{1-x}\text{Sb}_x$  the same group V metals are mixed we can expect a similar behavior for this material.

To evaluate the influence of the growth temperature on the quality of the grown material, a set of samples has been grown at substrate temperatures of 480 °C to 400 °C and examined by HRXRD. Figure 7.3 (a-d) show reciprocal space maps around the InAs (004) diffraction peak. The scans are aligned on the InAs peak and the peaks originating from the  $\text{GaAs}_{1-x}\text{Sb}_x$  layers are highlighted by the red box. The third peak in each scan originates from the  $\text{Ga}_x\text{In}_{1-x}\text{As}$  buffer layer. The shifting of the position of this layer in

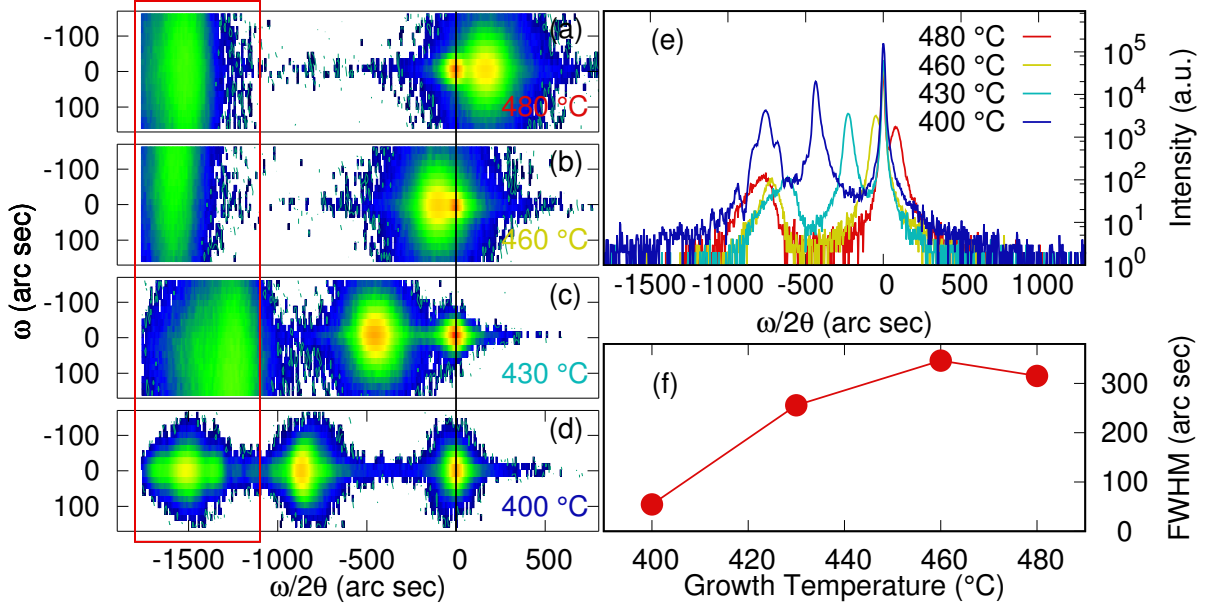


**Figure 7.3:** Rocking curve broadening of the  $\text{GaAs}_{1-x}\text{Sb}_x$  layer peak versus temperature. The full width at half maximum (FWHM) of the  $\text{GaAs}_{1-x}\text{Sb}_x$  peak drop from over 300 arcsec to a few 10 arcsec when the  $T_g$  is lowered from 480 °C to 400 °C. This indicated a strong increase in the layer quality at lower growth temperatures.

the different samples can be explained by a slow depletion of the Ga cell throughout the experiment. However, relaxation of this layer can be ruled out, since the composition of the buffer layer is close enough to the lattice matched composition at the given layer thickness. Although it is evident that the Ga flux changed during the experiment, the change is on the order of 10 % and can be neglected.

It can clearly be seen that temperatures of 430 °C and above lead to significant peak broadening in the  $\omega$ -direction which shows the presence of a high density of dislocations and mosaic spread which are clear indications of inaccurate growth conditions. Figure 7.3(e) supports this observation. Here we see the direct comparison of coupled  $\omega/2\theta$  scans performed on the same samples. The peak broadening, for samples grown at 430 °C and above, can also be clearly seen in these scans. Moreover, we find a two orders of magnitude higher peak intensity for the low temperature sample and the onset of Pendelösung fringes which both indicates high crystal quality. These findings are summarized in figure 7.3(f) which shows the FWHM of the  $\text{GaAs}_{1-x}\text{Sb}_x$  peak in omega direction. We can see a clear trend to a lower peak width, and hence, higher crystal quality at lower substrate temperatures.

An interesting side effect of a low substrate temperature can be seen when we look at the homogeneity of the composition of the  $\text{GaAs}_{1-x}\text{Sb}_x$  layer between the center and the edge of the sample. Figures 7.4(a-d) show the coupled  $\omega/2\theta$  scans of samples grown at

## 7.2. Crystal Quality of $\text{GaAs}_{1-x}\text{Sb}_x$ with Respect to the Substrate Temperature

substrate temperatures from 480 °C to 400 °C. For the sample grown at 480 °C we find a peak shift of almost 250 arcsec which corresponds to a shift in composition from 46.7 % to 43.1 % over a distance of about 16 mm. Between 460 °C and 430 °C the peak shift drops down to  $\sim 50$  arcsec and it vanishes at a  $T_g$  of 400 °C.

The observed shift in the  $\text{GaAs}_{1-x}\text{Sb}_x$  composition can not be related to the geometry of the MBE system since, 1) all cells in the MBE system have the same distance and are under the same angle to the substrate, and 2) a composition shift would have to be found for the  $\text{Ga}_x\text{In}_{1-x}\text{As}$  layers as well. Consequently, the shift is attributed to the temperature distribution on the wafer and the temperature dependent incorporation of Sb into  $\text{GaAs}_{1-x}\text{Sb}_x$ .

It is evident that such a strong shift in composition is a drawback for reliable production of  $\text{GaAs}_{1-x}\text{Sb}_x$  based devices and hence, also from the perspective of homogeneity low-temperature growth of this material is favorable.

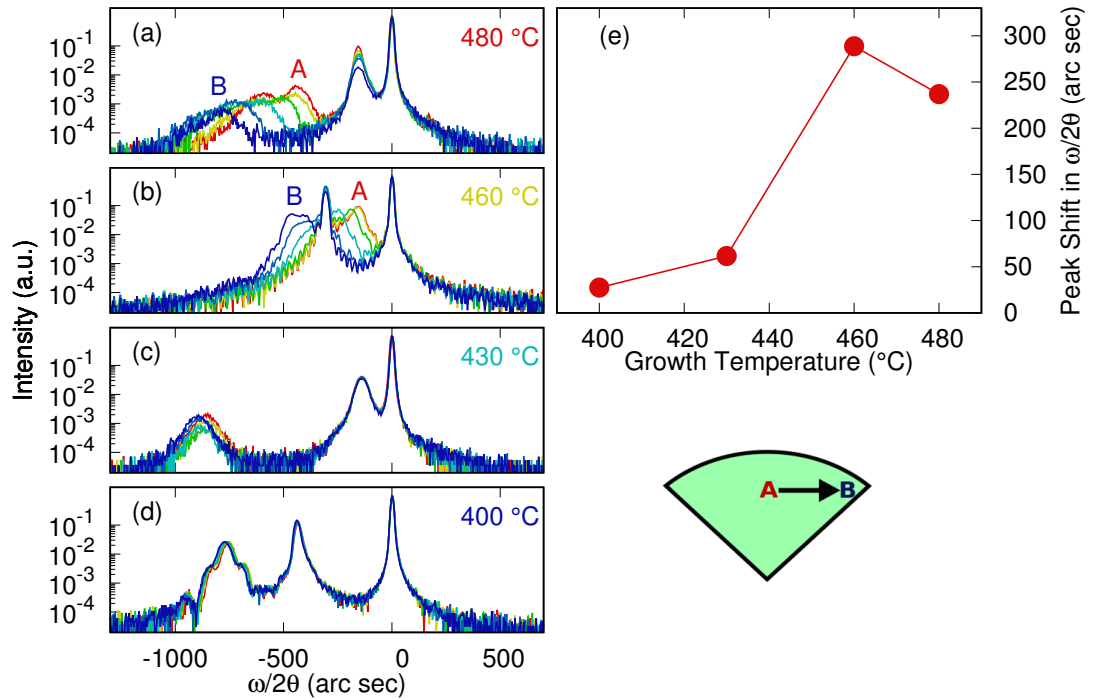


**Figure 7.4:** Distribution of the composition across a quarter wafer. The composition of the  $\text{GaAs}_{1-x}\text{Sb}_x$  layer is measured in six steps from the center to the edge of the wafer. At a  $T_g$  of 480 °C layer peak shifts  $\sim 250$  arcsec over a distance of  $\sim 16$  mm. This corresponds to a change in the As mole fraction from 46.7 % to 43.1 %. The peak shift is greatly reduced when the  $T_g$  is lowered and is negligible at  $T_g$  below 430 °C.

## 7.3 Incorporation of Sb into GaAs<sub>1-x</sub>Sb<sub>x</sub>

This section is based on Ref [115].

The search for concepts which allow for higher performance of these devices shifts the focus of the research towards low effective electron mass well materials like Ga<sub>x</sub>In<sub>1-x</sub>As[53, 103] and InAs[116, 117, 118, 119], and thus compounds containing Sb, like GaAs<sub>1-x</sub>Sb<sub>x</sub> or Al<sub>x</sub>In<sub>1-x</sub>As<sub>y</sub>Sb<sub>1-y</sub>[89], become more and more interesting as barrier materials. The growth of high quality layers of these materials, however, is still challenging since the presence of two group V species creates a non-trivial growth environment. GaAs<sub>1-x</sub>Sb<sub>x</sub> is an ideal material to study the interaction between As and Sb, since the presence of only one group III material limits the space for interpretations of the experimental results. MBE growth of GaAs<sub>1-x</sub>Sb<sub>x</sub> was first demonstrated by Chang et. al. in 1977[120]. Nakata and coworkers[121] have grown high quality layers of GaAs<sub>1-x</sub>Sb<sub>x</sub> using As<sub>4</sub> and Sb<sub>4</sub> at substrate temperatures between 470 °C and 490 °C and a growth rate of 1.3 μm h<sup>-1</sup>. Since then, numerous publications were devoted to understanding the incorporation of As and Sb into this alloy.

The inverse relation between the growth temperature ( $T_g$ ) and the incorporation of Sb into GaAs<sub>1-x</sub>Sb<sub>x</sub> was first demonstrated by Klem et. al.[122] and is generally agreed on in literature. The role of the growth rate, however, is still subject to debate. Al-muneau et. al. reported on the incorporation of Sb into GaAs<sub>1-x</sub>Sb<sub>x</sub>, AlAs<sub>1-x</sub>Sb<sub>x</sub> and Al<sub>x</sub>Ga<sub>1-x</sub>As<sub>y</sub>Sb<sub>1-y</sub>[123]. For all three alloys, a linear relation between the Sb flux, normalized by the total flux of the group III elements, and the Sb mole fraction in the layer was found. From these results, it was concluded that the incorporation of Sb has to be close to unity. Similarly, Semenov et. al. found an increasing As mole fraction in GaAs<sub>1-x</sub>Sb<sub>x</sub> and Al<sub>x</sub>Ga<sub>1-x</sub>As<sub>y</sub>Sb<sub>1-y</sub> alloys for increasing group III fluxes and constant group V fluxes[124]. This is attributed to the fact that higher growth rates will lead to a shortage of Sb and unoccupied lattice sites will be filled by excess As.

On the other hand, the reverse has also been stated by other authors. An inverse relation between the As mole fraction in GaAs<sub>1-x</sub>Sb<sub>x</sub> layers and the arrival rate of Ga atoms was first reported by Klem et. al. in 1987[125], i.e. higher  $P_{Ga}$  results in higher Sb incorporation. The same effect has been observed by Bosacchi and coworkers[126] for GaAs<sub>1-x</sub>Sb<sub>x</sub> layers grown on GaAs substrates. The authors concluded that the incorporation of Sb into GaAs<sub>1-x</sub>Sb<sub>x</sub> is more effective at higher growth rates since the availability of Ga sites on the growing surface promotes the dissociation of the Sb species. Sun and coworkers[127] grew layers of GaAs<sub>1-x</sub>Sb<sub>x</sub> on GaAs at growth rates between 0.2 ML s<sup>-1</sup> and 0.9 ML s<sup>-1</sup>. At growth rates above 0.8 ML s<sup>-1</sup> the authors find a saturation of the

Sb mole fraction, and hence, conclude that the growth rate dependence of the composition can be eliminated if the growth is performed at the higher growth rates. The authors assume that high growth rates, and hence, availability of Ga sites, prevents the desorption of Sb which leads to an increase in the incorporation efficiency. Selvig et. al. analyzed GaAs<sub>1-x</sub>Sb<sub>x</sub> and Al<sub>x</sub>Ga<sub>1-x</sub>As<sub>y</sub>Sb<sub>1-y</sub> layers with Sb mole fractions up to 0.2, grown on GaSb substrates[128]. It was found that the incorporation of Sb is decreased at the lower growth rate. The authors conclude that the lower Sb composition which is found if the GaAs<sub>1-x</sub>Sb<sub>x</sub> layer is grown at the lower growth rate is due to an As-for-Sb exchange reaction which happens at the growing surface.

We can see that the reports on the growth of GaAs<sub>1-x</sub>Sb<sub>x</sub> by MBE strongly disagree on the incorporation behavior of Sb. While some authors find an increase in the Sb mole fraction with the growth rate, others find the opposite behavior. Moreover, the authors reporting to find an increase of the Sb mole fraction with the growth rate present very different explanations for this effect. Hence, an in depth study of the effect of the growth rate on the composition of GaAs<sub>1-x</sub>Sb<sub>x</sub> is necessary in order to understand the mechanisms that define the final layer composition.

In order to investigate the incorporation of Sb into GaAs<sub>1-x</sub>Sb<sub>x</sub>, a set of samples was grown in a Riber Compact 21 MBE system on free-standing n+ InP (001) wafers. Within this set, the growth rate ( $R_{GaAsSb}$ ) was varied between 0.195 ML s<sup>-1</sup> and 1.56 ML s<sup>-1</sup>. The range of P<sub>Sb<sub>2</sub></sub> was between  $5 \times 10^{-7}$  torr and  $1.0 \times 10^{-6}$  torr, a P<sub>As<sub>2</sub></sub> between  $2.8 \times 10^{-6}$  torr and  $1.1 \times 10^{-5}$  torr was used, and the T<sub>g</sub> was varied from 400 °C to 460 °C. All pressures in this work are given as absolute values without correction for the specific molecular species. For the group V materials, valved cracking cells were used with the cracking zone temperatures set to 850 °C and 1000 °C to produce As<sub>2</sub> and Sb<sub>2</sub> respectively. For all samples, first the oxide was thermally desorbed under P<sub>As<sub>2</sub></sub> of  $1.1 \times 10^{-5}$  torr at 520 °C. The temperature was then reduced to the growth temperature where a 50 nm thick Ga<sub>0.47</sub>In<sub>0.53</sub>As buffer layer and a 400 nm thick GaAs<sub>1-x</sub>Sb<sub>x</sub> layer were grown. All samples were measured with HRXRD to determine their crystal quality and composition.

### 7.3.1 Growth rate dependence of the Sb incorporation

To understand the influence of the growth rate on the composition of GaAs<sub>1-x</sub>Sb<sub>x</sub>, four sets of samples have been grown at a T<sub>g</sub> of 400 °C and 460 °C. For each set, T<sub>g</sub>, P<sub>As<sub>2</sub></sub> and P<sub>Sb<sub>2</sub></sub> were kept constant, while the  $R_{GaAsSb}$  was varied. The results are given in figure 7.5. All samples show a decrease in the As mole fraction with increasing  $R_{GaAsSb}$  on the low growth rate side ( $R_{GaAsSb}$  between 0 ML s<sup>-1</sup> and  $0.5 \times 10^{-6}$  ML s<sup>-1</sup>), which is in

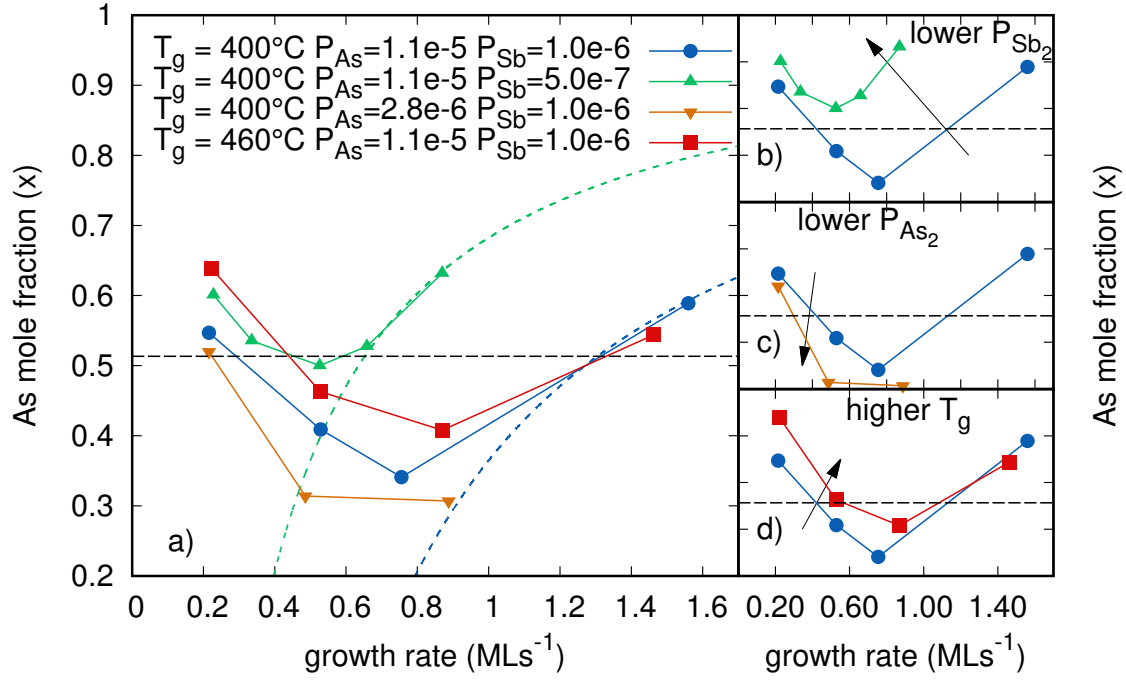


**Figure 7.5:** (a) Composition of  $\text{GaAs}_{1-x}\text{Sb}_x$  over the growth rate  $R_{\text{GaAsSb}}$  at different  $P_{\text{As}_2}$ ,  $P_{\text{Sb}_2}$  and  $T_g$ . On the high growth rate side the As mole fraction rises with the growth rate since for each curve the  $P_{\text{Sb}_2}$  is constant and hence the ratio  $\frac{P_{\text{Sb}_2}}{P_{\text{Ga}}}$  is decreasing. The dashed lines indicate a fit to  $1 - C \frac{P_{\text{Sb}_2}}{P_{\text{Ga}}}$  via  $C$ . On the low growth rate side the As mole fraction is rising with the falling growth rate. Supplying less  $\text{Sb}_2$  (b) leads to a higher As mole fraction. Supplying less  $\text{As}_2$  (c) leads to a lower As mole fraction in the  $\text{GaAs}_{1-x}\text{Sb}_x$  layer. On the high growth rate side, samples grown at a  $T_g$  of  $400^\circ\text{C}$  and  $460^\circ\text{C}$  (d) show an almost identical behavior. On the low growth rate side, the incorporation of Sb into  $\text{GaAs}_{1-x}\text{Sb}_x$  is strongly decreased at the higher temperature.

agreement with refs. [125, 126, 127, 128]. On the high growth rate side, however, the As mole fraction is increasing with rising  $R_{\text{GaAsSb}}$  as reported in refs. [123, 124]. Depending on the actual set of parameters chosen in each of these publications, the authors only saw either the low or the high growth rate side which resulted in the discrepancy in their reports.

In order to gain further insight, samples were grown at different values for  $T_g$ ,  $P_{\text{As}_2}$  and  $P_{\text{Sb}_2}$ . We find that a decrease of  $P_{\text{Sb}_2}$ , under otherwise identical conditions, leads to a shift of the measured compositions in the  $\text{GaAs}_{1-x}\text{Sb}_x$  layers towards higher As mole fractions (figure 7.5 (b)). While this seems to be an obvious result, it should be noted that the effect is much more dramatic on the high growth rate side of the experiment, than on the low growth rate side.



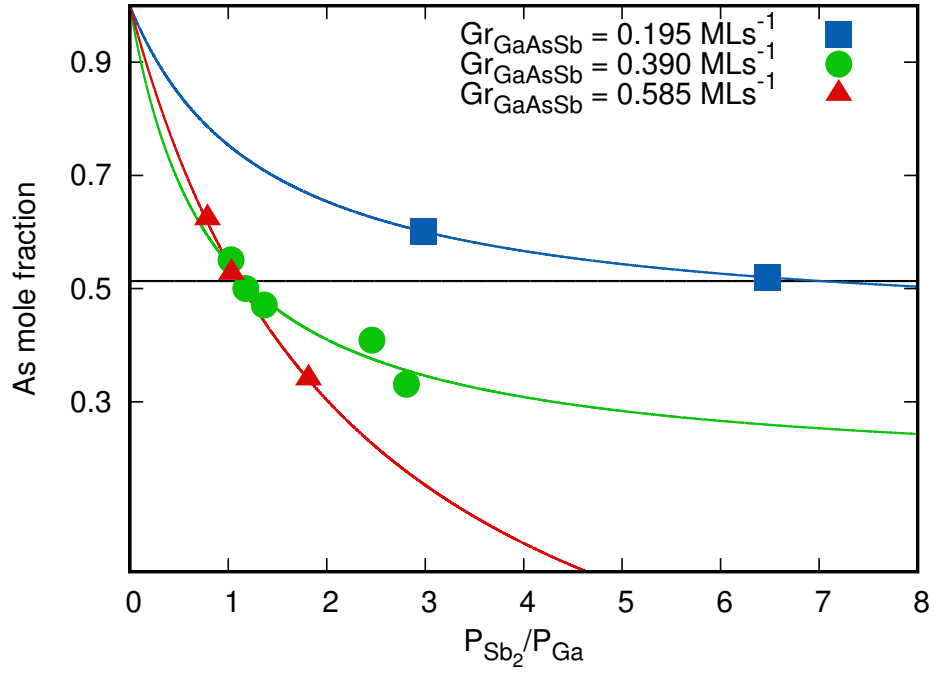


**Figure 7.6:** As mole fraction with respect to the  $\frac{P_{Sb_2}}{P_{Ga}}$  ratio at different growth rates. At the lowest growth rate a  $\frac{P_{Sb_2}}{P_{Ga}}$  ratio of 6 is necessary to achieve lattice matching with InP. For the higher growth rates the incorporation efficiency is greatly enhanced and only a  $\frac{P_{Sb_2}}{P_{Ga}}$  ratio of  $\sim 1.5$  is necessary.

If we assume a temperature dependent but otherwise constant incorporation coefficient for Sb, as described in refs. [123, 124], the arsenic mole fraction should be given by

$$x = 1 - C_{Sb} \frac{\Phi_{Sb}}{\Phi_{Ga}} \quad (7.1)$$

for  $C_{Sb}\Phi_{Sb} < \Phi_{Ga}$ , and

$$x = 0 \quad (7.2)$$

for  $C_{Sb}\Phi_{Sb} \geq \Phi_{Ga}$ . Since  $\Phi_{Ga} \propto P_{Ga}$ , for fixed  $P_{As_2}$  and  $P_{Sb_2}$ , the arsenic mole fraction should be a monotonically rising function

$$x = 1 - C \frac{P_{Sb_2}}{P_{Ga}}, \quad (7.3)$$

with  $C$  being constant for a given  $T_g$ . On the high growth rate side, the compositions of the GaAs<sub>1-x</sub>Sb<sub>x</sub> layers approach this trend, as indicated by the dashed lines in figure 7.5 (a).

### 7.3. Incorporation of Sb into GaAs<sub>1-x</sub>Sb<sub>x</sub>

---

We can conclude that the composition at high growth rates is strongly dependent on the arrival rate of Sb<sub>2</sub> molecules, while a different effect limits the incorporation of Sb into the GaAs<sub>1-x</sub>Sb<sub>x</sub> layer at the low growth rates.

A drastic decrease of the  $P_{As_2}$  shifts the curve even further towards lower As mole fractions. Especially on the low growth rate side we see that competition between As and Sb strongly influence the final composition of the GaAs<sub>1-x</sub>Sb<sub>x</sub> layers.

The change in the incorporation efficiency of Sb into GaAs<sub>1-x</sub>Sb<sub>x</sub> with respect to the growth rate can clearly be observed if we plot the composition over the  $\frac{P_{Sb_2}}{P_{Ga}}$  ratio for fixed growth rates. Figure 7.6 shows the as mole fraction for growth rates between 0.195 ML s<sup>-1</sup> and 0.585 ML s<sup>-1</sup>. We can see that, at a growth rate of 0.195 ML s<sup>-1</sup>, a  $\frac{P_{Sb_2}}{P_{Ga}}$  ratio of just over 6 is required to achieve lattice matching with InP. At growth rates of 0.390 ML s<sup>-1</sup> and 0.585 ML s<sup>-1</sup> a  $\frac{P_{Sb_2}}{P_{Ga}}$  ratio of roughly 1.5 is sufficient. Moreover, the highest growth rate shows the steepest decrease in the As mole fraction with rising  $P_{Sb_2}$ .

The fourfold increase in the incorporation efficiency clearly shows the importance of the growth rate as a growth parameter for the growth of GaAs<sub>1-x</sub>Sb<sub>x</sub>.

#### 7.3.2 Temperature dependence of the Sb incorporation

In the previous sections we have seen that the crystal quality of GaAs<sub>1-x</sub>Sb<sub>x</sub> as well as the incorporation of Sb into GaAs<sub>1-x</sub>Sb<sub>x</sub> are strongly temperature dependent. Numerous authors studied the influence of the  $T_g$ . We have seen how the growth rate and the fluxes of the source materials influence the incorporation of Sb into GaAs<sub>1-x</sub>Sb<sub>x</sub>. In the following experiment we will see the influence of the  $T_g$  on the incorporation. The samples were grown at growth rates between 0.195 ML s<sup>-1</sup> and 0.780 ML s<sup>-1</sup> at  $T_g$  of 400 °C and 460 °C,  $P_{As_2}$  of  $1.1 \times 10^{-5}$  torr and  $P_{Sb_2}$  of  $1.0 \times 10^{-6}$  torr. The results are shown in figure 7.5(d). We can see that there is an almost perfect overlap with the samples grown at  $T_g$  of 400 °C on the high growth rate side. This indicates that the sticking of Sb does not depend on  $T_g$  in this temperature range, and that this slope is solely dependent on the  $\frac{P_{Sb_2}}{P_{Ga}}$  fraction. On the low growth rate side, however, we see a strong increase in the As mole fraction at the higher  $T_g$ . The experiment, however, shows a rise in the As mole fraction with rising  $T_g$ . This indicates that the lower incorporation efficiency of Sb is due to a process which happens at an increasing rate at elevated temperatures.

#### 7.3.3 Crystal quality with respect to the growth rate

In addition to the composition of the GaAs<sub>1-x</sub>Sb<sub>x</sub> layers, their crystal quality might give a hint on the incorporation of Sb. In order to understand the influence of the growth rate

on the crystal quality, samples grown at different growth rates but similar compositions were examined by HRXRD.

A comparison of the crystal quality of GaAs<sub>1-x</sub>Sb<sub>x</sub> layers grown at 0.227 ML s<sup>-1</sup> and at 0.870 ML s<sup>-1</sup> is shown in figure 7.7. Subfigure (a) shows the rocking curve scans of the two layers. The sample grown at the lower growth rate shows a FWHM of 258 arcsec while the peak corresponding to the layer grown at the high growth rate shows a FWHM of only 36 arcsec. HRXRD Reciprocal Space Maps (RSMs) around the InP (224) diffraction peaks of the two layers are shown in subfigures (b) and (c). The in-plane lattice constant measured for the layer grown at the low growth rate deviates from that of the InP substrate, indicating partial relaxation. Using the measured in-plane and out-of-plane lattice constants and using the stiffness components given in ref [31], a relaxation of 25 % was calculated. The layer, grown at the higher growth rate (subfigure (c)) shows no deviation in the in-plane lattice constant and hence can be assumed to be fully strained.

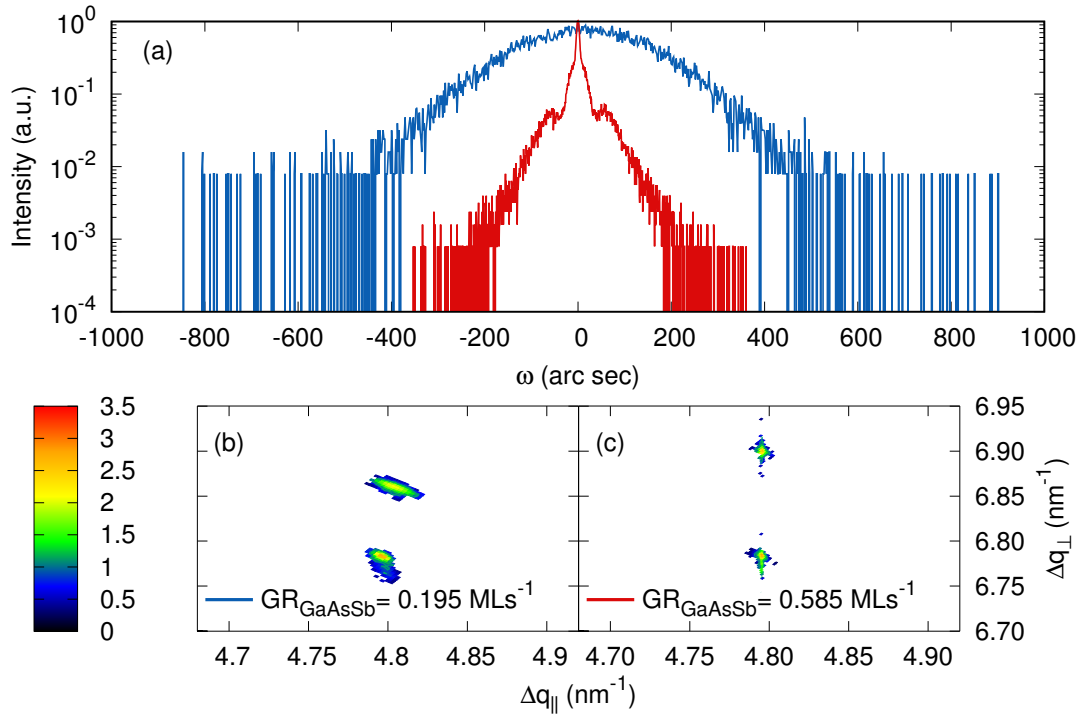


**Figure 7.7:** Rockingcurve (a) and RSM(b,c) scans of GaAs<sub>1-x</sub>Sb<sub>x</sub> layers grown at different growth rates. The sample grown at the lower growth rate of 0.195 ML s<sup>-1</sup> shows FWHM of 250 arcsec, while the layer grown at 0.585 ML s<sup>-1</sup> shows a FWHM of only 8 arcsec. The RSMs around the InAs (224) diffraction peak show a relaxation of 25 % for the GaAs<sub>1-x</sub>Sb<sub>x</sub> layer grown at the low growth rate and a fully strained layer for the sample grown at the high growth rate.

The effect of early relaxation can also be seen by comparing the crystal quality of highly lattice mismatched layers. The two samples shown in figure 7.5 (b) which have been grown at the lower  $P_{\text{As}_2}$  and at a  $R_{\text{GaAsSb}}$  of  $\sim 0.45 \text{ ML s}^{-1}$  and  $0.88 \text{ ML s}^{-1}$  have almost identical compositions. However, the layer grown at the higher growth rate shows a rocking curve peak FWHM of 1140 arcsec while the layer grown at the lower growth rate shows a peak with of 1710 arcsec which is an increase of about 50 %. This observation indicates that the mechanism, controlling the Sb incorporation at low growth rates, facilitates the strain relaxation in the  $\text{GaAs}_{1-x}\text{Sb}_x$  layers.

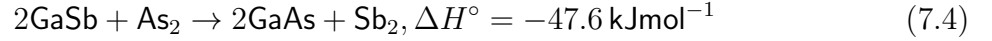
From these results we can conclude that the crystal quality of  $\text{GaAs}_{1-x}\text{Sb}_x$  layers is not solely defined by the relaxation due to lattice mismatch. Layers grown at low growth rates already show partial relaxation at compositions which yield a fully strained layer when a high growth rate is used.

## 7.4 Discussion

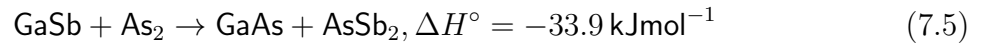
Different mechanisms for the incorporation of Sb into  $\text{GaAs}_{1-x}\text{Sb}_x$  layers were proposed in literature. Semenov and coworkers found an increase in the As mole fraction with increasing growth rates and attributed this to a shortage of Sb. These observations can be confirmed for the high growth rate side of the experiment. Three independent studies found a decrease in the As mole fraction with an increasing growth rate and provided different theories to explain their observations. Sun et. al. suggested that this increase in the Sb mole fraction is related to the availability of Ga sites which prevent the desorption of Sb species, and hence, increase the incorporation of Sb into the  $\text{GaAs}_{1-x}\text{Sb}_x$  layers. Under this assumption, the sticking coefficient of Sb would have to increase super linearly with the availability of Ga sites since the  $\frac{P_{\text{Sb}}}{P_{\text{Ga}}}$  fraction is decreasing when the  $R_{\text{GaAsSb}}$  is raised. Furthermore, the Sb sticking coefficient should be independent of the  $P_{\text{Sb}_2}$ . Hence, increasing  $P_{\text{Sb}_2}$  would have a similar effect on the high and on the low growth rate side of the experiment. In figure 7.5, however, we see that increasing the  $P_{\text{Sb}_2}$  has a much stronger effect on the high growth rate side. Moreover, the incorporation of As would have to be independent of the  $R_{\text{GaAsSb}}$ , since it would counteract the increase in the Sb mole fraction. Bosacchi et. al. suggested that the dissociation of  $\text{Sb}_4$  into  $\text{Sb}_2$  is enhanced when a higher density of Ga sites is available. The arguments which speak against this mechanism proposed, by Sun et. al., can also be applied to this theory. Moreover, an enhanced incorporation of Sb at higher growth rates was also found when  $\text{Sb}_4$  is cracked into  $\text{Sb}_2$  by using a cracker cell. This indicates that dissociation of  $\text{Sb}_4$  is not the predominant mechanism in this experiment.

In figure 7.5 we also see that the growth temperature has a stronger influence on the composition of the  $\text{GaAs}_{1-x}\text{Sb}_x$  layer at low growth rates. The fact that the high growth rate side for both curves overlap shows that the desorption of Sb is only slightly dependent of the  $T_g$  in this temperature range. This agrees with line-of-sight quatropole mass spectrometry (QMS) measurements by Kaspi and coworkers[129, 130]. Since the desorption of Ga can be neglected at these temperatures[131] and, hence, the availability of Ga sites is temperature independent, the difference between the  $\text{GaAs}_{1-x}\text{Sb}_x$  layers grown at different temperatures has to be explained by a different effect. Both mechanisms cannot provide an explanation for 1) the lower Sb incorporation at elevated  $T_g$  and 2) the enhanced tendency for relaxation of  $\text{GaAs}_{1-x}\text{Sb}_x$  layers grown at low growth rates.

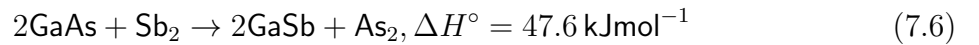
Selvig and coworkers conclude that the increase in the Sb mole fraction with higher growth rates is related to an As-for-Sb exchange reaction which takes place at the growth surface[128]. According to this mechanism, the Sb mole fraction increases with the growth rate since the time an Sb site is exposed to As flux decreases, and hence, the rate at which this event takes place is reduced. The As-for-Sb exchange reaction was previously studied by Losurdo and coworkers[100] by exposing steady GaAs and GaSb surfaces to Sb and As flux respectively. The authors found a transformation of the GaSb into GaAs while the reverse reaction is not found and conclude that the As for Sb exchange is favored due to the difference in the enthalpy of formation of the two reactions



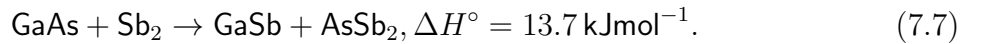
and



with respect to the reverse reactions



and



Transmission electron microscopy (TEM) analysis of GaAs layers exposed to  $\text{Sb}_2$  flux show relatively smooth interfaces while GaSb layers exposed to  $\text{As}_4$  flux show As-Sb clusters. This mechanism provides a good explanation for all the phenomena which have been found regarding the incorporation of Sb into  $\text{GaAs}_{1-x}\text{Sb}_x$  layers. Since the exchange reaction takes place at the growing surface, the chance for an Sb atom to be replaced by

an As atom is larger at the lower the growth rate. At higher  $T_g$  the reaction happens more frequently since the energy barrier for this reaction is more easily overcome. Since the imperfections such as particulates and impurities strongly influence the relaxation of strain in epitaxial layers [132, 133], the early relaxation of  $\text{GaAs}_{1-x}\text{Sb}_x$  layers grown at low growth rates can be linked to the presence of AsSb clusters originating from the As-for-Sb exchange reaction. Of the three mechanisms proposed in literature to describe the incorporation of Sb into  $\text{GaAs}_{1-x}\text{Sb}_x$  layers the As-for-Sb exchange reaction is the only one which can describe all aspects found in the experiments.

In conclusion, the incorporation of Sb into  $\text{GaAs}_{1-x}\text{Sb}_x$  layers grown on InP by MBE was studied, and the results were compared to studies on this topic found in literature. It was found that the incorporation of Sb is strongly dependent on the  $R_{\text{GaAsSb}}$ . At high growth rates, the Sb mole fraction is limited by the  $\frac{P_{\text{Sb}_2}}{P_{\text{Ga}}}$  ratio. At low growth rates the As-for-Sb exchange reaction inhibits the incorporation of Sb and leads early relaxation of lattice mismatched layers. It is evident that the growth rate is an important parameter for both composition and crystal quality of mixed As-Sb compounds.

---

## Low Temperature Grown InAs Based Intersubband Devices

---

The experimental data presented in this work show that low  $T_g$  is necessary in order to achieve high crystal quality for both, InAs and  $\text{Al}_{0.462}\text{In}_{0.538}\text{As}_y\text{Sb}_{1-y}$ . Growth performed at very low  $T_g$ , however, can lead to low device performance due to a deterioration of the optical properties and interface quality of the grown materials[134, 135]. To ensure that the requirement to grow at low a  $T_g$  does not prevent the realization of inter-subband devices, InAs-based devices using  $\text{AlAs}_{1-x}\text{Sb}_x$  barriers were designed and grown at a  $T_g$  of 400 °C.

Due to it's high conduction band offset of approximately 2.1 eV InAs/ $\text{AlAs}_{1-x}\text{Sb}_x$  is an interesting material for short-wavelength intersubband devices. Moreover, it's low effective electron mass of  $m_e = 0.021m_0$  in the well should provide an advantage over other material systems. For THz structures, however, the high conduction band offset requires the growth of very thin layers which are challenging to control by MBE. Nevertheless, a THz-structure was grown since the low electron effective mass of InAs is expected to be very advantageous for this type of structure.

### 8.1 InAs/ $\text{AlAs}_{1-x}\text{Sb}_x$ Quantum Cascade Detector

This section is based on Ref [117]. A QCD is an intersubband device which generates a photo current due to inter subband absorption [136, 137]. The structure consists of a doped active well in which electrons can be excited from the lower to the upper detector level. The excited electrons can then escape into the extractor which transfers the electron

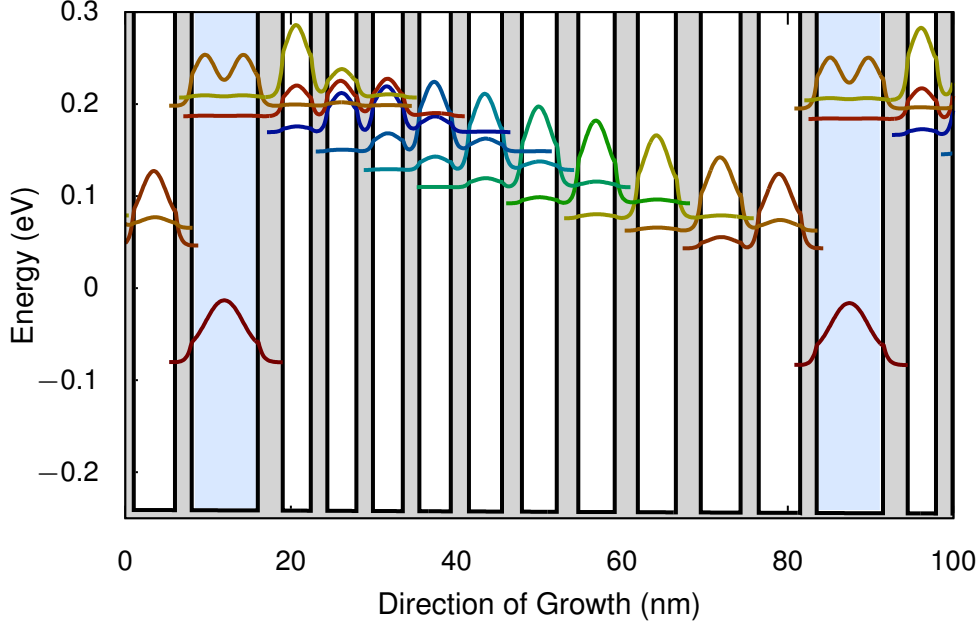


**Figure 8.1:** Conduction band diagram of the Quantum Cascade Detector (QCD) structure. The device consists of 30 repetitions of the layers **2.0|8.0|**3.0**|3.4|**2.0**|3.5|**2.0**|3.6|**2.0**|3.8|**2.2**|4.0|**2.4**|4.2|**2.6**|4.4|**2.8**|4.6|**3.0**|4.8|**2.2**|5.0** where InAs is indicated by normal font, AlAs<sub>1-x</sub>Sb<sub>x</sub> by bold font and underlined layers have intentional n-type doping of  $n = 4 \times 10^{17} \text{ cm}^{-3}$ . In this structure, an electron which is excited in the blue shaded active well from the lower (dark red) to the upper (dark orange) state, can escape into the extractor in which it relaxes down from the leftmost to the rightmost well and ends up in the active well of the next cascade.

into the active well of the next cascade. The asymmetry of the structure leads to a preferred path for the excited electrons and hence to a net photocurrent under illumination of the device.

In order to evaluate the usability of low-temperature grown InAs based structures for inter subband devices, a QCD structure with a vertical transition was designed using a semi-classical Monte-Carlo approach using the Vienna Schrödinger Poisson Solver (VSP) framework [138]. The structure consists of an active well which forms the upper and lower detector level and a series of ten quantum wells which form the extractor. The structure is shown in figure 8.1.

The sample has been grown in a Riber C21 Compact MBE system on a free-standing n-InAs (001) substrate. The substrate temperature was monitored using a calibrated 1.6  $\mu\text{m}$  pyrometer. Before deposition the oxide was thermally desorbed at 510  $^{\circ}\text{C}$  for 20 minutes under As<sub>2</sub> flux. After desorption of the oxide a 50 nm InAs buffer layer was deposited at 480  $^{\circ}\text{C}$ . The temperature was then lowered to 400  $^{\circ}\text{C}$  to deposit the heterostructure. For the group III materials standard Knudsen cells were used. For the group V materials



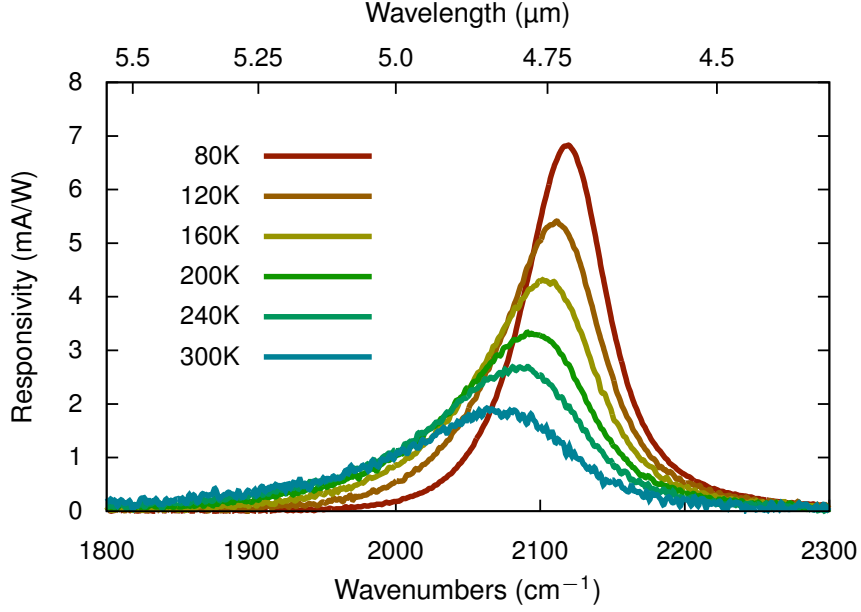


**Figure 8.2:** Representative spectral response of the QCD device. Mesa devices were illuminated by a Glowbar light source through a 45° wedge facet and the spectral response was measured by a Fourier-transform infrared spectrometer. The device showed a center detection wavelength of 4.84 μm and a responsivity of 1.9 mA W<sup>-1</sup> at room temperature.

valved cracking cells using 850 °C and 1000 °C cracking zone temperatures, to produce As<sub>2</sub> and Sb<sub>2</sub>, respectively, where used. The growth rates of InAs and AlAs<sub>1-x</sub>Sb<sub>x</sub> were set to 0.5 μm h<sup>-1</sup> and 0.18 μm h<sup>-1</sup> respectively. To ensure high crystal quality the As<sub>2</sub> pressure was calibrated using the technique described in [99]. The quality of both, the InAs and the AlAs<sub>1-x</sub>Sb<sub>x</sub> layers was examined by AFM on bulk samples prior to the growth of the heterostructure. The grown heterostructure was examined with double and triple axis HRXRD.

When mixing group V elements in MBE growth, special care has to be taken with respect to controlling the interfaces between two layers. Similar structures reported in literature often employ special shutter sequences at each interface to minimize the cross incorporation of the group V materials and thereby enhance the quality of said interface [118, 79, 81]. These growth interrupts, however, significantly prolong the growth time of a sample. For this study such growth interrupts have been omitted in order to reduce the total growth time, e.g. with respect to the sequence described in [139] by 30%. No evidence of degradation, resulting from this method, could be found in both, AFM and HRXRD examination of the sample.

The device was processed into a mesa structure by wet-chemical etching with  $H_3PO_4 : H_2O_2 : H_2O = 3 : 4 : 40$ . Ti/Au was deposited to form top and bottom contacts.

The devices were then illuminated through a 45° polished wedge faced by a Glowbar

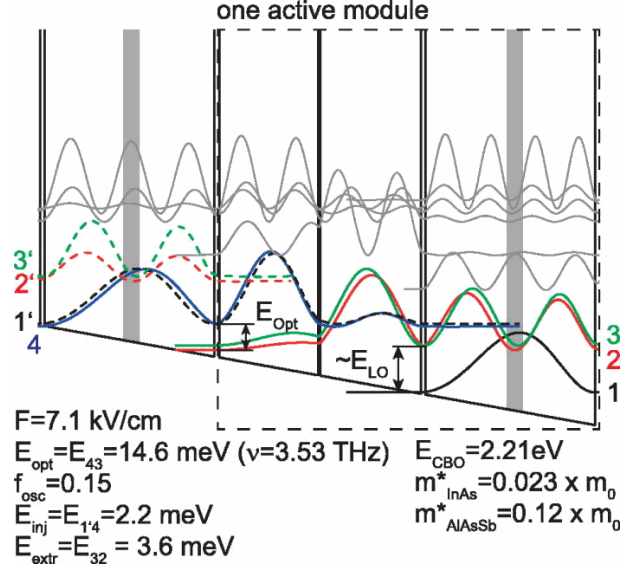


**Figure 8.3:** Conduction band diagram of the THz-QCL structure. The device consists of 121 repetitions of the layers **0.9**|19.5|**0.3**|19.8|**0.8**|33.3 where InAs is indicated by normal font, AlAs<sub>1-x</sub>Sb<sub>x</sub> by bold font and the central 3 nm of the underlined layer are intentional n-type with a density of  $n = 6.7 \times 10^{16} \text{ cm}^{-3}$ .

light source and the spectral response was measured via an Fourier-transform infrared spectrometer. It showed a peak specific detectivity  $2.7 \times 10^7 \text{ cm } \sqrt{\text{Hz}} \text{ W}^{-1}$  and a responsivity of  $1.9 \text{ mA W}^{-1}$  at 300 K at a center detection wavelength of  $4.84 \mu\text{m}$ .

## 8.2 InAs/AlAs<sub>1-x</sub>Sb<sub>x</sub> THz-QCL

This section is based on[116]. To evaluate the capabilities of low temperature grown InAs-based structure for THz devices a THz-QCL structure, shown in figure 8.3, based on a 3-well resonant phonon depletion design[140] was grown.

The THz QCL structure was grown in a Riber C21 Compact MBE system on a free-standing n+ InAs (001) substrate under the same conditions described for the QCD structure above. An HRXRD measurement of the sample is showed relatively high intensity of the satellite peaks, which indicates strain in the structure. Broadening of the satellite peaks can be found for higher orders which is an indication for fluctuations in the superlattice period. This can either be the result of actual growth rate fluctuations or random conditions at the InAs/AlAs<sub>1-x</sub>Sb<sub>x</sub> interfaces due to the omission of growth interrupts.

Double metal ridge resonator devices where processed via Au-Au wafer bonding and measurements where performed in an liquid He cryostat. The emitted light was collected using a p-doped Ge:Ga detector and a magnetic field was applied perpendicular to the

layer structure of the laser device. Figure 8.4 shows the voltage versus current density (IV) (a) and emitted light intensity versus current density (LI) (b) characteristics for different applied magnetic field strength of a  $2\text{ mm} \times 90\text{ }\mu\text{m}$  large device. For increasing field strength we see a reduction of the current density in the IV curve. This is attributed to the suppression of parasitic current paths and magnetoresistance. The LI characteristic shows no laser emission up until a magnetic field strength of 4.3 T. For higher field strengths, light emission, and a decreasing threshold current density with increasing field strengths is found. As shown in the inset of figure 8.4(a) the first and second Landau levels of the upper laser state cross the second and third Landau levels of the lower laser state around a field strength of  $\sim 3\text{ T}$ . This leads to an enhanced elastic depopulation of the upper laser state and hence laser emission is not possible.

The spectral response from a  $1\text{ mm} \times 120\text{ }\mu\text{m}$  large device was measured using a magnetic field tunable InSb detector and is shown in figure 8.5. The broad spectral response of  $\sim 0.5\text{ THz}$  of the detector prevents the resolution of individual laser modes, however a clear peak emission at  $\sim 3.8\text{ THz}$  was observed.

This is the first report of laser operation in the THz-regime for an InAs based device. Although laser operation could only be shown at liquid He temperature in the presence of high magnetic field strength, improvements in both, design of the laser structure and the quality of the grown material may lead to a significant enhancement in the operation of THz-QCLs in the future.

## 8.3 Discussion

In order to evaluate the influence of a low  $T_g$ , a QCD and a THz-QCL structure were grown by MBE. The QCD structure was processed into mesa devices and the spectral response of the devices was measured. A center detection wavelength of  $4.84\text{ }\mu\text{m}$  and a responsivity of  $1.9\text{ mA W}^{-1}$  was measured. The THz-QCL structure was processed into ridge devices and measured at liquid He temperature. By applying a magnetic field above 4.4 T laser emission was found at a center frequency of 3.8 THz. This is the first report of laser emission in the THz regime from an InAs based device.

The results show that the low  $T_g$  does not prevent the use of InAs based structures for the production of intersubband devices. In both, the MIR and the THz regime, excellent results were obtained and it can be expected that even higher performance can be reached by improving growth techniques and device structures.

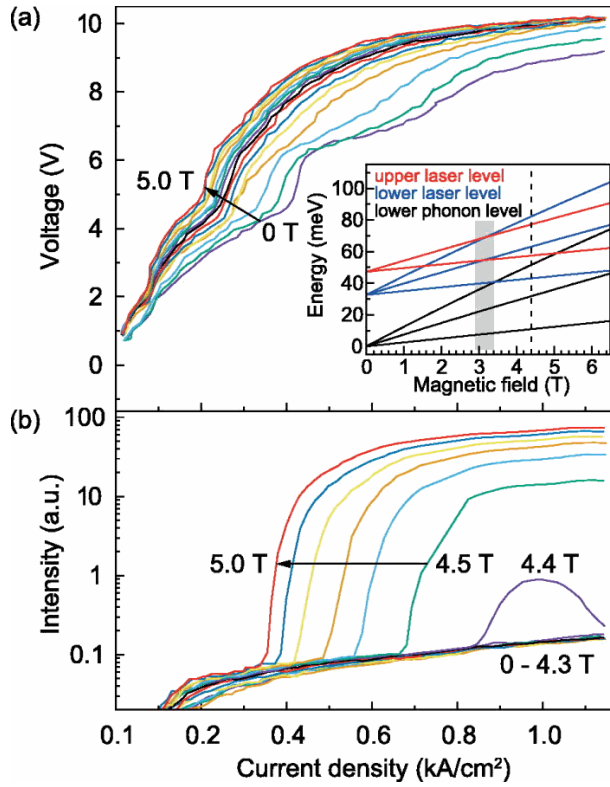


**Figure 8.4:** Voltage (a) and emitted output power (b) over current density of the THz-QCL. For increasing field strengths a reduction in the current density is found. Light emission is found at field strength above 4.4 T. At this field strength

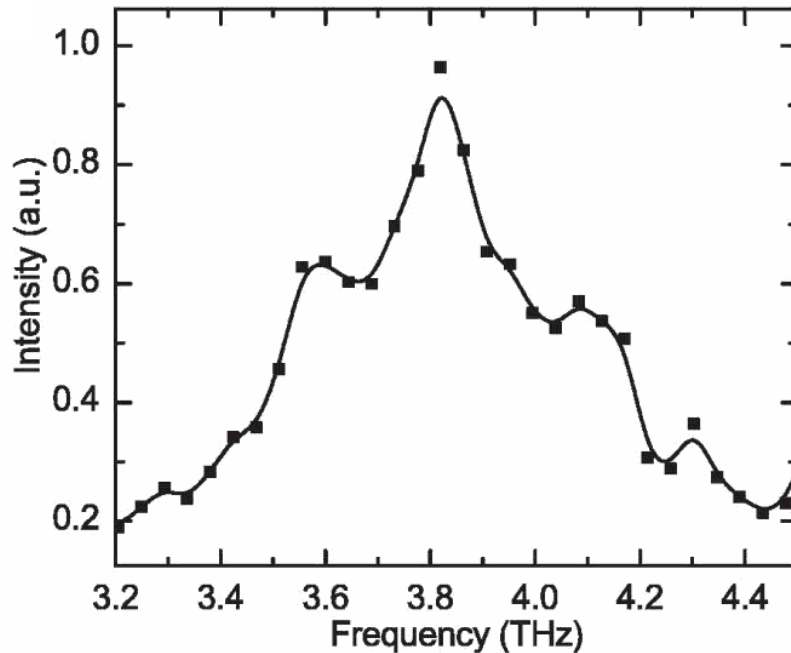


**Figure 8.5:** Spectral response of a laser device with the dimensions  $1\text{ mm} \times 120\text{ }\mu\text{m}$ . The device was measured in a liquid He cryostat under a magnetic field of 5 T applied perpendicular to the layers and at a current density of  $1\text{ kA cm}^{-2}$ .

## CHAPTER 9

---

### Discussion and Outlook

---

InAs based devices are excellent candidates for next generation THz devices. Due to the low effective electron mass in the well, high intersubband gain can be expected.  $\text{Al}_x\text{In}_{1-x}\text{As}_y\text{Sb}_{1-y}$  is a well suited barrier material to be used for InAs based devices since it allows for precise tailoring of the required band offset. Due to its novelty, however the growth of this material by MBE is not very well established. In order to determine the optimal growth parameters for the production of high quality semiconductor heterostructures featuring  $\text{Al}_x\text{In}_{1-x}\text{As}_y\text{Sb}_{1-y}$  layers, the growth of  $\text{Al}_{0.462}\text{In}_{0.538}\text{As}_y\text{Sb}_{1-y}$  lattice matched to InAs was investigated. It was shown that the incorporation of Sb into  $\text{Al}_{0.462}\text{In}_{0.538}\text{As}_y\text{Sb}_{1-y}$  is strongly temperature dependent and that this is determining the upper limit of the  $T_g$  for which lattice matching can be achieved. Moreover, it was found that the quality of the grown material is very sensitive to the used  $P_{\text{As}_2}$ , and that low pressures, which are necessary to achieve lattice matching, dramatically increase the roughness of the grown layer. It was furthermore found that the growth of compositions close to lattice matching at a  $T_g$  of 445 °C leads to decomposition of  $\text{Al}_x\text{In}_{1-x}\text{As}_y\text{Sb}_{1-y}$  into  $\text{Al}_x\text{In}_{1-x}\text{As}$  and  $\text{Al}_x\text{In}_{1-x}\text{Sb}$  and the formation of crystallites which significantly decreases in crystal quality. Below this limit, the requirements for the growth of high quality  $\text{Al}_{0.462}\text{In}_{0.538}\text{As}_y\text{Sb}_{1-y}$  and lattice matched growth can be met simultaneously. At a growth temperature of 410 °C, high quality  $\text{Al}_{0.462}\text{In}_{0.538}\text{As}_y\text{Sb}_{1-y}$  layers, confirmed by both HRXRD and AFM measurements, were grown. Using the information gathered in this study, two samples were grown on a Riber C21 MBE system on freestanding n+ InAs (001) wafers at a  $T_g$  of 410 °C. Al mole fractions of 0.25 and 0.53 were chosen and the

---

As<sub>2</sub> BEP was adjusted for high quality InAs. P<sub>Sb<sub>2</sub></sub> was then adjusted in order to achieve lattice matching with InAs. For both compositions high-quality material, confirmed by HRXRD and AFM measurements was obtained.

Since it was found that the mixing of As and Sb is the primary cause of low crystal quality in MBE grown Al<sub>x</sub>In<sub>1-x</sub>As<sub>y</sub>Sb<sub>1-y</sub>, the mechanisms which determine the composition and quality of a III-AsSb layer have to be investigated in detail. GaAs<sub>1-x</sub>Sb<sub>x</sub> was chosen as the model system for the mixing of As and Sb since the presence of only one group III material reduces the room for interpretation and facilitates the collection of reliable data. The quality of GaAs<sub>1-x</sub>Sb<sub>x</sub> layers grown at different substrate temperatures was investigated by HRXRD. It was found that the peak width in  $\omega$  direction is drastically reduced if the growth temperature is lowered. Moreover, also the homogeneity across the wafer was found to depend substantially on the growth temperature. At a growth temperature of 480 °C a shift in the composition of the GaAs<sub>1-x</sub>Sb<sub>x</sub> layers by more than 3.5 % was found over a distance of 16 mm. This shift could be eliminated by reducing the growth temperature below 430 °C.

The mechanisms which govern the composition of layers in which As and Sb are mixed were investigated by growing GaAs<sub>1-x</sub>Sb<sub>x</sub> layers at different Ga fluxes. While other publications either found a monotonic increase or a monotonic decrease in the As mole fraction in GaAs<sub>1-x</sub>Sb<sub>x</sub> layers with rising Ga fluxes, a U-shaped profile of the composition was found. It was concluded that the authors did only measure one of the effects that determine the composition of the GaAs<sub>1-x</sub>Sb<sub>x</sub> layers depending on the specific conditions that were chosen. The rise in the As mole fraction at high Ga fluxes i.e. high growth rates was concluded to originate from a shortage of Sb. On the low growth rate side, the increase in As mole fraction was found to be related to an As-for-Sb exchange reaction which happens more efficiently at low growth rates. This observation was corroborated by an experiment which showed a strong temperature dependence of the As mole fraction at low growth rates, while the composition is insensitive to the growth temperature on the high growth rate side.

Moreover, a strong influence of the growth rate on the crystal quality of the GaAs<sub>1-x</sub>Sb<sub>x</sub> layers was found. At low growth rates, strained GaAs<sub>1-x</sub>Sb<sub>x</sub> layers show a stronger degree of relaxation and hence lower crystal quality than at high growth rates. It was concluded that the As-for-Sb exchange reaction leads to the formation of AsSb clusters which act as seed for the formation of dislocations and hence promote the relaxation of the strain in the layers. The experiments show that the growth rate plays an important role for the quality of these layers. Delicate tuning of growth rates, growth temperature as well as As and Sb fluxes is necessary in order to obtain high crystal quality material.

---

Since the As-for-Sb exchange reaction happens at an increased rate at elevated temperatures, lower substrate temperatures facilitate the production high crystal quality layers. Low substrate temperatures, however, may also lead to the deterioration of the optical properties and the interface quality of the grown layers.

In order to determine the influence of the low growth temperature on the performance of intersubband devices, a THz-QCL and a QCD structure were grown. Both heterostructures were first examined by HRXRD and AFM and later processed into devices. For the QCD structure, a center detection wavelength of  $4.84\text{ }\mu\text{m}$  and a responsivity of  $1.9\text{ mA W}^{-1}$  were measured. Light emission from the THz-QCL structure was measured by applying a magnetic field above  $4.4\text{ T}$  within a liquid He cryostat. This result is the first record of coherent light emission in the THz-regime from an InAs based device. Both results show that the necessity to grow InAs based heterostructures employing mixed group V compounds at low substrate temperatures does not hinder the application of these materials intersubband devices.

Further improvement and understanding of the growth process and the properties of these materials will allow to exploit the low effective electron mass of InAs for high performance intersubband devices in the future. To enable the broad use of  $\text{Al}_x\text{In}_{1-x}\text{As}_y\text{Sb}_{1-y}$  as a barrier material for intersubband devices, the properties of this material, like effective electron mass and conduction band offset has to be determined for various compositions.

Since semi-insulating InAs substrates are not available[141], multi pass intersubband absorption measurements[29] will suffer from high absorption in the substrate and hence cannot be performed straightforwardly for this material system. New developments in direct wafer bonding[50], however, would allow for the transfer of the heterostructure onto a semi-insulating substrate and hence, excessive absorption in the substrate could be avoided. Determination of the conduction band offset can also be achieved by performing ballistic carrier emission experiments[142, 143]. Moreover, Shubnikov-de Haas oscillations may be used to measure the effective electron mass in  $\text{Al}_x\text{In}_{1-x}\text{As}_y\text{Sb}_{1-y}$ [144, 145, 146].

Precise knowledge of the electronic and optical properties of  $\text{Al}_x\text{In}_{1-x}\text{As}_y\text{Sb}_{1-y}$  and InAs/ $\text{Al}_x\text{In}_{1-x}\text{As}_y\text{Sb}_{1-y}$  heterostructures will allow the production of high-performance intersubband devices. In the long run InAs/ $\text{Al}_x\text{In}_{1-x}\text{As}_y\text{Sb}_{1-y}$  based devices may be able to surpass the performance of devices based on the much more mature GaAs/ $\text{Al}_x\text{Ga}_{1-x}\text{As}$  and  $\text{Ga}_x\text{In}_{1-x}\text{As}$ / $\text{Al}_x\text{In}_{1-x}\text{As}$  material systems in terms of both, output power and maximum operation temperature and thus enable the further advancement of THz technology into real world applications.





---

## Bibliography

---

- [1] B. H. Stuart. *Infrared Spectroscopy: Fundamentals and Applications (Analytical Techniques in the Sciences (AnTs) \*)*. Wiley, 2004.
- [2] *HITRAN Online Database*. <http://hitran.org/>. Accessed: 2016-08-25.
- [3] M. Amann, F. Capasso, A. Larsson, and M. Pessa. “Focus on advanced semiconductor heterostructures for optoelectronics”. *New Journal of Physics* 11 (2009).
- [4] A. Krier. *Mid-infrared Semiconductor Optoelectronics (Springer Series in Optical Sciences)*. Springer, 2006.
- [5] R. Hall, G. Fenner, J. Kingsley, T. Soltys, and R. Carlson. “Coherent light emission from GaAs junctions”. *Physical Review Letters* 9.9 (1962), pp. 366–368.
- [6] M. Nathan, W. Dumke, G. Burns, F. Dill Jr., and G. Lasher. “Stimulated emission of radiation from GaAs p-n junctions”. *Applied Physics Letters* 1.3 (1962), pp. 62–64.
- [7] T. Quist, R. Rediker, R. Keyes, W. Krag, B. Lax, A. McWhorter, and H. Zeigler. “Semiconductor maser of GaAs”. *Applied Physics Letters* 1.4 (1962), pp. 91–92.
- [8] S. Nakamura, M. Senoh, S.-i. Nagahama, N. Iwasa, T. Yamada, T. Matsushita, H. Kiyoku, and Y. Sugimoto. “InGaN-based multi-quantum-well-structure laser diodes”. *Japanese Journal of Applied Physics, Part 2: Letters* 35.1 B (1996), pp. L74–L76.
- [9] Q. Lu and M. Razeghi. “Recent Advances in Room Temperature, High-Power Terahertz Quantum Cascade Laser Sources Based on Difference-Frequency Generation”. *Photonics* 3.3 (2016), p. 42.
- [10] H. Choi. *Long-Wavelength Infrared Semiconductor Lasers (Wiley Series in Lasers and Applications)*. Wiley-Interscience, 2008.

- [11] B. Williams. “Terahertz quantum-cascade lasers”. *Nature Photonics* 1.9 (2007), pp. 517–525.
- [12] R. F. Kazarinov and R. A. Suris. “Possibility of the amplification of electromagnetic waves in a semiconductor with a superlattice”. *Sov Phys Semicond* 5.4 (1971), pp. 707–709.
- [13] R. F. Kazarinov and R. A. Suris. “Electric and electromagnetic properties of semiconductors with a superlattice”. *Sov. Phys. Semicond.* 6 (1972), pp. 120–131.
- [14] J. Faist, F. Capasso, D. Sivco, C. Sirtori, A. Hutchinson, and A. Cho. “Quantum cascade laser”. *Science* 264.5158 (1994), pp. 553–556.
- [15] S. S. Kim, C. Young, and B. Mizaikoff. “Miniaturized mid-infrared sensor technologies”. *Analytical and Bioanalytical Chemistry* 390.1 (2008), pp. 231–237.
- [16] F. K. Tittel, D. Richter, and A. Fried. “Solid-State Mid-Infrared Laser Sources”. Springer, 2003. Chap. “Mid-Infrared Laser Applications in Spectroscopy”, pp. 458–529.
- [17] J. Wagner, C. Mann, M. Rattunde, and G. Weimann. “Infrared semiconductor lasers for sensing and diagnostics”. *Applied Physics A: Materials Science and Processing* 78.4 (2004), pp. 505–512.
- [18] B. Schwarz, P. Reininger, D. Ristanić, H. Detz, A. Andrews, W. Schrenk, and G. Strasser. “Monolithically integrated mid-infrared lab-on-a-chip using plasmonics and quantum cascade structures”. *Nature Communications* 5 (2014).
- [19] M. Tonouchi. “Cutting-edge terahertz technology”. *Nature Photonics* 1.2 (2007), pp. 97–105.
- [20] P. Siegel. “Terahertz technology”. *IEEE Transactions on Microwave Theory and Techniques* 50.3 (2002), pp. 910–928.
- [21] J. Darmo, V. Tamosiunas, G. Fasching, J. Kröll, K. Unterrainer, M. Beck, M. Giovannini, J. Faist, C. Kremser, and P. Debbage. “Imaging with a Terahertz quantum cascade laser”. *Opt. Express* 12.9 (2004), pp. 1879–1884.
- [22] N. W. Ashcroft and D. N. Mermin. *Festkörperphysik*. Oldenbourg Wissensch.Vlg, 2007.
- [23] A. Bravais. “Mémoire sur les systèmes formés par des points distribués régulièrement sur un plan ou dans l’espace”. *Journal de l’Ecole Polytechnique* 19 (1850), pp. 1–128.

- 
- [24] A. ravais. *Abhandlung über die Systeme von regelmässig auf einer Ebene oder im Raum vertheilten Punkten*. Uebersetzt und herausgegeben von C. und E. Blasius. Leipzig: Verlag von Wilhelm Engelmann, 1897.
- [25] G. M. Fasching. *Werkstoffe für die Elektrotechnik – Mikrophysik, Struktur, Eigenschaften (German Edition)*. Springer, 2004.
- [26] H. J. Joyce, J. Wong-Leung, Q. Gao, H. H. Tan, and C. Jagadish. “Phase Perfection in Zinc Blende and Wurtzite III–V Nanowires Using Basic Growth Parameters”. *Nano Letters* 10.3 (2010), pp. 908–915.
- [27] A. R. Denton and N. W. Ashcroft. “Vegard’s law”. *Phys. Rev. A* 43 (6 1991), pp. 3161–3164.
- [28] I. Vurgaftman, J. R. Meyer, and L. R. Ram-Mohan. “Band parameters for II–V compound semiconductors and their alloys”. *Journal of Applied Physics* 89.11 (2001), pp. 5815–5875.
- [29] M. Nobile, H. Detz, E. Mujagić, A. Andrews, P. Klang, W. Schrenk, and G. Strasser. “Midinfrared intersubband absorption in InGaAs/GaAsSb multiple quantum wells”. *Applied Physics Letters* 95.4 (2009).
- [30] M. Levinstein, S. Rumyantsev, and M. Shur. *Handbook Series on Semiconductor Parameters - Volume 1: Si, Ge, C (Diamond), GaAs, GaP, GaSb, InAs, InP, InSb*. World Scientific Publishing Company, 1996.
- [31] M. Levinstein, S. Rumyantsev, and M. Shur. *Handbook Series on Semiconductor Parameters - Volume 2: Ternary And Quaternary III-V Compounds*. World Scientific Pub Co Inc, 1996.
- [32] J. Faist. *Quantum Cascade Lasers*. Oxford University Press, 2013.
- [33] R. Paiella. *Intersubband Transitions in Quantum Structures*. McGraw-Hill Companies, The, 2006.
- [34] C. Sirtori, J. Faist, F. Capasso, D. Sivco, A. Hutchinson, S. Chu, and A. Cho. “Continuous wave operation of midinfrared (7.4-8.6  $\mu\text{m}$ ) quantum cascade lasers up to 110 K temperature”. *Applied Physics Letters* 68.13 (1996), pp. 1745–1747.
- [35] J. Faist, F. Capasso, C. Sirtori, D. Sivco, A. Hutchinson, and A. Cho. “Room temperature mid-infrared quantum cascade lasers”. *Electronics Letters* 32.6 (1996), pp. 560–561.

- [36] M. Beck, D. Hofstetter, T. Aellen, J. Faist, U. Oesterle, M. Ilegems, E. Gini, and H. Melchior. “Continuous wave operation of a mid-infrared semiconductor laser at room temperature”. *Science* 295.5553 (2002), pp. 301–305.
- [37] J. Devenson, O. Cathabard, R. Teissier, and A. Baranov. “InAs/AlSb quantum cascade lasers emitting at 2.75-2.97  $\mu\text{m}$ ”. *Applied Physics Letters* 91.25 (2007).
- [38] R. Colombelli, F. Capasso, C. Gmachl, A. Hutchinson, D. Sivco, A. Tredicucci, M. Wanke, A. Sergent, and A. Cho. “Far-infrared surface-plasmon quantum-cascade lasers at 21.5  $\mu\text{m}$  and 24  $\mu\text{m}$  wavelengths”. *Applied Physics Letters* 78.18 (2001), pp. 2620–2622.
- [39] C. Gmachl, F. Capasso, D. Sivco, and A. Cho. “Recent progress in quantum cascade lasers and applications”. *Reports on Progress in Physics* 64.11 (2001), pp. 1533–1601.
- [40] M. S. Vitiello, G. Scalari, B. Williams, and P. D. Natale. “Quantum cascade lasers: 20 years of challenges”. *Opt. Express* 23.4 (2015), pp. 5167–5182.
- [41] C. Sirtori, P. Kruck, S. Barbieri, P. Collot, J. Nagle, M. Beck, J. Faist, and U. Oesterle. “GaAs/Al<sub>x</sub>Ga<sub>1-x</sub>As quantum cascade lasers”. *Applied Physics Letters* 73.24 (1998), pp. 3486–3488.
- [42] R. K"ohler, A. Tredicucci, F. Beltram, H. Beere, E. Linfield, A. Davies, D. Ritchie, R. Iotti, and F. Rossi. “Terahertz semiconductor-heterostructure laser”. *Nature* 417.6885 (2002), pp. 156–159.
- [43] S. Fatholouloumi, E. Dupont, C. Chan, Z. Wasilewski, S. Laframboise, D. Ban, A. Mátyás, C. Jirauschek, Q. Hu, and H. Liu. “Terahertz quantum cascade lasers operating up to  $\sim 200$  K with optimized oscillator strength and improved injection tunneling”. *Optics Express* 20.4 (2012), pp. 3866–3876.
- [44] C. Deutsch, H. Detz, M. Krall, M. Brandstetter, T. Zederbauer, A. Andrews, W. Schrenk, G. Strasser, and K. Unterrainer. “Dopant migration effects in terahertz quantum cascade lasers”. *Applied Physics Letters* 102.20 (2013).
- [45] F. Zernike Jr. and P. Berman. “Generation of far infrared as a difference frequency”. *Physical Review Letters* 15.26 (1965), pp. 999–1001.
- [46] K. Kawase, J.-I. Shikata, and H. Ito. “Terahertz wave parametric source”. *Journal of Physics D: Applied Physics* 35.3 (2002).

- 
- [47] M. Scheller, J. Yarborough, J. Moloney, M. Fallahi, M. Koch, and S. Koch. “Room temperature continuous wave milliwatt terahertz source”. *Optics Express* 18.26 (2010), pp. 27112–27117.
- [48] M. Krall, M. Brandstetter, C. Deutsch, H. Detz, A. Andrews, W. Schrenk, G. Strasser, and K. Unterrainer. “Subwavelength micropillar array terahertz lasers”. *Optics Express* 22.1 (2014), pp. 274–282.
- [49] M. Brandstetter, C. Deutsch, M. Krall, H. Detz, D. Macfarland, T. Zederbauer, A. Andrews, W. Schrenk, G. Strasser, and K. Unterrainer. “High power terahertz quantum cascade lasers with symmetric wafer bonded active regions”. *Applied Physics Letters* 103.17 (2013).
- [50] M. Brandstetter, C. Deutsch, A. Benz, G. Cole, H. Detz, A. Andrews, W. Schrenk, G. Strasser, and K. Unterrainer. “THz quantum cascade lasers with wafer bonded active regions”. *Optics Express* 20.21 (2012), pp. 23832–23837.
- [51] C. Sirtori, S. Barbieri, and R. Colombelli. “Wave engineering with THz quantum cascade lasers”. *Nature Photonics* 7.9 (2013), pp. 691–701.
- [52] F. Valmorra, G. Scalari, K. Ohtani, M. Beck, and J. Faist. “InGaAs/AlInGaAs THz quantum cascade lasers operating up to 195 K in strong magnetic field”. *New Journal of Physics* 17 (2015).
- [53] C. Deutsch, H. Detz, T. Zederbauer, M. Krall, M. Brandstetter, A. Andrews, P. Klang, W. Schrenk, G. Strasser, and K. Unterrainer. “InGaAs/GaAsSb/InP terahertz quantum cascade lasers”. *Journal of Infrared, Millimeter, and Terahertz Waves* 34.5-6 (2013), pp. 374–385.
- [54] C. Deutsch, M. Krall, M. Brandstetter, H. Detz, A. Andrews, P. Klang, W. Schrenk, G. Strasser, and K. Unterrainer. “High performance InGaAs/GaAsSb terahertz quantum cascade lasers operating up to 142 K”. *Applied Physics Letters* 101.21 (2012).
- [55] K. A., B. G., and W. J. “Molecular Beam Epitaxy of High-Quality GaAs and AlGaAs”. *Optical Characterization of Epitaxial Semiconductor Layers*. Ed. by G. Bauer and W. Richter. Springer, 1995. Chap. 6, pp. 287–391.
- [56] J. Matthews and A. Blakeslee. “Defects in epitaxial multilayers. I. Misfit dislocations”. *Journal of Crystal Growth* 27.C (1974), pp. 118–125.
- [57] A. Braun, K. Briggs, and P. Böni. “Analytical solution to Matthews’ and Blakeslee’s critical dislocation formation thickness of epitaxially grown thin films”. *Journal of Crystal Growth* 241.1-2 (2002), pp. 231–234.

- [58] R. A. Kubiak, S. M. Newstead, and P. Sullivan. “The Technology and Design of Molecular Beam Epitaxy Systems”. *Molecular Beam Epitaxy: Applications to Key Materials (Materials Science and Process Technology)*. Ed. by R. F. Farrow. William Andrew, 1996. Chap. 1, pp. 1–113.
- [59] P. Brewer, D. Chow, and R. Miles. “Atomic antimony for molecular beam epitaxy of high quality III-V semiconductor alloys”. *Journal of Vacuum Science and Technology B: Microelectronics and Nanometer Structures* 14.3 (1996), pp. 2335–2338.
- [60] Y. Rouillard, B. Lambert, Y. Toudic, M. Baudet, and M. Gauneau. “On the use of dimeric antimony in molecular beam epitaxy”. *Journal of Crystal Growth* 156.1-2 (1995), pp. 30–38.
- [61] R. T. Bayard and D. Alpert. “Extension of the Low Pressure Range of the Ionization Gauge”. *Review of Scientific Instruments* 21.6 (1950), pp. 571–572.
- [62] M. A. Herman and H. Sitter. *Molecular Beam Epitaxy: Fundamentals and Current Status (Springer series in materials science)*. Springer-Verlag Berlin und Heidelberg GmbH & Co. K, 1989.
- [63] ed.-in-chief W. M. Haynes. *CRC Handbook of Chemistry and Physics, 93rd Edition (CRC Handbook of Chemistry & Physics)*. CRC Press, 2012.
- [64] P. I. Cohen, G. S. Petrich, and G. J. Whaley. “Reflection High Energy Electron Diffraction Studies of the Dynamics of Molecular Beam Epitaxy”. *Molecular Beam Epitaxy: Applications to Key Materials (Materials Science and Process Technology)*. Ed. by R. F. Farrow. William Andrew, 1996. Chap. 8, pp. 669–744.
- [65] D. K. Biegelsen, R. D. Bringans, J. E. Northrup, and L.-E. Swartz. “Surface reconstructions of GaAs(100) observed by scanning tunneling microscopy”. *Phys. Rev. B* 41 (9 1990), pp. 5701–5706.
- [66] V. P. LaBella, H. Yang, D. W. Bullock, P. M. Thibado, P. Kratzer, and M. Scheffler. “Atomic Structure of the GaAs(001) – (2 × 4) Surface Resolved Using Scanning Tunneling Microscopy and First-Principles Theory”. *Phys. Rev. Lett.* 83 (15 1999), pp. 2989–2992.
- [67] W. Friedrich, P. Knipping, and M. von Laue. “Interferenz-Erscheinungen bei Röntgenstrahlen”. *Sitzungsberichte der Mathematisch-Physikalischen Classe der Königlich-Bayerischen Akademie der Wissenschaften zu München*. 1912: 303. (1912).

- 
- [68] W. L. Bragg. “The Specular Reflection of X-rays.” *Nature* 90 (1912), p. 410.
- [69] W. L. Bragg. “The diffraction of short electromagnetic waves by a crystal”. *Proceedings of the Cambridge Philosophical Society*. Vol. 17. 1913, pp. 43–57.
- [70] J. Als-Nielsen and D. McMorrow. *Elements of Modern X-ray Physics*. Wiley, 2001.
- [71] B. D. Cullity. *Elements of X-Ray Diffraction (Addison-Wesley series in metallurgy and materials)*. Addison-Wesley, 1978.
- [72] A. Ichimiya and P. I. Cohen. *Reflection High-Energy Electron Diffraction*. Cambridge University Press, 2004.
- [73] F. C. “Atomic Force Microscopy”. *Nanoscience: Nanotechnologies and Nanophysics*. Ed. by C. Dupas, P. Houdy, and M. Lahmani. Springer, 2006. Chap. 4, pp. 91–119.
- [74] Z. Cui. *Nanofabrication: Techniques and Principles*. Springer, 2011.
- [75] J. Goldstein, D. E. Newbury, D. C. Joy, C. E. Lyman, P. Echlin, E. Lifshin, L. Sawyer, and J. Michael. *Scanning Electron Microscopy and X-ray Microanalysis: Third Edition*. Springer, 2013.
- [76] J. A. Bearden. “X-Ray Wavelengths”. *Rev. Mod. Phys.* 39 (1 1967), pp. 78–124.
- [77] E. Benveniste, A. Vasanelli, A. Delteil, J. Devenson, R. Teissier, A. Baranov, A. Andrews, G. Strasser, I. Sagnes, and C. Sirtori. “Influence of the material parameters on quantum cascade devices”. *Applied Physics Letters* 93.13 (2008).
- [78] H. Kroemer. “The 6.1 Å family (InAs, GaSb, AlSb) and its heterostructures: a selective review”. *Physica E: Low-dimensional Systems and Nanostructures* 20.3-4 (2004), pp. 196–203.
- [79] R. Teissier, D. Barate, A. Vicet, C. Alibert, A. Baranov, X. Marcadet, C. Renard, M. Garcia, C. Sirtori, D. Revin, and J. Cockburn. “Room temperature operation of InAs/AlSb quantum cascade lasers”. *Applied Physics Letters* 85.2 (2004), pp. 167–169.
- [80] J. Devenson, R. Teissier, O. Cathabard, and A. Baranov. “InAs/AlSb quantum cascade lasers emitting below 3  $\mu\text{m}$ ”. *Applied Physics Letters* 90.11 (2007).
- [81] X. Marcadet, C. Renard, M. Carras, M. Garcia, and J. Massies. “InAs/AlAsSb based quantum cascade lasers”. *Applied Physics Letters* 91.16 (2007).
- [82] S. Sze and K. K. Ng. *Physics of semiconductor devices*. Hoboken, NJ: Wiley, 2007.

- [83] T. Hickmott, P. Solomon, R. Fischer, and H. Morkoç. “Negative charge, barrier heights, and the conduction-band discontinuity in  $\text{Al}_x\text{Ga}_{1-x}\text{As}$  capacitors”. *Journal of Applied Physics* 57.8 (1985), pp. 2844–2853.
- [84] C. Peng, A. Ketterson, H. Morkoç, and P. Solomon. “Determination of the conduction-band discontinuity between  $\text{In}_{0.53}\text{Ga}_{0.47}\text{As}/\text{In}_{0.52}\text{Al}_{0.48}\text{As}$  using n+-InGaAs/InAlAs/n-InGaAs Capacitors”. *Journal of Applied Physics* 60.5 (1986), pp. 1709–1712.
- [85] T. Makimoto, B. Brar, and H. Kroemer. “Hole accumulation in (In)GaSb/AlSb quantum wells induced by the Fermi-level pinning of an InAs surface”. *Journal of Crystal Growth* 150.1 -4 pt 2 (1995), pp. 883–886.
- [86] L. Olsson, C. Andersson, M. Håkansson, J. Kanski, L. Ilver, and U. Karlsson. “Charge accumulation at InAs surfaces”. *Physical Review Letters* 76.19 (1996), pp. 3626–3629.
- [87] R. E. Allen, T. J. Humphreys, J. D. Dow, and O. F. Sankey. “Theory of surface-defect states and schottky barrier heights: application to InAs.” *Journal of Vacuum Science and Technology B: Microelectronics and Nanometer Structures* 2.3 (1984), pp. 449–452.
- [88] A. Semenov, V. Solov’ev, B. Meltser, Y. Terent’ev, L. Prokopova, and S. Ivanov. “Molecular beam epitaxy of AlInAsSb alloys near the miscibility gap boundary”. *Journal of Crystal Growth* 278.1-4 (2005), pp. 203–208.
- [89] T. Zederbauer, A. M. Andrews, D. MacFarland, H. Detz, W. Schrenk, and G. Strasser. “Enhanced Crystal Quality of  $\text{Al}_x\text{In}_{1-x}\text{As}_y\text{Sb}_{1-y}$  for Terahertz Quantum Cascade Lasers”. *Photonics* 3.2 (2016), pp. 1–9.
- [90] K. Nakajima, K. Osamura, K. Yasuda, and Y. Murakami. “The pseudoquaternary phase diagram of the Ga-In-As-Sb system”. *Journal of Crystal Growth* 41.1 (1977), pp. 87–92.
- [91] G. Stringfellow. “Miscibility gaps in quaternary III/V alloys”. *Journal of Crystal Growth* 58.1 (1982), pp. 194–202.
- [92] V. Sorokin, S. Sorokin, A. Semenov, B. Meltser, and S. Ivanov. “Novel approach to the calculation of instability regions in GaInAsSb alloys”. *Journal of Crystal Growth* 216.1-4 (2000), pp. 97–103.
- [93] G. W. Turner, H. K. Choi, and H. Q. Le. “Growth of InAsSb quantum wells for long-wavelength ( $\sim 4\text{ }\mu\text{m}$ ) lasers”. *Journal of Vacuum Science & Technology B: Microelectronics and Nanometer Structures* 13.2 (1995), p. 699.



- 
- [94] A. Wilk, B. Fraisse, P. Christol, G. Boissier, P. Grech, M. El Gazouli, Y. Rouillard, A. Baranov, and A. Joullié. “MBE growth of InAs/InAsSb/InAlAsSb “W” quantum well laser diodes emitting near  $3\text{ }\mu\text{m}$ ”. *Journal of Crystal Growth* 227-228 (2001), pp. 586–590.
- [95] M. Kudo and T. Mishima. “MBE growth of Si-doped InAlAsSb layers lattice-matched with InAs”. *Journal of Crystal Growth* 175-176.PART 2 (1997), pp. 844–848.
- [96] D. Washington-Stokes, T. Hogan, P. Chow, T. Golding, U. Kirschbaum, C. Littler, and R. Lukic. “ $\text{Al}_x\text{In}_{1-x}\text{As}_y\text{Sb}_{1-y}/\text{GaSb}$  effective mass superlattices grown by molecular beam epitaxy”. *Journal of Crystal Growth* 201-202 (1999), pp. 854–857.
- [97] J. S. Rojas-Ramirez, S. Wang, R. Contreras-Guerrero, M. Caro, K. Bhatnagar, M. Holland, R. Oxland, G. Doornbos, M. Passlack, C. Diaz, and R. Droopad. “ $\text{Al}_x\text{In}_{1-x}\text{As}_y\text{Sb}_{1-y}$  alloys lattice matched to InAs(100) grown by molecular beam epitaxy”. *Journal of Crystal Growth* 425 (2015), pp. 33–38.
- [98] W. Sarney, S. Svensson, D. Wang, D. Donetsky, G. Kipshidze, L. Shterengas, Y. Lin, and G. Belenky. “AlInAsSb for M-LWIR detectors”. *Journal of Crystal Growth* 425 (2015), pp. 357–359.
- [99] H. Ye, L. Li, R. Hinkey, R. Yang, T. Mishima, J. Keay, M. Santos, and M. Johnson. “MBE growth optimization of InAs (001) homoepitaxy”. *Journal of Vacuum Science and Technology B: Nanotechnology and Microelectronics* 31.3 (2013).
- [100] M. Losurdo, P. Capezzuto, G. Bruno, A. Brown, T. Brown, and G. May. “Fundamental reactions controlling anion exchange during mixed anion heterojunction formation: Chemistry of As-for-Sb and Sb-for-As exchange reactions”. *Journal of Applied Physics* 100.1 (2006).
- [101] T. Kuech. *Handbook of Crystal Growth, Volume 3A-3B, Second Edition: Thin Films and Epitaxy*. Elsevier, 2015.
- [102] H. Detz, A. Andrews, M. Nobile, P. Klang, E. Mujagić, G. Hesser, W. Schrenk, F. Schäffler, and G. Strasser. “Intersubband optoelectronics in the InGaAs/GaAsSb material system”. *Journal of Vacuum Science and Technology B: Nanotechnology and Microelectronics* 28.3 (2010).

- [103] M. Nobile, P. Klang, E. Mujagić, H. Detz, A. Andrews, W. Schrenk, and G. Strasser. “Quantum cascade laser utilising aluminium-free material system: InGaAs/GaAsSb latticematched to InP”. *Electronics Letters* 45.20 (2009), pp. 1031–1033.
- [104] M. Nobile, H. Detz, A. Andrews, P. Klang, W. Schrenk, and G. Strasser. “An aluminum-free mid-infrared quantum cascade laser”. Vol. 7616. 2010.
- [105] R. Wang, M. Muneeb, S. Sprengel, G. Boehm, R. Baets, M.-C. Amann, and G. Roelkens. “SWIR InGaAs/GaAsSb type-II quantum well photodetectors and spectrometers integrated on SOI”. Vol. 9752. 2016.
- [106] S. Maëro, L.-A. De Vaultier, Y. Guldner, C. Deutsch, M. Krall, T. Zederbauer, G. Strasser, and K. Unterrainer. “Magnetic-field assisted performance of InGaAs/GaAsSb terahertz quantum cascade lasers”. *Applied Physics Letters* 103.5 (2013).
- [107] C. Deutsch, H. Detz, T. Zederbauer, A. Andrews, P. Klang, T. Kubis, G. Klimeck, M. Schuster, W. Schrenk, G. Strasser, and K. Unterrainer. “Probing scattering mechanisms with symmetric quantum cascade lasers”. *Optics Express* 21.6 (2013), pp. 7209–7215.
- [108] M. Patrashin, N. Sekine, A. Kasamatsu, I. Watanabe, I. Hosako, T. Takahashi, M. Sato, Y. Nakasha, and N. Hara. “Optimization of GaAsSb/InAlAs/InGaAs tunnel diodes for millimeter-wave detection”. 2015.
- [109] J. De Sousa, H. Detz, P. Klang, M. Nobile, A. Andrews, W. Schrenk, E. Gornik, G. Strasser, and J. Smoliner. “Nonparabolicity effects in InGaAs/GaAsSb double barrier resonant tunneling diodes”. *Journal of Applied Physics* 108.7 (2010).
- [110] J. Silvano De Sousa, H. Detz, P. Klang, E. Gornik, G. Strasser, and J. Smoliner. “Enhanced Rashba effect in transverse magnetic fields observed on InGaAs/GaAsSb resonant tunneling diodes at temperatures up to T=180 K”. *Applied Physics Letters* 99.15 (2011).
- [111] V. Aleshkin, A. Dubinov, K. Kudryavtsev, P. Yunin, M. Drozdov, O. Vikhrova, S. Nekorkin, and B. Zvonkov. “Stimulated emission from a metamorphic GaAsSb bulk layer on a GaAs substrate”. *Semiconductors* 50.5 (2016), pp. 586–589.
- [112] H. Detz, P. Klang, A. Andrews, W. Schrenk, and G. Strasser. “Si doping of MBE grown bulk GaAsSb on InP”. *Journal of Crystal Growth* 323.1 (2011), pp. 42–44.
- [113] J. Faist. “Wallplug efficiency of quantum cascade lasers: Critical parameters and fundamental limits”. *Applied Physics Letters* 90.25 (2007).

- 
- [114] P. Devlin, H. M. Heravi, and J. C. Woolley. “Electron Effective Mass Values in  $\text{GaAs}_x\text{Sb}_{1-x}$  Alloys.” *Canadian journal of physics* 59.7 (1981), pp. 939–944.
- [115] T. Zederbauer, A. M. Andrews, D. MacFarland, H. Detz, W. Schrenk, and G. Strasser. “Incorporation of Sb and As in MBE grown  $\text{GaAs}_x\text{Sb}_{1-x}$  layers”. *APL Materials* 5.3 (2017), p. 035501.
- [116] M. Brandstetter, M. Kainz, T. Zederbauer, M. Krall, S. Schönhuber, H. Detz, W. Schrenk, A. Andrews, G. Strasser, and K. Unterrainer. “InAs based terahertz quantum cascade lasers”. *Applied Physics Letters* 108.1 (2016).
- [117] P. Reininger, T. Zederbauer, B. Schwarz, H. Detz, D. MacFarland, A. Andrews, W. Schrenk, and G. Strasser. “InAs/AlAsSb based quantum cascade detector”. *Applied Physics Letters* 107.8 (2015).
- [118] K. Ohtani and H. Ohno. “InAs/AlSb quantum cascade lasers operating at  $10\ \mu\text{m}$ ”. *Applied Physics Letters* 82.7 (2003), pp. 1003–1005.
- [119] K. Ohtani, M. Beck, M. J. Süess, J. Faist, A. M. Andrews, T. Zederbauer, H. Detz, W. Schrenk, and G. Strasser. “Far-Infrared Quantum Cascade Lasers Operating in the AlAs Phonon Reststrahlen Band”. *ACS Photonics* 3.12 (2016), pp. 2280–2284.
- [120] C. A. Chang, R. Ludeke, L. Chang, and L. Esaki. “Molecular-beam epitaxy (MBE) of  $\text{In}_{1-x}\text{Ga}_x\text{As}$  and  $\text{GaSb}_{1-y}\text{As}_y$ ”. *Applied Physics Letters* 31.11 (1977), pp. 759–761.
- [121] Y. Nakata, T. Fujii, A. Sandhu, Y. Sugiyama, and E. Miyauchi. “Growth and characterization of  $\text{GaAs}_{0.5}\text{Sb}_{0.5}$  lattice-matched to InP by molecular beam epitaxy”. *Journal of Crystal Growth* 91.4 (1988), pp. 655–658.
- [122] J. Klem, R. Fischer, T. Drummond, H. Morkoc, and A. Cho. “Incorporation of Sb in  $\text{GaAs}_{1-x}\text{Sb}_x$  ( $x$  less than 0.15) by molecular beam epitaxy”. *Electronics Letters* 19.12 (1983), pp. 453–455.
- [123] G. Almuneau, E. Hall, S. Mathis, and L. Coldren. “Accurate control of Sb composition in AlGaAsSb alloys on InP substrates by molecular beam epitaxy”. *Journal of Crystal Growth* 208.1 (2000), pp. 113–116.
- [124] A. Semenov, V. Sorokin, V. Solov’ev, B. Mel’tser, and S. Ivanov. “Special Features of  $\text{Sb}_2$  and  $\text{Sb}_4$  Incorporation in MBE-Grown AlGaAsSb Alloys”. *Semiconductors* 38.3 (2004), pp. 266–272.

- [125] J. Klem, D. Huang, H. Morkoç, Y. Ihm, and N. Otsuka. “Molecular beam epitaxial growth and low-temperature optical characterization of  $\text{GaAs}_{0.5}\text{Sb}_{0.5}$  on  $\text{InP}$ ”. *Applied Physics Letters* 50.19 (1987), pp. 1364–1366.
- [126] A. Bosacchi, S. Franchi, P. Allegri, V. Avanzini, A. Baraldi, R. Magnanini, M. Berti, D. De Salvador, and S. Sinha. “Composition control of  $\text{GaSbAs}$  alloys”. *Journal of Crystal Growth* 201 (1999), pp. 858–860.
- [127] X. Sun, S. Wang, J. Hsu, R. Sidhu, X. Zheng, X. Li, J. Campbell, and A. Holmes Jr. “ $\text{GaAsSb}$ : A novel material for near infrared photodetectors on  $\text{GaAs}$  substrates”. *IEEE Journal on Selected Topics in Quantum Electronics* 8.4 (2002), pp. 817–822.
- [128] E. Selvig, B. Fimland, T. Skauli, and R. Haakenaasen. “Calibration of the arsenic mole fraction in MBE grown  $\text{GaAs}_y\text{Sb}_{1-y}$  and  $\text{Al}_x\text{Ga}_{1-x}\text{As}_y\text{Sb}_{1-y}$  ( $y < 0.2$ )”. *Journal of Crystal Growth* 227-228 (2001), pp. 562–565.
- [129] R. Kaspi, W. Cooley, and K. Evans. “In situ composition control of  $\text{III-As}_{1-x}\text{Sb}_x$  alloys during molecular beam epitaxy using line-of-sight mass spectrometry”. *Journal of Crystal Growth* 173 (1997), pp. 5–13.
- [130] R. Kaspi and K. Evans. “Sb-surface segregation and the control of compositional abruptness at the  $\text{GaAsSb}/\text{GaAs}$  interface”. *Journal of Crystal Growth* 175 (1997), pp. 838–843.
- [131] E. C. Larkins and J. James S. Harris. “Molecular Beam Epitaxy of High-Quality  $\text{GaAs}$  and  $\text{AlGaAs}$ ”. *Molecular Beam Epitaxy: Applications to Key Materials (Materials Science and Process Technology)*. Ed. by R. F. Farrow. William Andrew, 1996. Chap. 2, pp. 114–274.
- [132] E. Fitzgerald, G. Watson, R. Proano, D. Ast, P. Kirchner, G. Pettit, and J. Woodall. “Nucleation mechanisms and the elimination of misfit dislocations at mismatched interfaces by reduction in growth area”. *Journal of Applied Physics* 65.6 (1989), pp. 2220–2237.
- [133] E. A. Fitzgerald. “The effect of substrate growth area on misfit and threading dislocation densities in mismatched heterostructures”. *Journal of Vacuum Science and Technology B* 7.4 (1989), pp. 782–788.
- [134] K. Kudo, Y. Makita, I. Takayasu, T. Nomura, T. Kobayashi, T. Izumi, and T. Matsumori. “Photoluminescence spectra of undoped  $\text{GaAs}$  grown by molecular-beam epitaxy at very high and low substrate temperatures”. *Journal of Applied Physics* 59.3 (1986), pp. 888–891.

- 
- [135] O. Tejayadi, Y. Sun, J. Klem, R. Fischer, M. Klein, and H. Morkoç. “Effects of MBE growth conditions on carbon contamination in GaAs”. *Solid State Communications* 46.3 (1983), pp. 251–254.
  - [136] L. Gendron, M. Carras, A. Huynh, V. Ortiz, C. Koeniguer, and V. Berger. “Quantum cascade photodetector”. *Applied Physics Letters* 85.14 (2004), pp. 2824–2826.
  - [137] F. Giorgetta, E. Baumann, M. Graf, Q. Yang, C. Manz, K. Köhler, H. Beere, D. Ritchie, E. Linfield, A. Davies, Y. Fedoryshyn, H. Jäckel, M. Fischer, J. Faist, and D. Hofstetter. “Quantum cascade detectors”. *IEEE Journal of Quantum Electronics* 45.8 (2009), pp. 1039–1052.
  - [138] O. Baumgartner, Z. Stanojević, and H. Kosina. “Efficient simulation of quantum cascade lasers using the Pauli master equation” (2011), pp. 91–94.
  - [139] X. Marcadet, C. Becker, M. Garcia, I. Prévot, C. Renard, and C. Sirtori. “Material engineering for InAs/GaSb/AlSb quantum cascade light emitting devices”. *Journal of Crystal Growth* 251.1-4 (2003), pp. 723–728.
  - [140] H. Luo, S. R. Laframboise, Z. R. Wasilewski, G. C. Aers, H. C. Liu, and J. C. Cao. “Terahertz quantum-cascade lasers based on a three-well active module”. *Applied Physics Letters* 90.4, 041112 (2007).
  - [141] G. Turner and C. H.K. “Antimonide-Based Mid-Infrared Quantum-Well Diode Lasers”. *Antimonide-Related Strained-Layer Heterostructures (Optoelectronic Properties of Semiconductors and Superlattice)*. Ed. by M. Manasreh. CRC Press, 1997. Chap. 8, pp. 369–432.
  - [142] W. Yi, V. Narayanamurti, H. Lu, M. Scarpulla, and A. Gossard. “Probing semiconductor band structures and heterojunction interface properties with ballistic carrier emission: GaAs/Al<sub>x</sub>Ga<sub>1-x</sub>As as a model system”. *Physical Review B - Condensed Matter and Materials Physics* 81.23 (2010).
  - [143] W. Yi, V. Narayanamurti, H. Lu, M. Scarpulla, A. Gossard, Y. Huang, J.-H. Ryou, and R. Dupuis. “Bandgap and band offsets determination of semiconductor heterostructures using three-terminal ballistic carrier spectroscopy”. *Applied Physics Letters* 95.11 (2009).
  - [144] B. Fluegel, R. Kini, A. Ptak, D. Beaton, K. Alberi, and A. Mascarenhas. “Shubnikov-de Haas measurement of electron effective mass in GaAs<sub>1-x</sub>Bi<sub>x</sub>”. *Applied Physics Letters* 99.16 (2011).

- [145] J. Restorff, B. Houston, J. Burke, and R. Hayes. “Measurement of effective mass in  $\text{In}_{0.9}\text{Ga}_{0.1}\text{As}_{0.22}\text{P}_{0.78}$  by Shubnikov-de Haas oscillations”. *Applied Physics Letters* 32.3 (1978), pp. 189–190.
- [146] R. Shaw and D. Hill. “Shubnikov-de haas oscillations in n-type GaAs”. *Physical Review B* 1.2 (1970), pp. 658–662.

---

## Acronyms

---

**AFM** Atomic Force Microscopy. 48, 49, 59, 63, 65, 67–69, 72, 91, 95–97

**BEP** Beam Equivalent Pressure. 62, 68, 96

**cw** Continuous Wave. 19, 20

**EDX** Energy Dispersive X-Ray Spectroscopy. 50, 51, 67–72

**FIR** far-Infrared. 1, 2

**FWHM** full width at half maximum. 78, 85, 86

**HRXRD** High Resolution X-Ray Diffraction. viii, 37, 38, 41, 59, 63, 64, 67, 68, 71, 77, 81, 85, 91, 92, 95–97

**LPE** Liquid Phase Epitaxy. 60

**MBE** Molecular Beam Epitaxy. vii, 3, 21, 26–36, 41, 44, 48, 59–62, 75, 79–81, 88–93, 95, 96

**MIR** Mid-Infrared. 1, 2, 19, 75, 76, 93

**ML** Monolayer. 29

**MOCVD** Metal-Organic Chemical Vapor Deposition. 21

**NIR** near-Infrared. 1, 2

**PBN** Pyrolytic Boron Nitride. 26, 28, 32

**QCD** Quantum Cascade Detector. 89–91, 93, 97

**QCL** Quantum Cascade Laser. viii, 2, 3, 10, 13, 15, 16, 18–22, 53–57, 75, 77, 92–94, 97

**QE** Quantum Efficiency. 54, 55

**QMS** quatropole mass spectrometry. 87

**RHEED** Reflection High Energy Electron Diffraction. 28, 34, 44, 45, 48, 65–67

**RSM** Reciprocal Space Map. 85

**SEM** Scanning Electron Microscopy. 67, 69

**STM** Scanning Tunneling Microscopy. 34

**TE** Thermionic emission. 57–60

**TEM** Transmission electron microscopy. 87

**THz** Terahertz. viii, 2, 3, 19, 21, 53, 56, 57, 75, 77, 89, 92–95, 97

**UHV** Ultra High Vacuum. 26, 30

**VSP** Vienna Schrödinger Poisson Solver. 90



### Journal Articles

- [J42] H. Detz, D. MacFarland, T. Zederbauer, S. Lancaster, A. Andrews, W. Schrenk, and G. Strasser. “Growth rate dependence of boron incorporation into  $B_xGa_{1-x}As$  layers”. *Journal of Crystal Growth* (2017).
- [J41] E. Tütüncü, V. Kokoric, R. Szedlak, D. Macfarland, T. Zederbauer, H. Detz, A. Andrews, W. Schrenk, G. Strasser, and B. Mizaikoff. “Advanced gas sensors based on substrate-integrated hollow waveguides and dual-color ring quantum cascade lasers”. *Analyst* 141.22 (2016), pp. 6202–6207.
- [J40] H. Detz, M. Kriz, S. Lancaster, D. MacFarland, M. Schinnerl, T. Zederbauer, A. M. Andrews, W. Schrenk, and G. Strasser. “Lithography-free positioned GaAs nanowire growth with focused ion beam implantation of Ga”. *Journal of Vacuum Science & Technology B* 35.011803 (2017), pp. 1–5.
- [J39] S. Lancaster, M. Kriz, M. Schinnerl, D. MacFarland, T. Zederbauer, A. M. Andrews, W. Schrenk, G. Strasser, and H. Detz. “Focused ion beam implantation for the nucleation of self-catalyzed III-V nanowires”. *Microelectronic Engineering* 177 (2017), pp. 93–97.
- [J38] T. Zederbauer, A. M. Andrews, D. MacFarland, H. Detz, W. Schrenk, and G. Strasser. “Incorporation of Sb and As in MBE grown  $GaAs_xSb_{1-x}$  layers”. *APL Materials* 5.3 (2017), pp. 035501–1–035501–6.

- [J37] M. Brandstetter, M. A. Kainz, T. Zederbauer, M. Krall, S. Schönhuber, H. Detz, W. Schrenk, A. M. Andrews, G. Strasser, and K. Unterrainer. “InAs based terahertz quantum cascade lasers”. *Applied Physics Letters* 108.1 (2016), pp. 011109–1–011109–4.
- [J36] M. Brandstetter, S. Schönhuber, M. Krall, M. A. Kainz, H. Detz, T. Zederbauer, A. M. Andrews, G. Strasser, and K. Unterrainer. “Spectrally resolved far-fields of terahertz quantum cascade lasers”. *Optics Express* 24.22 (2016), pp. 25462–25470.
- [J35] K. Ohtani, M. Beck, M. Süess, J. Faist, A. Andrews, T. Zederbauer, H. Detz, W. Schrenk, and G. Strasser. “Far-Infrared Quantum Cascade Lasers Operating in the AlAs Phonon Reststrahlen Band”. *ACS Photonics* 3.12 (2016), pp. 2280–2284.
- [J34] R. Gansch, S. Kalchmair, P. Genevet, T. Zederbauer, H. Detz, W. Schrenk, F. Capasso, M. Loncar, and G. Strasser. “Measurement of bound states in the continuum by a detector embedded in a photonic crystal”. *Light-Science & Applications* 5.e16147 (2016), pp. 1–7.
- [J33] A. Harrer, B. Schwarz, S. Schuler, P. Reininger, A. Wirthmüller, H. Detz, D. MacFarland, T. Zederbauer, A. M. Andrews, M. Rothermund, H. Oppermann, W. Schrenk, and G. Strasser. “4.3  $\mu\text{m}$  quantum cascade detector in pixel configuration”. *Optics Express* 24.16 (2016), pp. 17041–17049.
- [J32] A. Harrer, R. Szedlak, B. Schwarz, H. Moser, T. Zederbauer, D. MacFarland, H. Detz, A. M. Andrews, W. Schrenk, B. Lendl, and G. Strasser. “Mid-infrared surface transmitting and detecting quantum cascade device for gas-sensing”. *Scientific Reports* 6.21795 (2016), pp. 1–6.
- [J31] K. Ohtani, M. Beck, M. J. Süess, J. Faist, A. M. Andrews, T. Zederbauer, H. Detz, W. Schrenk, and G. Strasser. “Far-Infrared Quantum Cascade Lasers Operating in the AlAs Phonon Reststrahlen Band”. *ACS Photonics* 3.12 (2016), pp. 2280–2284.
- [J30] R. Szedlak, A. Harrer, M. Holzbauer, B. Schwarz, J. P. Waclawek, D. MacFarland, T. Zederbauer, H. Detz, A. M. Andrews, W. Schrenk, B. Lendl, and G. Strasser. “Remote Sensing with Commutable Monolithic Laser and Detector”. *ACS Photonics* 3 (2016), pp. 1794–1798.

- 
- [J29] R. Szedlak, M. Holzbauer, P. Reininger, D. MacFarland, T. Zederbauer, H. Detz, A. M. Andrews, W. Schrenk, and G. Strasser. “Ring quantum cascade lasers with grating phase shifts and a light collimating dielectric metamaterial for enhanced infrared spectroscopy”. *Vibrational Spectroscopy* 84 (2016), pp. 101–105.
- [J28] E. Tütüncü, V. Kokoric, R. Szedlak, D. MacFarland, T. Zederbauer, H. Detz, A. M. Andrews, W. Schrenk, G. Strasser, and B. Mizaikoff. “Advanced gas sensors based on substrate-integrated hollow waveguides and dual-color ring quantum cascade lasers”. *Analyst* 141 (2016), pp. 6202–6207.
- [J27] T. Zederbauer, A. M. Andrews, D. MacFarland, H. Detz, W. Schrenk, and G. Strasser. “Enhanced Crystal Quality of  $\text{Al}_x\text{In}_{1-x}\text{As}_y\text{Sb}_{1-y}$  for Terahertz Quantum Cascade Lasers”. *Photonics* 3.2 (2016), pp. 1–9.
- [J26] H. Detz, M. Kriz, D. MacFarland, S. Lancaster, T. Zederbauer, M. Capriotti, A. M. Andrews, W. Schrenk, and G. Strasser. “Nucleation of Ga droplets on Si and  $\text{SiO}_x$  surfaces”. *Nanotechnology* 26.31 (2015), pp. 3156011–3156018.
- [J25] P. Reininger, B. Schwarz, R. Gansch, H. Detz, D. MacFarland, T. Zederbauer, A. M. Andrews, W. Schrenk, and G. Strasser. “Quantum cascade detector utilizing the diagonal-transition scheme for high quality cavities”. *Optics Express* 23.5 (2015), pp. 6283–6291.
- [J24] P. Reininger, T. Zederbauer, B. Schwarz, H. Detz, D. MacFarland, A. M. Andrews, W. Schrenk, and G. Strasser. “InAs/AlAsSb based quantum cascade detector”. *Applied Physics Letters* 107.081107 (2015), pp. 081107–1–081107–3.
- [J23] D. Ristanic, B. Schwarz, P. Reininger, H. Detz, T. Zederbauer, A. M. Andrews, W. Schrenk, and G. Strasser. “Monolithically integrated mid-infrared sensor using narrow mode operation and temperature feedback”. *Applied Physics Letters* 106.041101 (2015), pp. 041101–1–041101–4.
- [J22] B. Schwarz, D. Ristanic, P. Reininger, T. Zederbauer, D. MacFarland, H. Detz, A. M. Andrews, W. Schrenk, and G. Strasser. “High performance bi-functional quantum cascade laser and detector”. *Applied Physics Letters* 107.071104 (2015), pp. 071104–1–071104–4.
- [J21] R. Szedlak, M. Holzbauer, D. MacFarland, T. Zederbauer, H. Detz, A. M. Andrews, C. Schwarzer, W. Schrenk, and G. Strasser. “The influence of whispering gallery modes on the far field of ring lasers”. *Scientific Reports* 5.16668 (2015), pp. 1–8.

- [J20] S. Ahn, C. Schwarzer, T. Zederbauer, D. MacFarland, H. Detz, A. M. Andrews, W. Schrenk, and G. Strasser. “High-power, low-lateral divergence broad area quantum cascade lasers with a tilted front facet”. *Applied Physics Letters* 104 (2014), pp. 0511011–0511014.
- [J19] H. Detz, J. Silvano de Sousa, H. A. Leonhardt, P. Klang, T. Zederbauer, A. M. Andrews, W. Schrenk, J. Smoliner, and G. Strasser. “InGaAs/GaAsSb based two-dimensional electron gases”. *Journal of Vacuum Science & Technology B* 32.02C104 (2014), pp. 02C104–1–02C104–6.
- [J18] A. Harrer, B. Schwarz, R. Gansch, P. Reininger, H. Detz, T. Zederbauer, A. M. Andrews, W. Schrenk, and G. Strasser. “Plasmonic lens enhanced mid-infrared quantum cascade detector”. *Applied Physics Letters* 105.171112 (2014), pp. 1–4.
- [J17] P. Reininger, B. Schwarz, H. Detz, D. MacFarland, T. Zederbauer, A. M. Andrews, W. Schrenk, O. Baumgartner, H. Kosina, and G. Strasser. “Diagonal-transition quantum cascade detector”. *Applied Physics Letters* 105.091108 (2014), pp. 1–4.
- [J16] R. Szedlak, C. Schwarzer, T. Zederbauer, H. Detz, A. M. Andrews, W. Schrenk, and G. Strasser. “Grating-based far field modifications of ring quantum cascade lasers”. *Optics Express* 22.13 (2014), pp. 15829–15836.
- [J15] R. Szedlak, C. Schwarzer, T. Zederbauer, H. Detz, A. M. Andrews, W. Schrenk, and G. Strasser. “On-chip focusing in the mid-infrared: Demonstrated with ring quantum cascade lasers”. *Applied Physics Letters* 104 (2014), pp. 151105.1–4.
- [J14] S. Ahn, C. Schwarzer, T. Zederbauer, H. Detz, A. M. Andrews, W. Schrenk, and G. Strasser. “Enhanced light output power of quantum cascade lasers from a tilted front facet”. *Optics Express* 21.13 (2013), pp. 15869–15877.
- [J13] M. Brandstetter, C. Deutsch, M. Krall, H. Detz, D. MacFarland, T. Zederbauer, A. M. Andrews, W. Schrenk, G. Strasser, and K. Unterrainer. “High power terahertz quantum cascade lasers with symmetric wafer bonded active regions”. *Applied Physics Letters* 103.17 (2013), pp. 171113–1–171113–5.
- [J12] C. Deutsch, H. Detz, M. Krall, M. Brandstetter, T. Zederbauer, A. M. Andrews, W. Schrenk, G. Strasser, and K. Unterrainer. “Dopant migration effects in terahertz quantum cascade lasers”. *Applied Physics Letters* 102.201102 (2013), pp. 201102–1–201102–4.

- 
- [J11] C. Deutsch, H. Detz, T. Zederbauer, A. M. Andrews, P. Klang, T. Kubis, G. Klimeck, M. E. Schuster, W. Schrenk, G. Strasser, and K. Unterrainer. “Probing scattering mechanisms with symmetric quantum cascade lasers”. *Optics Express* 21.6 (2013), pp. 7209–7215.
- [J10] C. Deutsch, H. Detz, T. Zederbauer, M. Krall, M. Brandstetter, A. M. Andrews, P. Klang, W. Schrenk, G. Strasser, and K. Unterrainer. “InGaAs/GaAsSb/InP terahertz quantum cascade lasers”. *Journal of Infrared, Millimeter, and Terahertz Waves* 34.5-6 (2013), pp. 374–385.
- [J9] M. Krall, M. Brandstetter, C. Deutsch, H. Detz, T. Zederbauer, A. M. Andrews, W. Schrenk, G. Strasser, and K. Unterrainer. “Towards nanowire-based terahertz quantum cascade lasers: prospects and technological challenges”. *Proceedings of SPIE* 8640.864018 (2013), pp. 864018–1–864018–7.
- [J8] S. Maëro, L.-A. de Vaultier, Y. Guldner, C. Deutsch, M. Krall, T. Zederbauer, G. Strasser, and K. Unterrainer. “Magnetic-field assisted performance of InGaAs/GaAsSb terahertz quantum cascade lasers”. *Applied Physics Letters* 103.5 (2013), pp. 051116–1–051116–4.
- [J7] P. Reininger, B. Schwarz, A. Harrer, T. Zederbauer, H. Detz, A. M. Andrews, R. Gansch, W. Schrenk, and G. Strasser. “Photonic crystal slab quantum cascade detector”. *Applied Physics Letters* 103 (2013), pp. 2411031–2411034.
- [J6] B. Schwarz, P. Reininger, H. Detz, T. Zederbauer, A. M. Andrews, W. Schrenk, and G. Strasser. “Monolithically Integrated Mid-Infrared Quantum Cascade Laser and Detector”. *Sensors* 13 (2013), pp. 2196–2205.
- [J5] C. Schwarzer, R. Szedlak, S. Ahn, T. Zederbauer, H. Detz, A. M. Andrews, W. Schrenk, and G. Strasser. “Linearly polarized light from substrate emitting ring cavity quantum cascade lasers”. *Applied Physics Letters* 103 (2013), pp. 0811011–0811013.
- [J4] S. Ahn, C. Schwarzer, S. Kalchmair, R. Gansch, D. Ristanic, T. Zederbauer, P. Reininger, H. Detz, A. M. Andrews, W. Schrenk, and G. Strasser. “Facet Reflectivity Reduction of Quantum Cascade Lasers by Tilted Facets”. *Proceedings of SPIE* 8432 (2012), pp. 1–2.
- [J3] S. Kalchmair, R. Gansch, S. Ahn, A. M. Andrews, H. Detz, T. Zederbauer, E. Mujagic, P. Reininger, G. Lasser, W. Schrenk, and G. Strasser. “Detectivity enhancement in quantum well infrared photodetectors utilizing a photonic crystal slab resonator”. *Optics Express* 20.5 (2012), pp. 5622–5628.

- [J2] P. Reininger, S. Kalchmair, R. Gansch, A. M. Andrews, H. Detz, T. Zederbauer, S. Ahn, W. Schrenk, and G. Strasser. “Optimized Photonic Crystal Design for Quantum Well Infrared Photodetectors”. *Proceedings of SPIE* 8425 (2012), pp. 842501–842504.
- [J1] B. Schwarz, P. Reininger, H. Detz, T. Zederbauer, A. M. Andrews, S. Kalchmair, W. Schrenk, O. Baumgartner, H. Kosina, and G. Strasser. “A bi-functional quantum cascade device for same-frequency lasing and detection”. *Applied Physics Letters* 101 (2012), pp. 1911091–1911094.

## Oral Presentations

- [O101] A. Harrer, B. Schwarz, S. Schuler, P. Reininger, A. Wirthmüller, H. Detz, D. MacFarland, T. Zederbauer, A. M. Andrews, M. Rothermund, H. Oppermann, W. Schrenk, and G. Strasser. “Quantum cascade detector at  $4.3\mu\text{m}$  wavelength in pixel array configuration”. *Conference Proceedings. SPIE Photonics West 2017*, San Francisco. 2017, p. 320.
- [O100] A. Harrer, B. Schwarz, R. Szedlak, M. Holzbauer, D. Ristanic, H. Detz, D. MacFarland, T. Zederbauer, A. M. Andrews, W. Schrenk, and G. Strasser. “Quantum cascade structures for sensing applications”. Daylight Solution Seminar, San Diego; 2017-02-10. 2017.
- [O99] R. Szedlak, A. Harrer, B. Schwarz, M. Holzbauer, J. P. Waclawek, D. MacFarland, T. Zederbauer, H. Detz, A. M. Andrews, W. Schrenk, B. Lendl, and G. Strasser. “Remote gas sensing with quantum cascade systems”. eingeladen; Nano and Photonics, Mauterndorf. 2017.
- [O98] A. M. Andrews, T. Zederbauer, D. MacFarland, H. Detz, W. Schrenk, M. Brandstetter, M. A. Kainz, M. Krall, S. Schönhuber, K. Unterrainer, and G. Strasser. “Growth of  $\text{Al}_x\text{In}_{1-x}\text{As}_y\text{Sb}_{1-y}$  for InAs-based THz Quantum Cascade Lasers”. *Technical Program. 19th International Conference on Molecular Beam Epitaxy*, Montpellier, Frankreich. 2016, p. 32.
- [O97] A. M. Andrews, T. Zederbauer, D. MacFarland, H. Detz, W. Schrenk, M. Brandstetter, M. A. Kainz, M. Krall, S. Schönhuber, K. Unterrainer, and G. Strasser. “Growth of lattice-matched InAs-based intersubband devices”. *German MBE Workshop. German MBE Workshop*, Garching, Deutschland. 2016, p. 27.

- [O96] M. Brandstetter, M. Krall, M. A. Kainz, S. Schönhuber, C. Deutsch, T. Zederbauer, A. M. Andrews, G. Strasser, and K. Unterrainer. “THz Quantum Cascade Lasers with low effective mass active region”. *IEEE Photonics Conference (IPC) 2016*. eingeladen; IEEE Photonics Conference, Waikoloa, Hawaii, USA. 2016, pp. 70–71.
- [O95] A. Harrer, B. Schwarz, P. Reininger, R. Szedlak, T. Zederbauer, H. Detz, D. MacFarland, A. M. Andrews, W. Schrenk, and G. Strasser. “An optimized bi-functional material for integrated mid-infrared quantum cascade based sensors”. *digital digest*. Photonics West 2016, San Francisco, California, USA. 2016.
- [O94] A. Harrer, B. Schwarz, R. Szedlak, D. Ristanic, H. Detz, A. M. Andrews, T. Zederbauer, D. MacFarland, W. Schrenk, and G. Strasser. “Quantum Cascade devices: from discrete to integrated systems”. *Conference Book MIOMD-XIII*. eingeladen; 13th International Conference on Mid-IR Optoelectronics: Material and Devices (MIOMD-XIII), Beijing. 2016, p. 62.
- [O93] A. Harrer, R. Szedlak, B. Schwarz, H. Moser, T. Zederbauer, D. MacFarland, H. Detz, A. M. Andrews, B. Lendl, and G. Strasser. “Mid-infrared bi-functional quantum cascade sensor for long interaction regions”. *Conference Documentation*. International Conference Functional Integrated nano Systems, Graz. 2016.
- [O92] M. Holzbauer, R. Szedlak, D. MacFarland, T. Zederbauer, H. Detz, A. M. Andrews, W. Schrenk, M. P. Semtsiv, W. T. Masselink, and G. Strasser. “Ring Quantum Cascade Lasers for Chemical Sensing and Spectroscopic Applications”. Vienna Young Scientists Symposium - VSS 2016, Wien. 2016, p. 124.
- [O91] M. Holzbauer, R. Szedlak, D. MacFarland, T. Zederbauer, H. Detz, A. M. Andrews, W. Schrenk, and G. Strasser. “Ring quantum cascade lasers with metal-covered distributed feedback gratings”. *Proceedings of the ICPS 2016*. 33<sup>rd</sup> International Conference on the Physics of Semiconductors (ICPS2016), Beijing. 2016, p. 353.
- [O90] M. Holzbauer, R. Szedlak, D. MacFarland, T. Zederbauer, H. Detz, A. M. Andrews, W. Schrenk, and G. Strasser. “Sub-threshold measurements of the whispering gallery modes in ring quantum cascade lasers”. *Conference Book*. Annual Meeting of the Austrian Physical Society, Wien. 2016, pp. 160–161.
- [O89] M. A. Kainz, M. Brandstetter, T. Zederbauer, M. Krall, S. Schönhuber, H. Detz, W. Schrenk, A. M. Andrews, T. Grange, G. Strasser, and K. Unterrainer. “InAs based Terahertz Quantum Cascade Lasers”. *Proceedings of the ICPS 2016*. 33<sup>rd</sup>

- International Conference on the Physics of Semiconductors (ICPS2016), Beijing, China. 2016.
- [O88] S. Kalchmair, R. Gansch, P. Genevet, T. Zederbauer, D. MacFarland, H. Detz, A. M. Andrews, W. Schrenk, G. Strasser, F. Capasso, and M. Loncar. “In-situ measurement of bound states in the continuum in photonic crystal slabs”. *Proceedings of SPIE*. Photonic Crystal Materials and Devices XII, Brüssel. 9885: SPIE, 2016, pp. 9885–21.
  - [O87] M. Krall, M. A. Kainz, M. Brandstetter, C. Deutsch, S. Schönhuber, D. MacFarland, T. Zederbauer, H. Detz, A. M. Andrews, W. Schrenk, G. Strasser, and K. Unterrainer. “High Performance InGaAs-based Terahertz Quantum Cascade Lasers”. *Technical Digest*. International Quantum Cascade Lasers School and Workshop (IQCLSW 2016), Cambridge. 2016.
  - [O86] S. Lancaster, H. Detz, M. Kriz, D. MacFarland, M. Schinnerl, T. Zederbauer, A. M. Andrews, W. Schrenk, and G. Strasser. “Focused ion beam implantation for the nucleation of self-catalyzed III-V nanowires”. *Technical digest*. 42nd International Conference on Nano Engineering, MNE 2016, Wien. 2016.
  - [O85] P. Reininger, T. Zederbauer, B. Schwarz, H. Detz, D. MacFarland, A. M. Andrews, W. Schrenk, and G. Strasser. “A low effective mass materialsystem for quantum cascade detectors”. *digital digest*. eingeladen; Photonics West, San Francisco, USA. 2016.
  - [O84] G. Strasser, B. Schwarz, R. Szedlak, A. Harrer, H. Detz, A. M. Andrews, T. Zederbauer, D. MacFarland, and W. Schrenk. “Quantum cascade detectors and monolithically integrated sensing devices”. *FLAIR 2016*. eingeladen; FLAIR 2016, Aix-les-Bains. 2016, p. 165.
  - [O83] R. Szedlak, A. Harrer, M. Holzbauer, B. Schwarz, D. MacFarland, T. Zederbauer, H. Detz, A. M. Andrews, W. Schrenk, and G. Strasser. “Mid-infrared ring lasers for sensing applications”. *Europhysics Conference Abstract Volume 40 B*. 7th EPS-QEOD Europhoton Conference (EUROPHOTON 2016), Wien. 2016, p. 52.
  - [O82] R. Szedlak, A. Harrer, M. Holzbauer, B. Schwarz, J. P. Wacławek, H. Moser, D. MacFarland, T. Zederbauer, H. Detz, A. M. Andrews, W. Schrenk, B. Lendl, and G. Strasser. “Compact mid-IR sensors based on bi-functional and commutable semiconductor lasers and detectors on the same chip”. *digital digest*. eingeladen; 3<sup>rd</sup> International WORKshop on Infrared Technologies, Olching. 2016.



- [O81] R. Szedlak, A. Harrer, B. Schwarz, M. Holzbauer, H. Moser, D. MacFarland, T. Zederbauer, H. Detz, A. M. Andrews, W. Schrenk, B. Lendl, and G. Strasser. “Highly Integrated Gas Sensors based on Bi-functional Quantum Cascade Structures”. *CLEO:2016 Laser Science to Photonic Applications*. CLEO 2016, San Jose. 2016, p. 234.
- [O80] R. Szedlak, A. Harrer, B. Schwarz, M. Holzbauer, J. P. Waclawek, D. MacFarland, T. Zederbauer, H. Detz, A. M. Andrews, W. Schrenk, B. Lendl, and G. Strasser. “Remote gas sensing with commutable quantum cascade laser and detector on the same Chip”. *Technical Digest*. eingeladen; International Quantum Cascade Lasers School and Workshop (IQCLSW 2016), Cambridge. 2016.
- [O79] R. Szedlak, T. Hisch, M. Holzbauer, D. MacFarland, T. Zederbauer, H. Detz, A. M. Andrews, W. Schrenk, S. Rotter, and G. Strasser. “On-chip Generation of Infrared Orbital Angular Momentum Beams using a Dielectric Metamaterial”. *CLEO:2016 Laser Science to Photonic Applications*. CLEO 2016, San Jose. 2016, p. 181.
- [O78] A. Harrer, B. Schwarz, R. Szedlak, M. Holzbauer, T. Zederbauer, H. Detz, A. M. Andrews, D. MacFarland, W. Schrenk, H. Moser, J. P. Waclawek, B. Lendl, and G. Strasser. “Mid-infrared sensing based on quantum cascade structures”. NextLite Workshop, Wien. 2016.
- [O77] L. Prochaska, D. MacFarland, A. M. Andrews, M. Bonta, H. Detz, W. Schrenk, T. Zederbauer, A. Limbeck, G. Strasser, J. Bernardi, and S. Paschen. “Film growth of the heavy fermion compound  $\text{YbRh}_2\text{Si}_2$  by molecular beam epitaxy”. German MBE Workshop 2016, Garching, Deutschland. 2016.
- [O76] B. Schwarz, D. Ristanic, P. Reininger, W. Schrenk, H. Detz, T. Zederbauer, A. M. Andrews, D. MacFarland, and G. Strasser. “QCL based liquid sensing 2.0: A single chip solution”. eingeladen; SCIX 2016, Minneapolis. 2016.
- [O75] A. M. Andrews, D. MacFarland, M. Krall, T. Zederbauer, H. Detz, W. Schrenk, M. Brandstetter, C. Deutsch, K. Unterrainer, and G. Strasser. “AlGaInAs barriers for InP-based Terahertz Quantum Cascade Lasers”. *Book of Abstracts*. European Molecular Beam Epitaxy Workshop, Canazei, Italien. 2015, pp. 1–2.
- [O74] M. Brandstetter, M. Krall, C. Deutsch, S. Schönhuber, D. MacFarland, H. Detz, T. Zederbauer, A. M. Andrews, W. Schrenk, G. Strasser, and K. Unterrainer. “Alternative Material Systems for High Performance THz Quantum Cascade Lasers”. *Technical Digest*. ITQW, Wien. 2015.

- [O73] H. Detz, M. Kriz, S. Lancaster, D. MacFarland, T. Zederbauer, A. M. Andrews, W. Schrenk, and G. Strasser. “Nucleation Of Nano-Scale Gallium Droplets Silicon Surfaces”. *Book of Abstracts*. European Molecular Beam Epitaxy Workshop, Canazei, Italien. 2015, pp. 1–2.
- [O72] M. Krall, D. Bachmann, C. Deutsch, M. Brandstetter, H. Detz, T. Zederbauer, D. MacFarland, A. M. Andrews, W. Schrenk, G. Strasser, and K. Unterrainer. “All-electrical thermal characterization of terahertz quantum cascade lasers”. *Technical Digest*. ITQW, Wien. 2015, pp. 34–35.
- [O71] M. Krall, M. Brandstetter, C. Deutsch, H. Detz, T. Zederbauer, A. M. Andrews, W. Schrenk, G. Strasser, and K. Unterrainer. “Towards nanowire-based terahertz quantum cascade lasers”. *Book of Abstracts*. Towards Nanowire-Based Terahertz Quantum Cascade Lasers, Bad Honnef, Germany. 2015.
- [O70] P. Reininger, T. Zederbauer, B. Schwarz, H. Detz, D. MacFarland, A. M. Andrews, W. Schrenk, and G. Strasser. “InAs/AlAsSb for quantum cascade detectors”. *ITQW 2015*. ITQW, Wien. 2015, pp. 86–87.
- [O69] D. Ristanic, B. Schwarz, P. Reininger, H. Detz, A. M. Andrews, W. Schrenk, T. Zederbauer, D. MacFarland, and G. Strasser. “Monolithical Absorption Sensor Based on Bi-functional Quantum Cascade Structures”. *Abstracts in Laser Science to Photonic Applications*. CLEO 2015, San Jose, USA. OSA Publishing, 2015.
- [O68] D. Ristanic, B. Schwarz, P. Reininger, H. Detz, A. M. Andrews, W. Schrenk, T. Zederbauer, D. MacFarland, and G. Strasser. “Quantum Cascade Lasers and Detectors: Monolithically integrated Nanosensors”. *Book of Abstracts*. Nano and Photonics, Mauterndorf. 2015.
- [O67] B. Schwarz, A. Harrer, D. Ristanic, P. Reininger, H. Detz, T. Zederbauer, A. M. Andrews, W. Schrenk, and G. Strasser. “Bi-functional quantum cascade laser/ detectors: From design to applications”. *ITQW 2015*. ITQW, Wien. 2015, pp. 104–105.
- [O66] R. Szedlak, M. Holzbauer, D. MacFarland, T. Zederbauer, H. Detz, A. M. Andrews, W. Schrenk, and G. Strasser. “Using the far field of ring lasers to characterize their whispering gallery modes”. *Gemeinsame Jahrestagung in Wien - ÖPG Tagungsband*. Gemeinsame Jahrestagung 2015 der ÖPG, SPS, ÖGA und SSAA in Wien, Wien. 2015, p. 39.

- [O65] A. Harrer, P. Reininger, R. Gansch, B. Schwarz, D. MacFarland, T. Zederbauer, H. Detz, A. M. Andrews, W. Schrenk, O. Baumgartner, H. Kosina, and G. Strasser. “Quantum Cascade Detectors for Sensing Applications”. ICAVS8, Wien. 2015.
- [O64] A. Harrer, B. Schwarz, R. Szedlak, J. P. Waclawek, H. Moser, D. MacFarland, T. Zederbauer, H. Detz, A. M. Andrews, W. Schrenk, B. Lendl, and G. Strasser. “A bi-functional surface emitting and detecting mid-infrared device for sensing applications”. ÖPG-Jahrestagung, Wien. 2015.
- [O63] A. Harrer, R. Szedlak, M. Holzbauer, B. Schwarz, H. Moser, E. Mujagic, D. MacFarland, T. Zederbauer, H. Detz, A. M. Andrews, W. Schrenk, B. Lendl, and G. Strasser. “Monolithic integrated on-chip sensing utilizing plasmonics”. 1st Next-Lite Workshop, Hirschwang an der Rax. 2015.
- [O62] M. Holzbauer, R. Szedlak, D. MacFarland, T. Zederbauer, H. Detz, A. M. Andrews, W. Schrenk, and G. Strasser. “Light extraction from ring quantum cascade lasers”. eingeladen; Nanoforum 2015, Linz. 2015.
- [O61] M. Holzbauer, R. Szedlak, D. MacFarland, T. Zederbauer, H. Detz, A. M. Andrews, W. Schrenk, and G. Strasser. “Thermal Management in Ring Quantum Cascade Lasers”. ÖPG-Jahrestagung, Wien. 2015.
- [O60] P. Reininger, B. Schwarz, A. Harrer, T. Zederbauer, H. Detz, A. M. Andrews, R. Gansch, W. Schrenk, and G. Strasser. “High-responsivity photovoltaic inter-subband detectors”. Photonics West, San Francisco, USA. 2015.
- [O59] G. Strasser, D. Ristanic, B. Schwarz, P. Reininger, H. Detz, A. M. Andrews, T. Zederbauer, D. MacFarland, and W. Schrenk. “A Mid-Infrared On-Chip Sensor Array Based on Bi-functional Quantum Cascade Structures and Plasmonics”. eingeladen; ICAVS8, Wien. 2015.
- [O58] R. Szedlak, A. Harrer, M. Holzbauer, B. Schwarz, H. Moser, E. Mujagic, C. Deutsch, D. MacFarland, T. Zederbauer, H. Detz, A. M. Andrews, W. Schrenk, K. Unterrainer, B. Lendl, and G. Strasser. “Infrared and terahertz spectroscopy with ring quantum cascade lasers”. German THz Conference 2015, Dresden. 2015.
- [O57] R. Szedlak, M. Holzbauer, D. MacFarland, T. Zederbauer, H. Detz, A. M. Andrews, W. Schrenk, and G. Strasser. “Probing whispering gallery modes in ring lasers”. 1st Next-Lite Workshop, Hirschwang an der Rax. 2015.

- [O56] R. Szedlak, M. Holzbauer, D. MacFarland, T. Zederbauer, H. Detz, A. M. Andrews, W. Schrenk, and G. Strasser. “Ring Quantum Cascade Lasers for Infrared Spectroscopy”. ICAVS8, Wien. 2015.
- [O55] H. Detz, C. Deutsch, T. Zederbauer, D. MacFarland, M. Krall, M. Brandstetter, A. M. Andrews, W. Schrenk, K. Unterrainer, and G. Strasser. “Material Analysis and Optimization using Symmetric THz Quantum Cascade Lasers”. *Compound Semiconductor Week*. eingeladen; International Symposium on Compound Semiconductors (ISCS), Montpellier, Frankreich. 2014, pp. 1–3.
- [O54] H. Detz, J. Silvano de Sousa, H. A. Leonhardt, P. Klang, T. Zederbauer, A. M. Andrews, W. Schrenk, J. Smoliner, and G. Strasser. “Two-Dimensional Electron Gases Based on InGaAs/GaAsSb Heterostructures”. *Compound Semiconductor Week*. International Symposium on Compound Semiconductors (ISCS), Montpellier, Frankreich. 2014, pp. 1–3.
- [O53] K. Unterrainer, C. Deutsch, M. Brandstetter, M. Krall, H. Detz, T. Zederbauer, A. M. Andrews, W. Schrenk, and G. Strasser. “High Power THz Quantum Cascade Lasers Based on Novel Materials and Designs”. *IPC 2014*. eingeladen; IEEE Photonics Conference, San Diego. 2014.
- [O52] A. M. Andrews, M. Brandstetter, C. Deutsch, M. Krall, H. Detz, D. MacFarland, T. Zederbauer, W. Schrenk, G. Strasser, and K. Unterrainer. “Increasing THz QCL active region thickness by wafer bonding”. WOCSEMMAD, San Antonio, TX, USA. 2014.
- [O51] C. Deutsch, M. Brandstetter, M. Krall, T. Zederbauer, G. Strasser, and K. Unterrainer. “Novel THz quantum cascade laser active materials and designs”. eingeladen; Photonics West, San Francisco, USA. 2014.
- [O50] A. Harrer, P. Reininger, B. Schwarz, R. Gansch, S. Kalchmair, H. Detz, T. Zederbauer, D. MacFarland, A. M. Andrews, W. Schrenk, O. Baumgartner, H. Kosina, and G. Strasser. “Advances in Quantum Cascade Detector Design”. 4th International Nanophotonics Meeting 2014, Igls. 2014.
- [O49] M. Holzbauer, R. Szedlak, C. Schwarzer, D. MacFarland, T. Zederbauer, H. Detz, A. M. Andrews, W. Schrenk, and G. Strasser. “Mid-infrared Ring Cavities”. 4th International Nanophotonics Meeting 2014, Igls. 2014.

- [O48] P. Reininger, B. Schwarz, A. Harrer, T. Zederbauer, H. Detz, A. M. Andrews, R. Gansch, W. Schrenk, and G. Strasser. “Room temperature quantum cascade detector”. International Quantum Cascade Lasers School & Workshop (IQCLSW 2014), Bari. 2014.
- [O47] H. Detz, C. Deutsch, T. Zederbauer, P. Klang, A. M. Andrews, M. Schuster, W. Schrenk, K. Unterrainer, and G. Strasser. “Symmetric THz Quantum Cascade Lasers as a Tool for Growth Optimization”. *Book of Abstracts*. European Molecular Beam Epitaxy Workshop, Levi, Finland. 2013, p. 73.
- [O46] C. Deutsch, M. Krall, H. Detz, M. Brandstetter, T. Zederbauer, A. M. Andrews, G. Strasser, and K. Unterrainer. “High Performance InGaAs/InP-based Terahertz Quantum Cascade Lasers and Growth-related Asymmetries”. *Technical Digest*. ITQW, New York, USA. 2013.
- [O45] M. Krall, M. Brandstetter, C. Deutsch, H. Detz, T. Zederbauer, A. M. Andrews, W. Schrenk, G. Strasser, and K. Unterrainer. “Fabrication and Characterization of Terahertz Emitting GaAs/AlGaAs Micropillar Quantum Cascade Structures in a Double Metal Waveguide”. *Conference Digest*. CLEO Europe 2013, Munich. 2013.
- [O44] M. Krall, M. Brandstetter, C. Deutsch, T. Grange, H. Detz, T. Zederbauer, D. MacFarland, A. M. Andrews, W. Schrenk, G. Strasser, and K. Unterrainer. “From photonic crystal to micropillar terahertz quantum cascade lasers and recent progress towards nanowire-based devices”. *Technical Digest*. Joint Annual Meeting of ÖPG, SPG, ÖGAA und SGAA 2013, Linz. 2013.
- [O43] A. M. Andrews, M. Nobile, C. Deutsch, H. Detz, T. Zederbauer, D. MacFarland, W. Schrenk, K. Unterrainer, and G. Strasser. “InGaAs/GaAsSb Material System for Quantum Cascade Lasers”. eingeladen; 3<sup>rd</sup> International Nanophotonics Meeting 2013, Salzburg. 2013.
- [O42] M. Brandstetter, C. Deutsch, M. Krall, H. Detz, D. MacFarland, T. Zederbauer, A. M. Andrews, W. Schrenk, G. Strasser, and K. Unterrainer. “High performance THz QCLs with wafer bonded active regions”. 3<sup>rd</sup> International Nanophotonics Meeting 2013, Salzburg. 2013.
- [O41] H. Detz, C. Deutsch, T. Zederbauer, D. MacFarland, M. Krall, M. Brandstetter, A. M. Andrews, W. Schrenk, K. Unterrainer, and G. Strasser. “Growth Optimization Using Symmetric Quantum Cascade Laser Active Regions”. North American Conf. on Molecular Beam Epitaxy (NAMBE), Banff, Canada. 2013.

- [O40] A. Harrer, B. Schwarz, P. Reininger, R. Gansch, T. Zederbauer, A. M. Andrews, S. Kalchmair, W. Schrenk, O. Baumgartner, Z. Stanojevic, H. Kosina, and G. Strasser. “Intersubband Detectors”. 3<sup>rd</sup> International Nanophotonics Meeting 2013, Salzburg. 2013.
- [O39] M. Krall, M. Brandstetter, C. Deutsch, H. Detz, T. Zederbauer, A. M. Andrews, W. Schrenk, G. Strasser, and K. Unterrainer. “Towards nanowire-based terahertz quantum cascade lasers: prospects and technological challenges”. SPIE Photonics West 2013, San Francisco. 2013.
- [O38] D. MacFarland, C. Deutsch, H. Detz, M. Krall, M. Brandstetter, T. Zederbauer, A. M. Andrews, K. Unterrainer, and G. Strasser. “Effects of MBE Growth Asymmetries in Symmetric THz Quantum Cascade Lasers”. International Terahertz Conference, Villach. 2013.
- [O37] P. Reininger, B. Schwarz, A. Wirthmüller, A. Harrer, O. Baumgartner, H. Detz, T. Zederbauer, D. MacFarland, A. M. Andrews, W. Schrenk, L. Hvozdar, H. Kosina, and G. Strasser. “Towards higher temperature operation of quantum cascade detectors”. ITQW, New York, USA. 2013.
- [O36] B. Schwarz, P. Reininger, O. Baumgartner, T. Zederbauer, H. Detz, A. M. Andrews, W. Schrenk, H. Kosina, and G. Strasser. “Towards Mid-Infrared On-Chip Sensing utilizing a bi-functional Quantum Cascade Laser/Detector”. Conference on Electronic Properties of Two-Dimensional Systems / Modulated Semiconductor Structures (EP2Ds-MSS), Wroclaw, Polen. 2013.
- [O35] B. Schwarz, P. Reininger, H. Detz, T. Zederbauer, A. M. Andrews, W. Schrenk, O. Baumgartner, H. Kosina, and G. Strasser. “Same-frequency detector and laser utilizing bi-functional quantum cascade active regions”. SPIE Photonics West 2013, San Francisco. 2013.
- [O34] B. Schwarz, P. Reininger, D. Ristanic, O. Baumgartner, H. Detz, T. Zederbauer, D. MacFarland, A. M. Andrews, W. Schrenk, H. Kosina, and G. Strasser. “On-Chip mid-infrared light generation and detection”. eingeladen; ITQW, New York, USA. 2013.
- [O33] B. Schwarz, P. Reininger, W. Schrenk, H. Detz, O. Baumgartner, T. Zederbauer, A. M. Andrews, H. Kosina, and G. Strasser. “Monolithically integrated quantum cascade laser and detector”. CLEO Europe 2013, München, Deutschland. 2013.

- [O32] C. Schwarzer, R. Szedlak, S. Ahn, T. Zederbauer, H. Detz, A. M. Andrews, W. Schrenk, and G. Strasser. “Linearly Polarized Emission Beams from Vertically Emitting Quantum Cascade Ring Lasers”. ITQW, New York, USA. 2013.
- [O31] G. Strasser, B. Schwarz, P. Reininger, O. Baumgartner, W. Schrenk, T. Zederbauer, H. Detz, A. M. Andrews, and H. Kosina. “Bi-functional Quantum Cascade Laser/Detectors for Integrated Photonics”. eingeladen; ÖPG-Jahrestagung, Linz. 2013.
- [O30] M. Brandstetter, M. Janits, C. Deutsch, M. Martl, A. Benz, H. Detz, T. Zederbauer, A. M. Andrews, W. Schrenk, and G. Strasser. “Coupled microdisk THz quantum cascade lasers”. *Technical Digest*. EOS Topical Meeting on Terahertz & Science Technology (TST 2012), Prag. 2012.
- [O29] M. Brandstetter, M. Janits, C. Deutsch, M. Martl, A. Benz, H. Detz, T. Zederbauer, A. M. Andrews, W. Schrenk, G. Strasser, and K. Unterrainer. “Coupling of THz quantum cascade lasers with microdisk cavities”. *Technical Digest*. MIRTHER-IRON-SensorCAT virtual conference 2012, Princeton. 2012.
- [O28] H. Detz, C. Deutsch, T. Zederbauer, A. M. Andrews, M. Schuster, P. Klang, A. Benz, W. Schrenk, K. Unterrainer, and G. Strasser. “Symmetric InGaAs/GaAsSb based THz quantum cascade lasers”. *GDR-I Workshop 2012*. eingeladen; GDRI-CNRS workshop: Semiconductor Sources and Detectors of THz Radiation, Tignes, Frankreich. 2012, pp. 14–15.
- [O27] H. Detz, C. Deutsch, T. Zederbauer, P. Klang, A. M. Andrews, M. Schuster, W. Schrenk, K. Unterrainer, and G. Strasser. “Symmetric InGaAs/GaAsSb Terahertz Quantum Cascade Lasers as a Tool for Interface Analysis”. *MBE2012*. The 17th International Conference on Molecular Beam Epitaxy (MBE 2012), Nara, Japan. 2012, pp. 1–2.
- [O26] H. Detz, T. Zederbauer, P. Klang, A. M. Andrews, M. Nobile, M. Schuster, C. Deutsch, M. Brandstetter, W. Schrenk, K. Unterrainer, and G. Strasser. “Improved InGaAs/GaAsSb MBE Growth of Quantum Cascade Lasers”. *Proceedings of 17th International Winterschool on New Developments in Solid State Physics*. 17th International Winterschool on New Developments in Solid State Physics, Mauterndorf. 2012.
- [O25] C. Deutsch, H. Detz, T. Zederbauer, A. M. Andrews, W. Schrenk, A. Benz, G. Strasser, and K. Unterrainer. “Terahertz Quantum Cascade Lasers with Sym-

- metric Active Regions”. *Technical Digest*. CLEO 2012, San Jose, California, USA. 2012.
- [O24] C. Deutsch, H. Detz, T. Zederbauer, A. M. Andrews, W. Schrenk, K. Unterrainer, T. Kubis, and G. Strasser. “Probing growth-induced imperfections with symmetric terahertz quantum cascade laser structures”. *International Quantum Cascade Lasers School & Workshop 2012*. eingeladen; International Quantum Cascade Lasers School & Workshop 2012 (IQCLSW 2012), Baden. 2012, p. 60.
- [O23] R. Gansch, S. Kalchmair, A. M. Andrews, H. Detz, T. Zederbauer, W. Schrenk, and G. Strasser. “Photonic Crystal Slabs for Resonant Cavity Enhancement of Quantum Well Infrared Photodetectors”. *PECS -X: 10th International Symposium on Photonic and Electromagnetic Crystal Structures*. International Symposium on Photonic and Electromagnetic Crystal Structures, Santa Fe, New Mexico, USA. 2012, pp. 82–83.
- [O22] R. Gansch, S. Kalchmair, P. Reininger, H. Detz, T. Zederbauer, A. M. Andrews, W. Schrenk, and G. Strasser. “Stacked Photonic Crystal Slabs as Resonant Cavities for Multicolor Quantum Well Infrared Photodetectors”. *QSIP12*. QSIP Quantum Structured Infrared Photodetectors, Cargèse, Frankreich. 2012, p. 48.
- [O21] S. Ahn, C. Schwarzer, S. Kalchmair, R. Gansch, D. Ristanic, T. Zederbauer, H. Detz, A. M. Andrews, W. Schrenk, and G. Strasser. “The Mode Reflectivity Reduction of Quantum Cascade Lasers by a Tilted Front Facet”. MIRTHER-IRON-SensorCAT virtual conference 2012, Princeton. 2012.
- [O20] A. M. Andrews, C. Deutsch, A. Benz, H. Detz, T. Zederbauer, W. Schrenk, K. Unterrainer, and G. Strasser. “Terahertz Quantum Cascade Lasers”. eingeladen; WOCSEMMAD, Napa, CA, USA. 2012.
- [O19] A. M. Andrews, M. Nobile, C. Deutsch, H. Detz, T. Zederbauer, W. Schrenk, K. Unterrainer, and G. Strasser. “InGaAs/GaAsSb Material System for Quantum Cascade Lasers”. eingeladen; MIOMD-XI Infrared Optoelectronics: Materials and Devices, Chicago, USA. 2012.
- [O18] A. M. Andrews, M. Nobile, C. Deutsch, H. Detz, T. Zederbauer, W. Schrenk, K. Unterrainer, and G. Strasser. “InGaAs/GaAsSb Quantum Cascade Lasers”. eingeladen; GMe Forum 2012, Wien. 2012.
- [O17] A. M. Andrews, M. Nobile, C. Deutsch, H. Detz, T. Zederbauer, W. Schrenk, K. Unterrainer, and G. Strasser. “InGaAs/GaAsSb Quantum Cascade Lasers”. eingeladen; Nanophotonics and Electronics Meeting, Paris, Frankreich. 2012.



- [O16] C. Deutsch, H. Detz, T. Zederbauer, A. M. Andrews, T. Kubis, W. Schrenk, G. Strasser, and K. Unterrainer. “Enhanced performance of terahertz quantum cascade lasers in reverse operating direction”. Int. Conf. on Superlattices, Nanostructures and Nanodevices (ICSNN), Dresden, Deutschland. 2012.
- [O15] C. Deutsch, H. Detz, T. Zederbauer, A. M. Andrews, W. Schrenk, A. Benz, G. Strasser, and K. Unterrainer. “Operating direction of terahertz quantum cascade lasers”. OSA Topical Meetings: Optical Terahertz Science and Technology, Prag. 2012.
- [O14] R. Gansch, S. Kalchmair, H. Detz, T. Zederbauer, A. M. Andrews, W. Schrenk, and G. Strasser. “Impedance matched resonant cavities for quantum well infrared photodetectors”. International Quantum Cascade Lasers School & Workshop 2012 (IQCLSW 2012), Baden. 2012.
- [O13] S. Kalchmair, R. Gansch, A. M. Andrews, H. Detz, T. Zederbauer, W. Schrenk, and G. Strasser. “Focusing of Light with a Plasmonic Lens onto Mid-Infrared Quantum Well Photodetector”. 10th International Symposium on Photonic and Electromagnetic Crystal Structures (PECS-X), Santa Fe, New Mexico, USA. 2012.
- [O12] S. Kalchmair, R. Gansch, E. Mujagic, S. Ahn, P. Reininger, G. Lasser, A. M. Andrews, H. Detz, T. Zederbauer, W. Schrenk, and G. Strasser. “Increased Detectivity and Operation Temperature in Photonic Crystal Slab Quantum Well Photodetectors”. CLEO 2012, San Jose, California, USA. 2012.
- [O11] M. Krall, M. Brandstetter, C. Deutsch, A. Benz, H. Detz, T. Zederbauer, A. M. Andrews, W. Schrenk, G. Strasser, and K. Unterrainer. “Micropillar array quantum cascade terahertz emitters”. MIRTHE-IROn-SensorCAT virtual conference 2012, Princeton. 2012.
- [O10] P. Reininger, S. Kalchmair, R. Gansch, A. M. Andrews, H. Detz, T. Zederbauer, W. Schrenk, and G. Strasser. “Enhancing the detectivity of photonic crystal photodetectors by quality factor tuning”. ÖPG-Jahrestagung, Graz. 2012.
- [O9] P. Reininger, S. Kalchmair, R. Gansch, E. Mujagic, S. Ahn, A. M. Andrews, H. Detz, T. Zederbauer, W. Schrenk, and G. Strasser. “Improving the detectivity of quantum well infrared photodetectors with photonic crystal slabs”. MIRTHE-IROn-SensorCAT virtual conference 2012, Princeton. 2012.

- [O8] G. Strasser, C. Deutsch, H. Detz, T. Zederbauer, A. M. Andrews, T. Kubis, W. Schrenk, and K. Unterrainer. “InGaAs/GaAsSb: a new material system for THz QCLs”. eingeladen; International Conference on Physics of Semiconductor (ICPS), Zürich, Schweiz. 2012.
- [O7] A. M. Andrews, M. Nobile, H. Detz, P. Klang, T. Zederbauer, W. Schrenk, and G. Strasser. “Growth of Mid-infrared InGaAs/GaAsSb QCLs emitting around 11  $\mu\text{m}$ ”. *The 11th International Conference on Intersubband Transitions in Quantum Wells (ITQW 2011)*. ITQW, Badesi, Italy. 2011.
- [O6] C. Schwarzer, E. Mujagic, T. Zederbauer, H. Detz, Y Yan, A. M. Andrews, W. Schrenk, J Chen, C. Gmachl, and G. Strasser. “Broadband single-mode and coherently emitting two-dimensional arrays”. *The 11th International Conference on Intersubband Transitions in Quantum Wells (ITQW 2011)*. ITQW, Badesi, Italy. 2011.
- [O5] C. Schwarzer, E. Mujagic, T. Zederbauer, H. Detz, Y Yao, A. M. Andrews, W. Schrenk, J. Chen, C. Gmachl, and G. Strasser. “Two Dimensional Integration of Ring Cavity Surface Emitting Quantum Cascade Lasers”. *AIP Conference Proceedings*. 15th International Conference on Narrow Gap Systems, Blacksburg, USA. 2011, pp. 49–51.
- [O4] H. Detz, C. Deutsch, M. Schuster, M. Nobile, P. Klang, T. Zederbauer, A. M. Andrews, W. Schrenk, K. Unterrainer, and G. Strasser. “Interface Analysis in Symmetric InGaAs/GaAsSb THz Quantum Cascade Lasers”. North American Conf. on Molecular Beam Epitaxy (NAMBE), San Diego, USA. 2011.
- [O3] S. Kalchmair, R. Gansch, P. Reininger, S. Schartner, A. M. Andrews, H. Detz, P. Klang, T. Zederbauer, W. Schrenk, and G. Strasser. “Resonant photonic detection”. eingeladen; Nano Photonics Meeting, Wien. 2011.
- [O2] C. Schwarzer, E. Mujagic, T. Zederbauer, H. Detz, W. Schrenk, Y Yao, C. Gmachl, and G. Strasser. “Ring cavity surface emitting quantum cascade lasers and their two-dimensional integration”. EP2DS19/MSS15, Tallahassee, usa. 2011.
- [O1] H. Detz, E. Mujagic, C. Schwarzer, T. Zederbauer, P. Klang, A. M. Andrews, W. Schrenk, C. Deutsch, K. Unterrainer, and G. Strasser. “Ring Cavity Induced Performance Enhancement in Mid-Infrared and Terahertz Quantum Cascade Lasers”. 60th Annual Meeting Austrian Physical Society, Salzburg. 2010.

---

## Poster Presentations

- [P59] H. Detz, M. Kriz, S. Lancaster, D. MacFarland, M. Schinnerl, T. Zederbauer, A. M. Andrews, W. Schrenk, and G. Strasser. “Lithography-Free Positioned GaAs Nanowire Growth”. *Digital digest*. 19<sup>th</sup> International Winterschool - New Developments in Solid State Physics, Mauterndorf. 2016.
- [P58] H. Detz, S. Lancaster, H. Groiss, D. MacFarland, A. M. Andrews, T. Zederbauer, W. Schrenk, and G. Strasser. “Formation of B-enriched clusters on GaAs nanowire sidewalls”. *German MBE Workshop*. German MBE Workshop, Garching, Deutschland. 2016.
- [P57] H. Detz, D. MacFarland, T. Zederbauer, S. Lancaster, A. M. Andrews, W. Schrenk, and G. Strasser. “Anomalous Incorporation of B into  $B_xGa_{1-x}As$  Layers”. *Final Program*. 19<sup>th</sup> International Conference on Molecular Beam Epitaxy, Montpellier, Frankreich. 2016, pp. 1–2.
- [P56] A. Harrer, B. Schwarz, R. Szedlak, S. Schuler, H. Detz, A. M. Andrews, T. Zederbauer, D. MacFarland, W. Schrenk, and G. Strasser. “High performance quantum cascade detector array for CO<sub>2</sub> detection”. *Technical Digest*. International Quantum Cascade Lasers School and Workshop (IQCLSW 2016), Cambridge. 2016.
- [P55] A. Harrer, R. Szedlak, B. Schwarz, H. Moser, T. Zederbauer, H. Detz, A. M. Andrews, W. Schrenk, B. Lendl, and G. Strasser. “A mid-infrared gas-sensing device based on bi-functional quantum cascade structures”. *Digital digest*. 19<sup>th</sup> International Winterschool - New Developments in Solid State Physics, Mauterndorf. 2016.
- [P54] M. Holzbauer, R. Szedlak, D. MacFarland, T. Zederbauer, H. Detz, A. M. Andrews, W. Schrenk, M. P. Semtsiv, W. T. Masselink, and G. Strasser. “Towards continuous wave operation of ring cavity quantum cascade lasers”. *Europhysics Conference Abstract Volume 40 B*. 7<sup>th</sup> EPS-QEOD Europhoton Conference (EUROPHOTON 2016), Wien. 2016, p. 33.
- [P53] M. Holzbauer, R. Szedlak, D. MacFarland, T. Zederbauer, H. Detz, A. M. Andrews, W. Schrenk, and G. Strasser. “Substrate-emitting ring quantum cascade laser array with distributed feedback metal gratings”. *Technical digest*. International Quantum Cascade Lasers School and Workshop (IQCLSW 2016), Cambridge. 2016.

- [P52] M. A. Kainz, M. Brandstetter, T. Zederbauer, M. Krall, S. Schönhuber, H. Detz, W. Schrenk, A. M. Andrews, T. Grange, G. Strasser, and K. Unterrainer. “InAs based Terahertz Quantum Cascade Lasers”. *Technical Digest*. International Quantum Cascade Lasers School and Workshop (IQCLSW 2016), Cambridge. 2016.
- [P51] M. A. Kainz, M. Brandstetter, T. Zederbauer, M. Krall, S. Schönhuber, H. Detz, W. Schrenk, A. M. Andrews, G. Strasser, and K. Unterrainer. “Terahertz Quantum Cascade Lasers based on InAs”. *Technical Digest*. 19<sup>th</sup> International Winterschool Mauterndorf 2016, Mauterndorf. 2016.
- [P50] M. Krall, M. A. Kainz, M. Brandstetter, C. Deutsch, D. MacFarland, T. Zederbauer, H. Detz, A. M. Andrews, W. Schrenk, G. Strasser, and K. Unterrainer. “Systematic comparison of alternative barrier materials for InGaAs-based terahertz quantum cascade lasers”. *Proceedings of the ICPS 2016*. 33<sup>rd</sup> International Conference on the Physics of Semiconductors (ICPS2016), Beijing, China. 2016.
- [P49] S. Lancaster, A. M. Andrews, T. Zederbauer, D. MacFarland, H. Detz, and G. Strasser. “Schottky barrier formation in GaAs nanowires by heterogeneous contact deposition”. *Conference Documentation*. International Conference Functional Integrated nano Systems, Graz. 2016.
- [P48] B. Schwarz, D. Ristanic, P. Reininger, T. Zederbauer, D. MacFarland, H. Detz, A. M. Andrews, W. Schrenk, and G. Strasser. “A monolithically integrated mid-infrared lab-on-a-chip”. *Digital digest*. 19<sup>th</sup> International Winterschool Mauterndorf 2016, Mauterndorf. 2016.
- [P47] R. Szedlak, A. Harrer, M. Holzbauer, B. Schwarz, J. P. Wacławek, D. MacFarland, T. Zederbauer, H. Detz, A. M. Andrews, W. Schrenk, B. Lendl, and G. Strasser. “Laser Surface Emission and Detection from the same Quantum Cascade Element”. *Proceedings of the ICPS 2016*. 33<sup>rd</sup> International Conference on the Physics of Semiconductors (ICPS2016), Beijing, China. 2016, p. 658.
- [P46] R. Szedlak, T. Hisch, M. Holzbauer, D. MacFarland, T. Zederbauer, H. Detz, A. M. Andrews, W. Schrenk, S. Rotter, and G. Strasser. “Creation of Orbital Angular Momentum using an On-chip Dielectric Metamaterial for Beam Shaping”. *Proceedings of the ICPS 2016*. 33<sup>rd</sup> International Conference on the Physics of Semiconductors (ICPS2016), Beijing, China. 2016, p. 659.

- 
- [P45] A. M. Andrews, T. Zederbauer, D. MacFarland, H. Detz, P. Reininger, B. Schwarz, W. Schrenk, and G. Strasser. “Growth of  $\text{Al}_x\text{In}_{1-x}\text{As}_{1-y}\text{Sb}_y$  for InAs-based Quantum Cascade Detectors”. 19<sup>th</sup> International Winterschool Mautern-dorf 2016, Mautern-dorf. 2016.
- [P44] S. Lancaster, A. M. Andrews, T. Zederbauer, D. MacFarland, H. Detz, and G. Strasser. “Impact of Annealing Temperature on Au/Zn/Au Contacts to GaAs Nanowires”. 19<sup>th</sup> International Winterschool Mautern-dorf 2016, Mautern-dorf. 2016.
- [P43] L. Prochaska, D. MacFarland, A. M. Andrews, M. Bonta, H. Detz, W. Schrenk, T. Zederbauer, A. Limbeck, G. Strasser, J. Bernardi, and S. Paschen. “First results on  $\text{YbRh}_2\text{Si}_2$  film growth by molecular beam epitaxy”. Workshop on Frontiers of Quantum Materials, Rice University, Houston, USA, Houston. 2016.
- [P42] L. Prochaska, D. MacFarland, A. M. Andrews, H. Detz, W. Schrenk, G. Strasser, T. Zederbauer, and S. Paschen. “Heavy fermion film growth by molecular beam epitaxy”. DK Solids4Fun Summer School 2016, Ybbs. 2016.
- [P41] B. Schwarz, D. Ristanic, P. Reininger, H. Detz, T. Zederbauer, D. MacFarland, A. M. Andrews, W. Schrenk, and G. Strasser. “Mid-infrared spectroscopy on a single chip”. MESS16 - Microelectronic Systems Symposium, Wien. 2016.
- [P40] M. A. Kainz, M. Brandstetter, T. Zederbauer, M. Krall, S. Schönhuber, A. M. Andrews, W. Schrenk, G. Strasser, and K. Unterrainer. “Towards InAs based Terahertz Quantum Cascade Lasers”. *Gemeinsame Jahrestagung in Wien - ÖPG Tagungsband*. Gemeinsame Jahrestagung 2015 der ÖPG, SPS, ÖGA und SSAA in Wien, Wien. 2015.
- [P39] D. MacFarland, M. Krall, H. Detz, O. Bethge, T. Zederbauer, A. M. Andrews, W. Schrenk, M. Brandstetter, K. Unterrainer, and G. Strasser. “Growth and Characterization of AlGaInAs for use as the Barrier Material in Terahertz Quantum Cascade Lasers”. *Technical Digest*. ITQW, Wien. 2015, pp. 252–253.
- [P38] A. Harrer, R. Szedlak, B. Schwarz, H. Moser, T. Zederbauer, H. Detz, A. M. Andrews, W. Schrenk, B. Lendl, and G. Strasser. “Towards a monolithic integrated surface emitting and detecting mid-infrared gas sensor”. ITQW, Wien. 2015.
- [P37] M. Holzbauer, R. Szedlak, D. MacFarland, T. Zederbauer, H. Detz, A. M. Andrews, W. Schrenk, and G. Strasser. “High Performance Ring Quantum Cascade Laser for Sensing Applications”. ICAVS8, Wien. 2015.

- [P36] M. Holzbauer, R. Szedlak, D. MacFarland, T. Zederbauer, H. Detz, A. M. Andrews, W. Schrenk, and G. Strasser. “Thermal Optimization of Ring Quantum Cascade Lasers”. ITQW, Wien. 2015.
- [P35] L. Prochaska, A. M. Andrews, H. Detz, D. MacFarland, W. Schrenk, G. Strasser, T. Zederbauer, and S. Paschen. “Developing heavy fermion film growth by molecular beam epitaxy”. C-MAC Euroschool 2015 Material synthesis and characterization applied to complex metallic alloys, Bratislava. 2015.
- [P34] L. Prochaska, S. Dzsaber, G. Eguchi, W. Artner, A. M. Andrews, H. Detz, D. MacFarland, W. Schrenk, G. Strasser, T. Zederbauer, and S. Paschen. “A new molecular beam epitaxy system for the growth of heavy fermion thin films”. NGSCES 2015: The New Generation in Strongly Correlated Electron Systems, Trogir; Croatia. 2015.
- [P33] R. Szedlak, M. Holzbauer, D. MacFarland, T. Zederbauer, H. Detz, A. M. Andrews, W. Schrenk, and G. Strasser. “How whispering gallery modes can influence the far field of ring lasers”. ITQW, Wien. 2015.
- [P32] A. Harrer, B. Schwarz, R. Gansch, P. Reininger, H. Detz, T. Zederbauer, A. M. Andrews, W. Schrenk, and G. Strasser. “Mid-infrared Plasmonic Lens Inter-subband Photodetector”. *New Developments in Solid State Physics - Mauterndorf 2014*. 18<sup>th</sup> International Winterschool on New Developments in Solid State Physics, Mauterndorf. 2014, pp. 108–109.
- [P31] P. Reininger, B. Schwarz, A. Harrer, T. Zederbauer, H. Detz, A. M. Andrews, R. Gansch, W. Schrenk, and G. Strasser. “2.5 D photonic crystal quantum cascade detector”. *Laser Science to Photonic Applications*. CLEO 2014, San Jose. 2014.
- [P30] P. Reininger, B. Schwarz, A. Harrer, T. Zederbauer, H. Detz, A. M. Andrews, R. Gansch, W. Schrenk, and G. Strasser. “Photonic crystal quantum cascade detector”. *New Developments in Solid State Physics*. 18<sup>th</sup> International Winterschool on New Developments in Solid State Physics, Mauterndorf. 2014, pp. 92–93.
- [P29] B. Schwarz, P. Reininger, D. Ristanic, H. Detz, T. Zederbauer, D. MacFarland, A. M. Andrews, W. Schrenk, and G. Strasser. “Towards mid-infrared on-chip sensing”. *New Developments in Solid State Physics - Mauterndorf 2014*. 18<sup>th</sup> International Winterschool on New Developments in Solid State Physics, Mauterndorf. 2014, pp. 106–107.

- [P28] A. M. Andrews, M. Brandstetter, M. Krall, C. Deutsch, T. Zederbauer, D. MacFarland, H. Detz, W. Schrenk, K. Unterrainer, and G. Strasser. “Role of Facet Type on Terahertz Quantum Cascade Lasers with Metal-Metal Waveguides”. 18<sup>th</sup> International Winterschool on New Developments in Solid State Physics, Mauterndorf. 2014.
- [P27] C. Deutsch, M. Brandstetter, M. Krall, H. Detz, T. Zederbauer, A. M. Andrews, W. Schrenk, and G. Strasser. “Terahertz Quantum Cascade Lasers: From Growth Asymmetries Towards Watt-level Performance”. 20 Years of Quantum Cascade Laser Workshop, Zürich, Schweiz. 2014.
- [P26] A. Harrer, B. Schwarz, R. Gansch, P. Reininger, H. Detz, T. Zederbauer, A. M. Andrews, W. Schrenk, and G. Strasser. “Mid-infrared detectors with on-chip light collection”. International Quantum Cascade Lasers School & Workshop (IQCLSW 2014), Bari. 2014.
- [P25] L. Prochaska, A. M. Andrews, H. Detz, D. MacFarland, W. Schrenk, G. Strasser, T. Zederbauer, and S. Paschen. “Molecular beam epitaxy of heavy fermion compounds”. NGSCES 2014 - The New Generation in Strongly Correlated Electron Systems 2014, Nizza, France. 2014.
- [P24] L. Prochaska, A. M. Andrews, H. Detz, D. MacFarland, W. Schrenk, G. Strasser, T. Zederbauer, and S. Paschen. “The rocky road to heavy fermion films grown by molecular beam epitaxy”. DK Solids4Fun Summer School, Hernstein. 2014.
- [P23] L. Prochaska, A. M. Andrews, H. Detz, D. MacFarland, W. Schrenk, G. Strasser, T. Zederbauer, and S. Paschen. “Towards heavy fermion films grown by MBE”. QCM14 - Quantum Critical Matter - From Atoms To Bulk, Obergurgl, Austria. 2014.
- [P22] C. Schwarzer, R. Szedlak, S. Ahn, D. MacFarland, T. Zederbauer, H. Detz, A. M. Andrews, W. Schrenk, and G. Strasser. “DFB Grating Phase-Shifts for Quantum Cascade Ring Lasers”. 18<sup>th</sup> International Winterschool on New Developments in Solid State Physics, Mauterndorf. 2014.
- [P21] M. Krall, M. Brandstetter, C. Deutsch, A. Benz, H. Detz, T. Zederbauer, A. M. Andrews, W. Schrenk, G. Strasser, and K. Unterrainer. “Micropillar Arrays of Terahertz Quantum Cascade Emitters Based on InGaAs/GaAsSb”. *Proceedings of the GMe Forum 2013*. GMe Forum 2013, Vienna. 2013.

- [P20] M. Krall, M. Brandstetter, C. Deutsch, T. Grange, H. Detz, T. Zederbauer, D. MacFarland, A. M. Andrews, W. Schrenk, G. Strasser, and K. Unterrainer. “Prospects and technological challenges of terahertz quantum cascade lasers based on semiconductor nanowires”. *Technical Digest*. International THz Conference, Villach, Österreich. 2013.
- [P19] A. Harrer, R. Gansch, P. Reininger, B. Schwarz, H. Detz, A. M. Andrews, T. Zederbauer, D. MacFarland, W. Schrenk, and G. Strasser. “Tuning of resonances in photonic crystal photodetectors”. Joint Annual Meeting of ÖPG, SPG, ÖGAA und SGAA 2013, Linz. 2013.
- [P18] M. Brandstetter, M. Janits, C. Deutsch, A. Benz, H. Detz, T. Zederbauer, A. M. Andrews, W. Schrenk, G. Strasser, and K. Unterrainer. “Coupling of THz quantum cascade lasers”. *Proceedings of 17<sup>th</sup> International Winterschool on New Developments in Solid State Physics*. 17<sup>th</sup> International Winterschool on New Developments in Solid State Physics, Mauterndorf, Austria. 2012.
- [P17] C. Deutsch, H. Detz, A. M. Andrews, T. Zederbauer, A. Benz, W. Schrenk, G. Strasser, and K. Unterrainer. “InGaAs/GaAsSb: Highly Attractive for Terahertz Quantum Cascade Lasers”. *Proceedings of 17<sup>th</sup> International Winterschool on New Developments in Solid State Physics*. 17<sup>th</sup> International Winterschool on New Developments in Solid State Physics, Mauterndorf. 2012.
- [P16] M. Krall, M. Brandstetter, C. Deutsch, A. Benz, H. Detz, T. Zederbauer, A. M. Andrews, W. Schrenk, G. Strasser, and K. Unterrainer. “Micropillar arrays of terahertz quantum cascade emitters based on InGaAs/GaAsSb”. *International Quantum Cascade Lasers School & Workshop 2012*. International Quantum Cascade Lasers School & Workshop 2012 (IQCLSW 2012), Baden. 2012, p. 159.
- [P15] M. Krall, M. Brandstetter, C. Deutsch, A. Benz, K. Unterrainer, H. Detz, T. Zederbauer, A. M. Andrews, W. Schrenk, and G. Strasser. “THz emission from InGaAs/GaAsSb micropillar arrays”. *Technical Digest*. EOS Topical Meeting on Terahertz & Science Technology (TST 2012), Prag. 2012.
- [P14] M. Krall, M. Brandstetter, C. Deutsch, A. Benz, K. Unterrainer, H. Detz, T. Zederbauer, A. M. Andrews, W. Schrenk, and G. Strasser. “Top-down fabrication and characterization of InGaAs/GaAsSb semiconductor nanowires”. *Proceedings of 17<sup>th</sup> International Winterschool on New Developments in Solid State Physics*. 17<sup>th</sup> International Winterschool on New Developments in Solid State Physics, Mauterndorf. 2012.



- [P13] S. Ahn, C. Schwarzer, S. Kalchmair, R. Gansch, D. Ristanic, T. Zederbauer, H. Detz, A. M. Andrews, W. Schrenk, and G. Strasser. “The Influence of a Tilted Facet on Quantum Cascade Lasers”. International Quantum Cascade Lasers School & Workshop 2012 (IQCLSW 2012), Baden. 2012.
- [P12] M. Brandstetter, M. Janits, C. Deutsch, M. Martl, A. Benz, H. Detz, T. Zederbauer, A. M. Andrews, W. Schrenk, G. Strasser, and K. Unterrainer. “THz quantum cascade lasers with coupled microdisk cavities”. GMe Forum 2012, Wien. 2012.
- [P11] H. Detz, T. Zederbauer, P. Klang, A. M. Andrews, M. Nobile, M. Schuster, C. Deutsch, M. Brandstetter, W. Schrenk, K. Unterrainer, and G. Strasser. “Improved InGaAs/GaAsSb MBE Growth of Quantum Cascade Lasers”. GMe Forum 2012, Wien. 2012.
- [P10] R. Gansch, S. Kalchmair, H. Detz, T. Zederbauer, A. M. Andrews, W. Schrenk, and G. Strasser. “Resonant cavity enhanced quantum well infrared photodetectors showing improved temperature performance”. International Conference on Physics of Semiconductor (ICPS), Zürich, Schweiz. 2012.
- [P9] S. Kalchmair, R. Gansch, P. Reininger, A. M. Andrews, H. Detz, T. Zederbauer, W. Schrenk, and G. Strasser. “High Detectivity and Enhanced Operation Temperature of Photonic Crystal Slab QWIPs”. 17<sup>th</sup> International Winterschool on New Developments in Solid State Physics, Mauterndorf. 2012.
- [P8] S. Kalchmair, R. Gansch, P. Reininger, A. M. Andrews, H. Detz, T. Zederbauer, W. Schrenk, and G. Strasser. “Photonic Crystal Slabs for Resonant Photodetection in Quantum Wells”. GMe Forum 2012, Wien. 2012.
- [P7] M. Krall, M. Brandstetter, C. Deutsch, A. Benz, K. Unterrainer, H. Detz, T. Zederbauer, A. M. Andrews, W. Schrenk, and G. Strasser. “In<sub>0.53</sub>Ga<sub>0.47</sub>As/GaAs<sub>0.51</sub>Sb<sub>0.49</sub> Semiconductor Nanowires: Fabrication and Electrical Characterization”. GMe Forum 2012, Wien. 2012.
- [P6] P. Reininger, R. Gansch, S. Kalchmair, H. Detz, T. Zederbauer, A. M. Andrews, W. Schrenk, and G. Strasser. “Detectivity Improvement of Quantum Well Infrared Photodetectors using a Photonic Crystal Slab as Resonant Cavity”. International Conference on Superlattices, Nanostructures, and Nanodevices (IC-SNN2012), Dresden. 2012.

- [P5] M Sassermann, L Einkemmer, P Mai, Z Vörös, G Weihs, T. Zederbauer, H. Detz, A. M. Andrews, G. Strasser, C Schneider, A Löffler, S Höfling, A Forchel, and S Protolan. “Toward polarisation entangled photon pairs from microcavity exciton polaritons”. ÖPG-Jahrestagung, Graz. 2012.
- [P4] H. Detz, J. Silvano de Sousa, M. Schwantzer, C. Deutsch, M. Nobile, T. Zederbauer, P. Klang, A. M. Andrews, W. Schrenk, J. Smoliner, K. Unterrainer, and G. Strasser. “Electronic characterization of InGaAs/GaAsSb heterostructures by magneto transport in resonant tunneling diodes”. *The 11<sup>th</sup> International Conference on Intersubband Transitions in Quantum Wells (ITQW 2011)*. ITQW, Badesi, Italy. 2011.
- [P3] C. Schwarzer, E. Mujagic, T. Zederbauer, H. Detz, Y Yao, A. M. Andrews, W. Schrenk, J Chen, C. Gmachl, and G. Strasser. “Two Dimensional Integration of Ring Cavity Surface Emitting Quantum Cascade Lasers”. *AIP Conference Proceedings*. International Conference on Physics of Semiconductor (ICPS), Soul, Korea. 2011, pp. 49–51.
- [P2] T. Zederbauer, C. Deutsch, M. Nobile, H. Detz, A. M. Andrews, P. Klang, W. Schrenk, and G. Strasser. “Growth of InGaAs/GaAsSb Heterostructures for MIR and THz Quantum Cascade Lasers”. *Program and Abstracts*. 3rd International Workshop on Epitaxial Growth and Fundamental Properties of Semiconductor Nanostructures, Traunkirchen. 2011, p. 145.
- [P1] T. Zederbauer, E. Mujagic, C. Schwarzer, and G. Strasser. “Analytical and Numerical Study on Surface Emitting Ring Lasers”. *60<sup>th</sup> Annual Meeting Austrian Physical Society*. 60<sup>th</sup> Annual Meeting Austrian Physical Society, Salzburg. 2010, pp. 194–195.